SPARK PLASMA SINTERING OF TUNGSTEN AND TUNGSTEN-CERIA: MICROSTRUCTURES AND KINETICS

by

Jeffrey Bryce Perkins

A thesis

submitted in partial fulfillment

of the requirements for the degree of

Master of Science in Materials Science and Engineering

Boise State University

December 2011

BOISE STATE UNIVERSITY GRADUATE COLLEGE

DEFENSE COMMITTEE AND FINAL READING APPROVALS

of the thesis submitted by

Jeffrey Bryce Perkins

Thesis Title: Spark Plasma Sintering of Tungsten and Tungsten-Ceria: Microstructures and Kinetics

Date of Final Oral Examination: 20 September 2010

The following individuals read and discussed the thesis submitted by student Jeffrey Bryce Perkins, and they evaluated his presentation and response to questions during the final oral examination. They found that the student passed the final oral examination.

Darryl P. Butt, Ph.D.	Chair, Supervisory Committee
Megan E. Frary, Ph.D.	Co-Chair, Supervisory Committee
Henry A. Charlier, Ph.D.	Member, Supervisory Committee

The final reading approval of the thesis was granted by Darryl P. Butt, Ph.D., Chair of the Supervisory Committee. The thesis was approved for the Graduate College by John R. Pelton, Ph.D., Dean of the Graduate College.

ACKNOWLEDGEMENTS

I would like to thank my advisors, Dr. Darryl Butt and Dr. Megan Frary, for allowing me the opportunity to research spark plasma sintering and for supporting me financially. I will always be grateful to Dr. Butt and Dr. Frary, and I will always appreciate both of them pushing me to finish. Thank you also to Dr. Henry Charlier for being on my thesis committee. Thank you very much to the Center for Advanced Energy Studies and Battelle Energy Alliance for supporting my research.

Dr. Will Windes and Mark Carroll from Idaho National Laboratory helped me along the way. Dr. Ivar Reimanis also helped by allowing me to use his hot press at Colorado School of Mines. Matt Luke, Todd Gansauge, James Carrillo, Kyle Knori, and Adriel Apter all helped in the production and analysis of my samples. Thank you very much to all of you.

Thank you to Aaron Thurber of the Boise State University Physics department, who helped to acquire and analyze the XPS data. The X-ray photoelectron spectroscopy experiments were made financially possible my Dr. Alex Punnoose of the Boise State University Physics department and NSF-MRI award 0722699.

Finally, thank you to my parents, Tom and Cathy Perkins, and my sister, Jamie Perkins, for their support. My mom has poured her time into this thesis, reading every page, asking questions, and helping with grammatical errors. I have her to thank the most for getting me to finish.

ABSTRACT

Tungsten casting is impractical, and tungsten compacts are most often produced by press-and-sinter or by hot pressing. The temperatures typically required to sinter tungsten above 90% dense are above 1800 ºC, and sintering times are typically hours. Alternatively, spark plasma sintering (SPS) can be used to consolidate materials to high densities at lower temperatures and shorter times than traditional sintering techniques. In this study, pure tungsten and tungsten with 1, 4, 10, 15, and 20 weight percent ceria were spark plasma sintered at varying pressures, temperatures, and times to investigate the microstructures and the kinetics of sintering.

Densification of tungsten and tungsten with 10 weight percent ceria begins between 800 and 900 ºC and densities greater than 90% can be achieved at temperatures as low as 1500 ºC. Grain growth is limited in the tungsten with 1, 10, and 20 weight percent ceria samples relative to the pure tungsten. The limited grain growth may be due to boundary pinning effects in the tungsten with 1 weight percent ceria, and it may be due to an increased diffusion distance in the tungsten with 10 and 20 weight percent ceria samples. The hardness of the tungsten and tungsten with 1 weight percent ceria is dependent on the density of the samples; however, the hardness of the tungsten with 10 and 20 weight percent ceria may be dependent on grain size and/or flaws in the microstructure. The ceria phase in these samples contained microscopic cracks, and these fractures may be due to a mismatch in thermal expansion between the tungsten and ceria

phases or they may be due to thermal shock from rapid heating or rapid cooling during SPS.

Ceria loss was observed in tungsten samples containing 10, 15, and 20 weight percent ceria that were spark plasma sintered above 1600 ºC. Using X-ray photoelectron spectroscopy, it was found that both the Ce^{3+} and Ce^{4+} ions were present in the samples, indicating that the ceria phase was reduced from CeO_2 to Ce_2O_3. This reaction likely releases oxygen gas, forming pores in the tungsten-ceria microstructure.

The densification kinetics of SPS tungsten has been determined using traditional hot pressing models. The models for plastic flow, lattice diffusion, and power-law creep were inadequate to describe the densification kinetics. Between 1100 and 1500 ºC, the rate-limiting mechanism for densification appears to be boundary diffusion. The apparent activation energy for boundary diffusion was found to be 360±20 kJ/mol, and the resulting diffusion constant was found to be 4.3±0.1 m^2/s. The densification kinetics data from this study are limited, and future experiments on spark plasma sintering of tungsten are necessary to confirm the results in this thesis. An attempt was also made to determine the grain growth kinetics of SPS tungsten. Grain size data from tungsten spark plasma sintered at 1200, 1500, and 1800 ºC were used to determine the apparent activation energy for grain growth. Realistic values for the grain growth exponents could not be determined, and future work is necessary.

TABLE OF CONTENTS

LIST OF TABLES

LIST OF FIGURES

LIST OF ABBREVIATIONS

BSE	—	Backscatter electron
EBSD	—	Electron backscatter diffraction
GE	—	General Electric
HIP	—	Hot isostatic pressing
HP	—	Hot pressing
RTG	—	Radioisotope thermal generator
SEM	—	Scanning electron microscope
SNAP	—	Space nuclear auxilary power
SPS	—	Spark plasma sintering
XPS	—	X-ray photoelectron spectroscopy

LIST OF SYMBOLS

a, b, c, d	—	Fitting parameters	μ_o	—	Shear modulus at 300K
a_o^3	—	Atomic volume	MW	—	Molecular weight
A^*	—	Dorn parameter for shear stress	n	—	Grain growth exponent, stress sensitivity exponent
B	—	Collection of material and geometric parameters	ϕ	—	Stress intensification parameter
b	—	Burgers vector	P_A	—	Applied stress
c	—	Constant equal to 1 for intermediate stage sintering and 2 for final stage sintering	P_E	—	Effective applied stress
δ	—	Boundary width	P_{pore}	—	Internal pore pressure
D_b	—	Boundary diffusion coefficient	P_v	—	Vapor pressure
D_{ob}	—	Boundary diffusion constant	Q	—	Apparent activation energy
D_s	—	Surface diffusion coefficient	Q_b	—	Activation energy for boundary diffusion
D_v	—	Lattice/volume diffusion coefficient	Q_v	—	Activation energy for volume/lattice diffusion
D_{ov}	—	Lattice/volume diffusion constant	r	—	Average pore size radius
d_{pore}	—	Average pore diameter	r_1, r_2	—	Radii of curvature
ε	—	Emissivity	ρ	—	Density
γ	—	Surface energy	ρ_i	—	Fractional green density
G	—	Average grain size	ρ_p	—	Fractional sintered porosity
G_o	—	Initial grain size	σ	—	Stress
h	—	Sample height	$\sigma_y(T)$	—	Temperature-dependent yield stress
K	—	Thermally-activated grain growth parameter	T_m	—	Melting temperature of material
K_o	—	Rate constant for grain growth	(T_m/μ_o) $(d\mu/dT)$	—	Temperature dependence of the shear modulus
m, n	—	Exponents indicating mechanism of sintering	x	—	Neck diameter
$\mu(T)$	—	Temperature-dependent shear modulus	X	—	Geometric term

CHAPTER 1: INTRODUCTION

1.1. Research Motivation and Objectives

Spark plasma sintering (SPS) has been shown to produce materials with high densities and limited grain growth within minutes, whereas pressureless sintering and hot pressing require hours to produce materials with similar densities. A majority of SPS studies have been based on trial-and-error approaches to achieve the desired properties of a materials system, and are not based on an understanding of the underlying mechanisms of SPS.[1] To optimize future SPS materials, it is necessary to understand the fundamental mechanisms of spark plasma sintering and to develop models to predict the properties of a sintered compact.

This study was designed to take a systematic approach to some of the process variables and determine which of these variables has the greatest impact on the spark plasma sintering of pure tungsten powders and tungsten-ceria composite powders. The process variables investigated were sintering time, sintering temperature, and applied pressure. The final densities, grain sizes, and hardness values of the SPS compacts were measured. The SPS tungsten data were applied to traditional models for plastic flow, lattice diffusion in hot pressing, and boundary diffusion in hot pressing to determine the rate-limiting mechanism of densification. The activation energies and diffusivities found using these models were compared to the activation energies and diffusivities from previously published research on tungsten sintering. The SPS tungsten data was also

applied to models for isothermal and nonisothermal grain growth to determine the rate-limiting mechanism. The activation energies and diffusivities for grain growth found using these methods were compared to the values in the literature. Based on the results in this thesis, areas of future research were recommended.

In addition to providing a better understanding of the spark plasma sintering process, this study was also designed to demonstrate spark plasma sintering as a viable method for consolidating tungsten-ceria composite powders. The tungsten-ceria system is an important starting point for future production of tungsten-plutonia cermets for nuclear applications. Nuclear fuel bearing tungsten cermets and other refractory metal cermets have been studied previously, both for use in radioisotope thermoelectric generators (RTGs)[2-6] and as fuel elements in nuclear reactors for nuclear thermal rockets.[7-10]

The first plutonia cermets were produced for the Systems Nuclear Auxiliary Power (SNAP) program headed by the US Atomic Energy Commission. Plutonia molybdenum cermets were developed during this program, and these cermets were used to fuel the SNAP-19 RTG and the Transit RTG.[11-13] The SNAP-19 RTG was used as the power source for the Pioneer 10 and 11 spacecrafts,[13] which operated until 2003 and 1995, respectively.[12] The Transit TRIAD satellite used the Transit RTG, and operated for more than a decade after launch.[12] The legacy of these long-lived spacecrafts has demonstrated the realistic possibility of using plutonia-fueled cermets for RTGs in future space exploration.

Uranium oxide-bearing tungsten cermets were first produced during the GE 710 program.[10] The goal of the program was to produce tungsten fuel elements containing

UO_2 for use in a nuclear rocket engine core.[10] Tungsten cermets containing up to 60 vol% UO_2 were produced by cold pressing then sintered above 2200 ºC for a minimum of one hour in hydrogen.[10] Many technical challenges arose from this process, including reduction and loss of the fuel during sintering,[8,10] low density parts,[10] and warping of the final parts.[8] Spark plasma sintering may be advantageous to pressureless sintering techniques because the sintering time is reduced from hours to minutes, SPS parts can reach high densities at lower temperatures than traditional sintering techniques,[14-16] and the die body can be used to produce near net shape parts. Processing of these same nuclear systems by SPS may mitigate or eliminate some of the problems experienced during earlier tungsten cermet studies, and it may become more feasible for tungsten cermets to be used in future nuclear applications.

1.2. Materials Processed

1.2.1. Selection of Tungsten

Tungsten was first selected as a potential matrix material for high temperature nuclear applications during the nuclear rocket program in the United States.[7] Los Alamos Science Laboratory (now Los Alamos National Laboratory) was in charge of primary development of nuclear thermal rocket technology, and chose to pursue graphite-based fuel elements instead of tungsten-based fuel elements.[17] Concurrent to the graphite-based program, the GE 710 program[10] and the Argonne National Laboratory Cermet Nuclear Rocket program[8] focused on the development of tungsten-based fuel elements. Studies on refractory metal fast reactors showed an apparent advantage over graphite-based reactors, including a reactor lifetime of greater than 10 h, high specific impulses (800-900

s) on multiple restarts, and a lighter and more compact reactor design than graphite-based reactors with similar thermal power and specific impulse.[8]

The nuclear rocket designs required the hottest possible reactor to achieve the highest specific impulse, and tungsten was selected due to this requirement. Tungsten has the highest melting point of any metal (3422±15 ºC) and lowest vapor pressure of any metal,[18] making it ideal for a high-temperature space reactor. Based on the legacy of tungsten being used to produce nuclear-fueled cermets, tungsten was used as the metal matrix material in this study.

1.2.2. Selection of Cerium Dioxide

Although the ultimate goal of this research is to use a nuclear fuel encapsulated in tungsten, cerium dioxide (CeO_2) was used as a surrogate material for plutonium dioxide (PuO_2). Multiple studies[19-22] have compared experiments using ceria and experiments using plutonia, and the results of these studies have shown ceria to be good surrogate material for plutonia. A surrogate is necessary for these initial studies to prevent radiation exposure to researchers and equipment.

Ceria was selected as the surrogate for plutonia because the thermodynamic properties are similar in both systems. For example, the Gibbs free energies of CeO_2 and Ce_2O_3 are comparable to PuO_2 and Pu_2O_3, respectively (Figure 1.1). Both ceria and plutonia form the fluorite crystal structure, and these fluorites are typically hypostoichiometric with respect to oxygen.[22] The fluorite structures of both oxides are stable in nearly the same temperature regime with respect to oxygen nonstoichiometry, as can be seen by comparing the phase diagrams of ceria[23] and plutonia[24] (Figure 1.2).

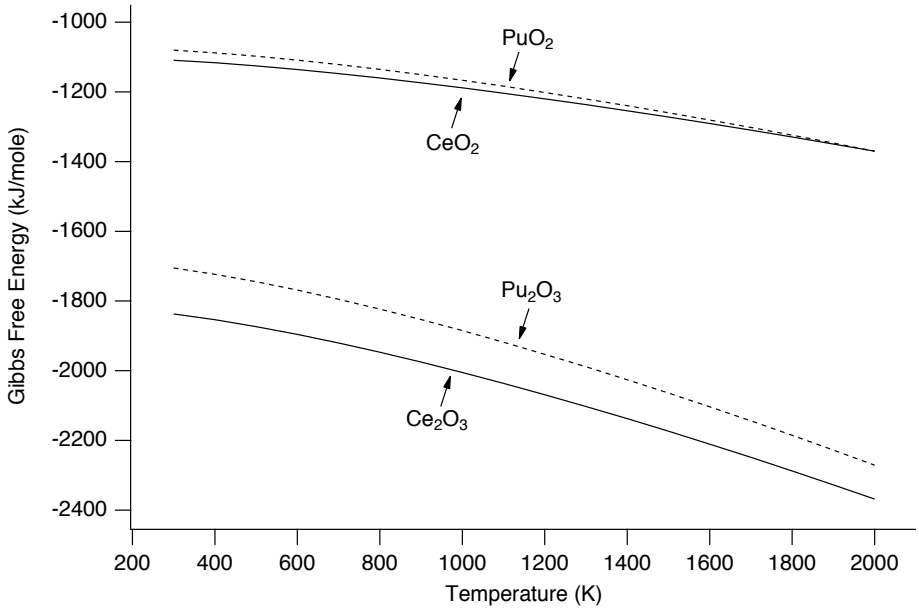

Figure 1.1. Comparison of the Gibbs free energy for CeO_2, PuO_2, Ce_2O_3 and Pu_2O_3. The Gibbs free energy is similar in the two systems, showing the thermodynamic applicability of ceria as a surrogate for plutonia. (Data from Zinkevich *et al.*[23] and Guéneau *et al.*[24])

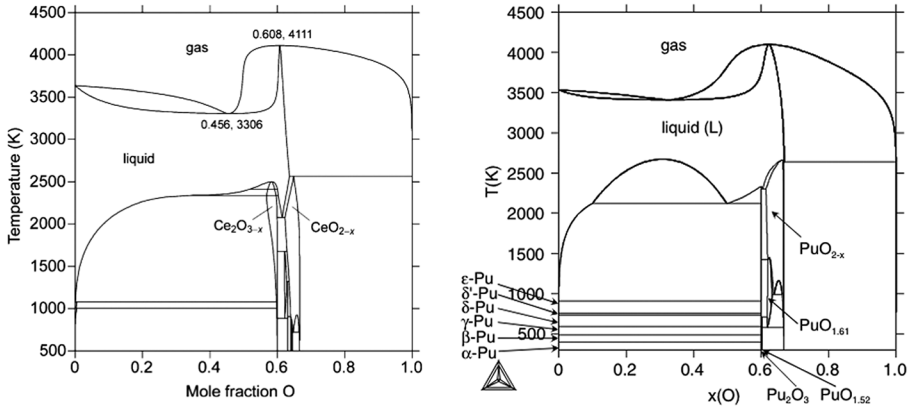

Figure 1.2. Comparison of Ce-O phase diagram[23] (left) and Pu-O phase diagram[24] (right) showing similar structure dependency on the mole fraction of oxygen. The fluorite phase exists in the CeO_{2-x} and PuO_{2-x} regions. (Diagrams are reproduced by permission from the publishers.)

CHAPTER 2: LITERATURE REVIEW

Sintering is a thermally activated process whereby a porous compact is densified by mass transport occurring primarily at the atomic level. Diffusion mechanisms are activated as thermal energy is added to the system, and atoms will diffuse to particle contacts, bonding the particles.[25] There is an inherent stress associated with the surface curvature of the particles, and this stress provides the thermodynamic driving force for particles to coarsen, reducing the surface stress as the radii of the particles increase.[26] The surface stress is proportional to the surface free energy and inversely proportional to the radius of curvature of the particles, as expressed by the Laplace equation:

$$\sigma = \gamma\left(\frac{1}{r_1} + \frac{1}{r_2}\right) \qquad 2.1$$

where σ is the surface stress, γ is the surface free energy, and r_1 and r_2 are the radii of curvature.[25] The inverse relationship between the surface stress and the particle radii implies that smaller particles will have a higher surface stress than larger particles, increasing the thermodynamic driving force for sintering.[25-27] These principles are the fundamental basis for sintering, and will be described in more detail in this chapter.

This chapter will introduce the mechanisms responsible for solid state sintering, the stages of sintering, and the effects of pressure and electrical current on the sintering process. In the last section of this chapter, a review of these sintering processes as applied to tungsten is presented.

2.1. Mass Transport Mechanisms

Fundamentally, sintering is the movement of atoms across a surface or through a material. Surface transport mechanisms, including evaporation-condensation and surface diffusion, are responsible for bonding particles; however, these mechanisms do not contribute to the densification of particle compacts.[25,27] Recent studies on nanocrystalline particle sintering have implied that surface diffusion mechanisms may be responsible for densification,[28,29] but this is beyond the scope of this review. Bulk transport mechanisms, including volume diffusion, grain boundary diffusion, and plastic flow, contribute to both bonding and densification during sintering. These mechanisms are described in more detail in the following sections. Viscous flow is a bulk transport mechanism present in amorphous systems, and is not described in this review.

2.1.1. Surface Transport Mechanisms

Evaporation-condensation and surface diffusion are the primary mechanisms of surface transport. In evaporation-condensation, surface atoms with a low enthalpy of vaporization are volatilized and deposited in another region,[25] or a secondary vapor phase may facilitate the removal of atoms from the surface.[30] In material systems with low vapor pressures, such as tungsten,[18] evaporation-condensation is not a significant contributor to surface transport.[25]

Surface diffusion is driven by defects on the surface of a material, including vacancies, adatoms, ledges, and kinks. Highly curved surfaces and high temperatures increase the density of these defects, which leads to greater surface diffusion.[25] Surface diffusion has been identified as the mechanism primarily responsible for initial sintering.[31] Other mechanisms, such as grain boundary diffusion, volume diffusion, and

plastic flow, may be active during initial sintering, and these are discussed in more detail in Section 2.2.1 of this thesis. The effects of surface diffusion are less pronounced as sintering progresses; however, surface diffusion may inhibit the mobility of pores during grain growth.[25]

2.1.2. Material Transport by Plastic Flow

Plastic flow is characterized by the motion of dislocations under stress, which is most often present in sintering with an applied pressure, sintering of highly-deformed powders, and sintering using rapid heating rates (greater than 10 ºC/min).[25,32-34] For plastic flow to contribute to the densification of a material, the dislocations must climb through the material, annihilating vacancies.[25] A more extensive review of plastic flow is addressed in Section 2.3.2.

2.1.3. Bulk Transport Mechanisms

Bulk transport by diffusion is often characterized as being volume diffusion or grain boundary diffusion. The rate of volume diffusion is controlled by the equilibrium vacancy concentration, the composition of the particles, and the surface stress of the curved surface.[25] During densification, vacancies diffuse from the neck to the grain boundary formed between two particles. At elevated temperatures, vacancies are annihilated by dislocation climb, resulting in densification of the particles.[25] Volume diffusion is typically not the dominant mechanism of sintering, except at temperatures close to the melting temperature, because the activation energy for volume diffusion is generally higher than surface diffusion or grain boundary diffusion.[25,27]

The misalignment and defect structure of crystals at the grain boundaries allows for mass flow, leading to bonding and densification. In pure metal systems, the grain

boundary width is typically on the order of a few atomic diameters.[35] Atoms may diffuse by dislocation motion through the grain boundaries in cases where significant pressures exist, such as in pressure-assisted sintering,[32,36] and these mechanisms are addressed in Section 2.3.3.

2.2. Stages of Sintering

Sintering is a complex process, and it is often described in three idealized stages. The first stage involves diffusion of atoms across the particle surfaces to form particle contacts. The second stage is dominated by the coalescence of pores and the coarsening of particles during densification. The final stage of sintering is dominated by grain growth and pore stabilization.[25,27] This review is not intended to be comprehensive, and the reader is referred to more complete reviews for a better understanding of the sintering process.[25,27]

2.2.1. Initial Stage Sintering

During the initial stage of sintering, particles in contact with one another will form a bonded region, or "neck," at the point of contact. In crystalline materials, neck growth occurs by diffusion of atoms from the surface of the particles,[31] from the grain boundaries, from the interior of the material, by the motion of dislocations (plastic flow and creep),[25] or by evaporation-condensation.[30] In a simplified model of two equal-sized spherical particles of radius r in contact with a neck of diameter x (Figure 2.1), the dominant sintering mechanism is related to the neck size ratio:

$$\left(\frac{x}{2r}\right)^n = \frac{Bt}{(2r)^m} \qquad 2.2$$

where $x/2r$ is the neck size ratio, B is a collection of material and geometric parameters, n and m are exponents that indicate the mechanism of sintering (Table 2.1), and t is the isothermal sintering time.[25]

Table 2.1. Initial stage sintering mechanisms for Equation 2.2 and their associated parameters for the sphere sintering model. (Table adapted from German.[25])

Mechanism	n	m	B
Plastic flow	2	1	$9\pi\gamma b D_v/kT$
Evaporation-condensation	3	2	$(3P_v/\rho^2)(\pi/2)^{1/2}(MW/kT)^{3/2}$
Volume diffusion	5	3	$80D_v\gamma a_o^3/kT$
Boundary diffusion	6	4	$20\delta D b\gamma a_o^3/kT$
Surface diffusion	7	4	$56D_s\gamma(a_o^3)^{4/3}/kT$

γ	= surface energy	MW	= molecular weight
b	= Burgers vector	a_o^3	= atomic volume
k	= Boltzmann constant	δ	= boundary width
T	= absolute temperature	D_v	= volume diffusivity
P_v	= vapor pressure	D_b	= boundary diffusivity
ρ	= theoretical density	D_s	= surface diffusivity

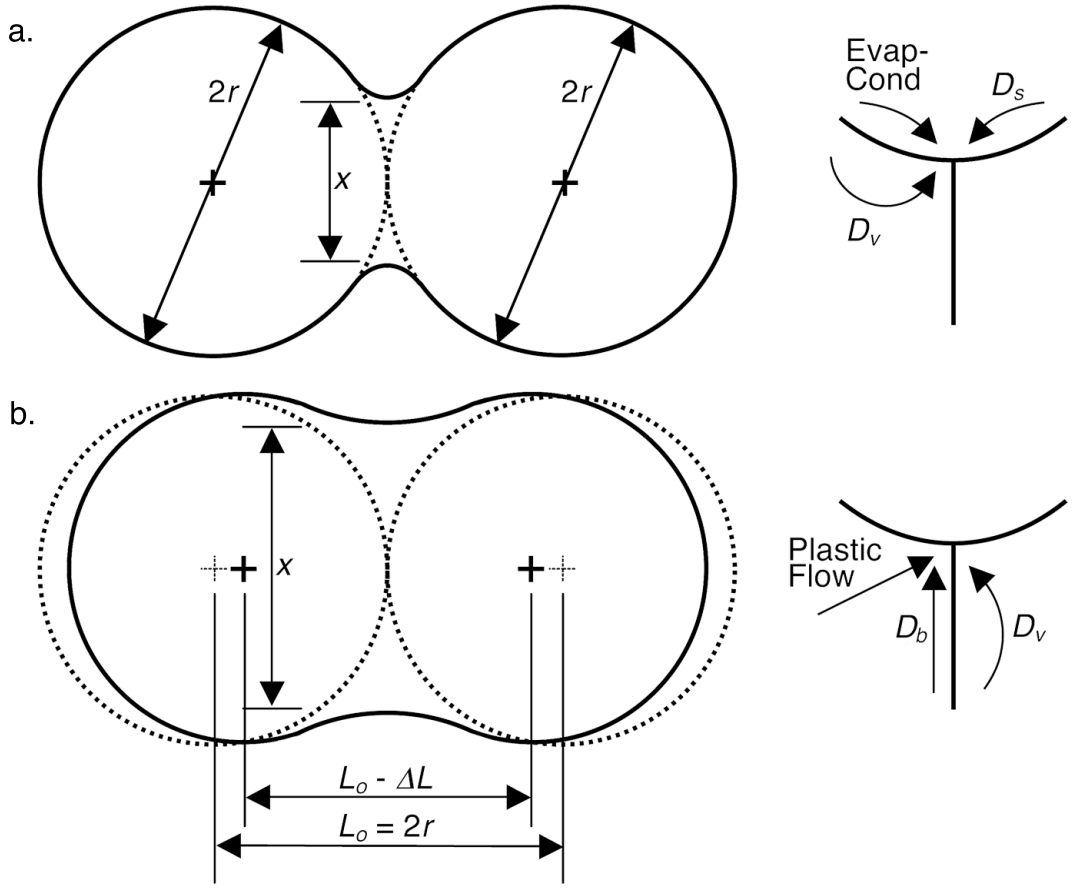

Figure 2.1. Initial stage sintering of two spheres and the possible mechanisms of sintering. Non-densifying mechanisms (a) that may be active during initial stage sintering are evaporation-condensation (Evap-Cond), surface diffusion (D_s), and diffusion of surface atoms through the bulk to the neck (D_v). Densifying mechanisms (b) include plastic flow, boundary diffusion (D_b), and lattice diffusion (D_v). (Figure adapted from German.[25])

Evaporation-condensation and surface diffusion do not contribute to densification in sintering, and densification occurs by lattice diffusion, boundary diffusion, or plastic flow. To model the shrinkage in initial stage sintering, the following equation is used:

$$\left(\frac{\Delta L}{L_o}\right)^{n/2} = \frac{Bt}{2^n (2r)^m} \exp\left(\frac{-Q}{kT}\right) \qquad 2.3$$

where ΔL is the change in the distance of the particle centers; L_o is the original distance between particle centers; B, n, and m are the same parameters given in Table 2.1; Q is the activation energy for the dominant mechanism; k is the Boltzmann constant; and, T is the absolute temperature of the system. It should be emphasized that the shrinkage during initial stage sintering is small, and once the neck size ratio is greater than 3%, the models presented above are not applicable; the models for intermediate stage sintering must be used.[25]

2.2.2. Intermediate Stage Sintering

Initial stage sintering is characterized by the growth of necks and negligible shrinkage. As sintering enters the intermediate stage, densification, pore rounding and elimination, and grain growth occur simultaneously. The intermediate stage of sintering is the least understood stage due to the complexity of grain growth and densification occurring simultaneously, and many different models exist to explain intermediate stage sintering.[25,37,38] The intermediate stage is driven by the coalescence of pores and the reduction in the surface area of the pores.[25] At this stage, the pores are assumed to be cylindrical and interconnected, and the geometry of the pore structure is dependent on the surface tension between the pores and the grains.[39] The fractional porosity of the structure can be estimated by:

$$\rho_p = \pi\left(\frac{d_{pore}}{G}\right)^2 \qquad 2.4$$

where ρ_p is the fractional sintered porosity, d_{pore} is the average pore diameter (assuming cylindrical pores), and G is the grain size.[25] As intermediate sintering continues, the pores continue to shrink until a critical value is reached at which point the pores are no longer connected.[25] Smaller pores along the grain boundaries continue to be eliminated due to grain boundary vacancy migration to larger pores, but near the end of intermediate stage sintering the pores contained within the grains are not eliminated.[25] As the pore structure collapses, grain growth becomes more active, and the relationship between the isothermal sintering time and the average grain size increases by a power relationship:

$$G^n = G_o^{\,n} + Kt \qquad 2.5$$

where G is the grain size at time t, G_o is the initial grain size, K is a thermally-activated parameter containing material-specific parameters, and n is dependent on the sintering mechanism and is typically close to 3.[25]

2.2.3. Final Stage Sintering

The transition from intermediate stage sintering and final stage sintering occurs when the pores, which were interconnected along grain boundaries, collapse and become isolated from one another.[25] Assuming all of the grains in a compact are uniform in size, the pores will begin to close at approximately 8% porosity.[25] In real sintering of materials, there exists a pore size distribution, and the pores will begin to close at about 15% porosity, and typically will be closed by 5% porosity.[25] The pores located at the grain triple junctions will begin to round to reduce the surface free energy between the pores and grains.

The cylindrical pores that remain along the grain boundaries become lenticular in shape, and the vertices of these lenses approach the equilibrium solid-vapor dihedral angle.[25] As the grain grows, the pore drags on the grain boundary, eventually breaking free of the boundary and becoming spherical within the grain.[25]

The closed pores have an associated pressure that slows down or prevents full densification of the sintered compact unless the pressure exerted on the compact exceeds the pore pressure.[37] Sintering in a vacuum reduces the pressure in the pores, and aids in final densification.[37] The change in porosity approaches zero during final stage sintering, and the rate of sintering can be modeled by the equation (assuming volume diffusion is the rate controlling mechanism):

$$\frac{d\rho}{dt} = 12\frac{D_v a_o^{\,3}}{kTG^2}\left(4\frac{\gamma}{d_{pore}} - P_{Pore}\right) \qquad 2.6$$

where $d\rho/dt$ is the densification rate, D_v is the volume diffusivity, $a_o^{\,3}$ is the atomic volume, k is the Boltzmann constant, T is the absolute temperature, G is the average grain size at time t, γ is the surface tension at the grain-pore interface, d_{pore} is the average diameter of the pores, and P_{pore} is the pressure inside the pores.[25] As the pore pressure increases, the densification rate is slowed, and if the pore pressure is equal to $4\gamma/d_{pore}$, the densification rate becomes zero.[25]

2.3. Sintering Mechanisms of Uniaxial Hot Pressing

The addition of an external pressure on a compact during sintering increases the stress between the particles, thereby increasing the driving force for densification. This greater stress increases the sintering rate, leading to lower sintering temperatures and shorter sintering times relative to sintering without an applied force.[25] In intermediate

and final stage sintering, the applied pressure aids in pore closure, resulting in a higher density material than may be achieved in pressureless sintering.[25,27]

Many processing methods have been developed to apply an external load during sintering: forging, extrusion, shock consolidation, hot isostatic pressing, reactive hot isostatic pressing, triaxial compression, and uniaxial hot pressing.[25] The focus of this section will be on uniaxial hot pressing; however, the principles of uniaxial hot pressing can generally be applied to other pressure-assisted sintering methods. More in-depth reviews of pressure-assisted sintering are contained in the literature,[25,27,37] and the following is only a brief review of pressure-assisted sintering.

2.3.1. Effective Pressure and Sintering Stress in Pressure-Assisted Sintering

During pressure-assisted sintering (e.g., hot isostatic pressing, uniaxial hot pressing, and spark plasma sintering), the applied pressure is distributed through a porous compact at the particle contacts, and the pressure at these contacts is higher than the applied pressure. This pressure is described as the effective pressure, and is related to the applied pressure:

$$P_E = \phi P_A \qquad 2.7$$

where P_E is the effective pressure, P_A is the applied pressure, and ϕ is the stress intensification factor.[27] During sintering, the particle contacts grow, diminishing the effective pressure, and as the compact approaches full density, the effective pressure approaches the applied pressure.

Multiple equations based on geometrical models have been developed to calculate the effective pressure in a compact. The most basic model assumes the pores in the compact are spherical and uniformly distributed. Based on this assumption, the stress

intensification parameter is directly related to the fractional density of the part, ρ, and can be estimated by $1/\rho$.[40] Other models for the stress intensification factor exist; however, Coble showed the differences between more complex models and the estimation of $1/\rho$ are negligible.[40]

The effective pressure increases the sintering stress, which increases the driving force for diffusion, and thus increases the sintering rate of the particles. By factoring the effective pressure into the Laplace stress given by Equation 2.1, the densification rate becomes:

$$\frac{d\rho}{dt} = B\left(\sigma + P_E\right)(1-\rho) \qquad 2.8$$

where $d\rho/dt$ is the densification rate, B is a collection of sintering and material parameters, σ is the sintering stress, P_E is the effective pressure, and ρ is the fractional density.[25,27] Applied pressures as low as 0.1 MPa can significantly increase the densification rate depending on the stage of sintering and the porosity of the material.[25,27]

2.3.2. Plastic Flow of Particles in Compression

In uniaxial constrained compression, such as what exists in a hot pressing setup, the proportion of the axial and radial stresses produces a shear component that is not present in pressureless sintering. This shearing effect produces plastic flow of the material as long as the effective pressure exceeds the temperature-dependent yield strength. Assuming plastic flow is the only mechanism responsible for densification, the final density may be estimated from the applied pressure by the equation:

$$\rho = \begin{cases} \left(\dfrac{(1-\rho_i)}{1.3\sigma_y(T)} + \rho_i \right)^{1/3} & \rho < 0.9 \\ 1 - \exp\left(-\dfrac{3}{2}\dfrac{P_A}{\sigma_y(T)} \right) & \rho \geq 0.9 \end{cases} \qquad 2.9$$

where ρ_{pf} is the fractional density obtainable by plastic flow, ρ_i is the fractional density of the green compact, P_A is the applied pressure, $\sigma_y(T)$ is the temperature-dependent yield strength of the particles, and ρ is the fractional density.[25] The yield strength of materials decreases with temperature, and initial densification is driven by plastic flow of the material.[25] During final stage sintering, plastic flow is responsible for the collapse of pores; however, the effective pressure must be greater than about three times the yield stress to obtain a fractional density of 0.99.[37]

Although grain size is not explicitly stated as a factor in Equation 2.9, plastic flow is a form of dislocation-controlled densification, and usually requires large grain sizes and high temperature.[37] The applicability of plastic flow to spark plasma sintering of submicron tungsten is discussed in Section 4.7.1 of this thesis. In the case of molten glasses or liquids, viscous flow is used to model the mass flow during hot pressing. Viscous flow models are not reviewed here, but can be found in the literature.[25,27]

2.3.3. Diffusion Mechanisms in Uniaxial Hot Pressing

Applying a pressure to a compact during sintering enhances the driving force for both volume diffusion and grain boundary diffusion.[40] Other diffusion-controlled densification mechanisms may also become active at higher temperatures and stresses, such as dislocation climb (power-law creep)[41] and grain boundary sliding.[42] The stress gradient between the grain boundaries in compression and the grain boundaries in tension

provides the driving force for atoms to diffuse from areas of compression to areas in tension (Figure 2.2).

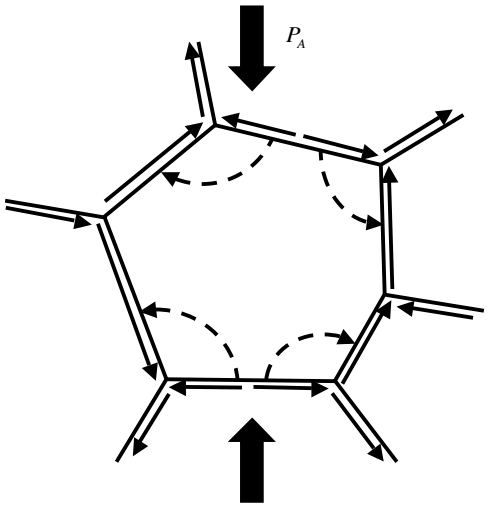

Figure 2.2. Direction of atomic flux when a uniaxial pressure is applied (P_A). When a force is applied, atoms diffuse perpendicular to the applied pressure by boundary diffusion (solid lines) or lattice diffusion (dashed lines).

These densification mechanisms are analogous to the mechanisms for creep, and creep models have been modified to describe sintering. In uniaxial hot pressing, the mass of the starting powder, M, and the cross-sectional area, A, are constant during sintering, and the height of the sample, h, varies. The sintered density of the sample, ρ, is then a function of the sample height, $\rho = M/(A \times h)$. From this relationship, the sample height and sample density are directly related:

$$h\rho = h_i\rho_i = h_f\rho_f \qquad 2.10$$

where h_i and h_f are the initial and final heights, respectively, and ρ_i and ρ_f are the initial and final densities, respectively. Differentiating Equation 2.10 with respect to time and rearranging the equation yields:

$$-\frac{1}{h}\frac{dh}{dt} = \frac{1}{\rho}\frac{d\rho}{dt} \qquad 2.11$$

where the left-hand side of the equation is the definition of a linear strain rate, and the right-hand side is the normalized densification rate.[40] The models for volume diffusion creep (Nabarro-Herring creep) and grain boundary diffusion creep (Coble creep) can then be directly applied to densification during uniaxial hot pressing:

$$\frac{1}{\rho}\frac{d\rho}{dt} = \frac{40}{3}\frac{D_v a_o^{\,3}}{G^2 kT} \qquad 2.12$$

$$\frac{1}{\rho}\frac{d\rho}{dt} = X\frac{D_b a_o^{\,3}}{G^3 kT} \qquad 2.13$$

where D_v and D_b are the volume and grain boundary diffusivities, respectively, $a_o^{\,3}$ is the atomic volume of the material, G is the grain size, k is the Boltzmann constant, T is the absolute temperature, and X is a geometric constant equal to 95/2 for intermediate stage sintering and 15/2 for final stage sintering.[40] Coble incorporated the influence of applied pressure and surface energy into the creep models in Equation 2.12 and Equation 2.13, respectively:

$$\frac{1}{\rho}\frac{d\rho}{dt} = \frac{40}{3}\frac{D_v a_o^{\,3}}{G^2 kT}\left(\frac{P_A}{\rho} + c\frac{\gamma}{r}\right) \qquad 2.14$$

$$\frac{1}{\rho}\frac{d\rho}{dt} = X\frac{D_b a_o^{\,3}}{G^3 kT}\left(\frac{P_A}{\rho} + c\frac{\gamma}{r}\right) \qquad 2.15$$

where P_A is the applied pressure, c is a constant equal to 1 for intermediate stage sintering and 2 for final stage sintering, γ is the surface energy of the material, and r is the radius of

the particles.[40] The models in Equations 2.14 and 2.15 were used in Section 4.7.2 to evaluate the nonisothermal densification kinetics of spark plasma sintered tungsten.

A similar approach to converting linear strain rate to densification rate in uniaxial hot pressing may be applied to the model for power-law creep. Power-law creep occurs when the temperature and stress are high, enabling climb and glide of dislocations.[43] The semi-empirical model of power-law creep is given by:

$$\frac{1}{\rho}\frac{d\rho}{dt} = A^* \frac{D_v \mu(T) b}{kT}\left(\frac{P_A}{\mu(T)\rho}\right)^n \qquad 2.16$$

where $\mu(T)$ is the temperature-dependent shear modulus, b is the Burgers vector, n is the stress sensitivity exponent, and A^* is the Dorn parameter for shear stress.[43] A^* is approximately $(3^{(n+1)/2})\times A$, where A is the Dorn parameter for tensile stress. Both the Dorn parameter and the stress sensitivity exponent are based on experimental measurements of steady state creep of a material.[25] The shear modulus is temperature dependent, and is estimated by the equation:

$$\mu(T) = \mu_o\left(1 + \frac{(T-300)}{T_m}\frac{T_m}{\mu_o}\frac{d\mu}{dT}\right) \qquad 2.17$$

where μ_o is the shear modulus at 300 K, T_m is the melting temperature of the material, and $(T_m/\mu_o)(d\mu/dT)$ is the temperature dependence of the modulus.[44]

2.4. Sintering Maps and Pressure Sintering Maps

Sintering maps and pressure sintering maps are visual tools that help determine the rate-limiting densification mechanism of sintering at a given temperature, density, grain size, and pressure (in pressure-assisted sintering). Ashby derived the first sintering maps to help determine the mechanism of neck growth in sintering particles.[45] To

construct these maps, Ashby used models for surface diffusion, lattice diffusion, boundary diffusion, and vapor transport.[45] Swinkels and Ashby modified the original model for sintering maps by constructing diagrams in which the sintering models have been plotted as functions of density and temperature.[46] Sintering maps for tungsten with a grain size of 2 μm were produced by Ashby[45] and Swinkels and Ashby[46] (Figure 2.3).

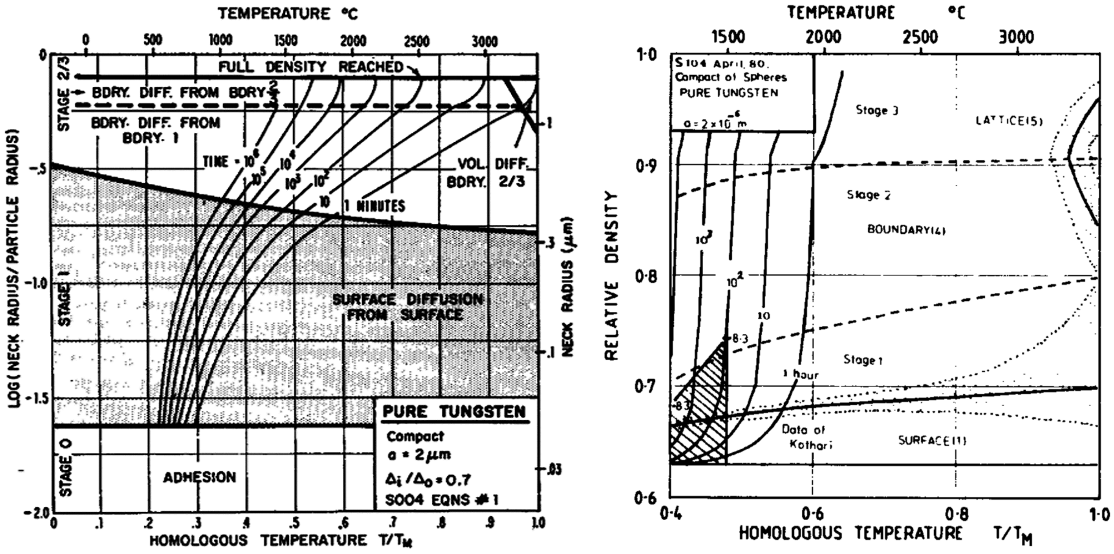

Figure 2.3. Sintering maps of tungsten produced by Ashby[45] and Swinkels and Ashby.[46] The regions between the bolded lines are labeled with the dominant sintering mechanism for a given neck-to-particle-size and sintering temperature (left) or a given density and sintering temperature (right). (Figures reproduced by permission from the publisher.)

Wilkinson and Ashby incorporated applied pressure into sintering maps, allowing pressure-assisted sintering maps to be constructed.[47] These diagrams, referred to as pressure sintering diagrams, were constructed assuming four densification mechanisms are active during pressure-assisted sintering: volume diffusion, boundary diffusion, plastic flow, and power-law creep.[47] In this thesis, pressure-sintering maps were

constructed for tungsten based on volume diffusion, boundary diffusion, and power-law creep. Due to the complexities and uncertainties in the proposed SPS densification models, only known densification mechanisms were used. The pressure sintering maps constructed in this study are presented and discussed in Section 4.7.3.

2.5. Application of an Electric Current During Pressure-Assisted Sintering

2.5.1. History of Pressure-Assisted Sintering with an Electric Current

Green-body sintering and pressure-assisted sintering techniques traditionally rely on external heating elements to raise the temperature of the furnace to sintering conditions. Disadvantages of these techniques include slow heating rates and long sintering times to reach high densities. An alternative to sintering by an external heat source is to directly heat the powder compact during sintering. To do this, direct resistance heating of the compact powder (or die material, if the powder is insulating) is performed by the application of an electric current to the compact and die.

In 1922, Sauerwald reported the earliest experiments in direct resistance heating and simultaneous application of pressure to a powder compact.[48] Sauerwald placed a green compact of tungsten between two carbon electrodes, and applied a uniaxial force in conjunction with a current regulator used to control the temperature of the powder compact.[48] The tungsten powder was densified by this technique with a maximum measured temperature of 2000 ºC.[48]

The first electric current sintering patent was awarded to Taylor in 1933.[49] The patent was exclusively for the production of cemented carbides by the direct application of an electrical current.[49] In the patent, a glass or ceramic hollow tube was used to

contain loose powders, and electrodes were placed on both ends of the powder and a high-current, low-voltage source was used to resistively heat the parts.[49] The patent does not mention the current density used to densify the parts, but it does mention temperatures in excess of 1000 ºC are produced by the sintering apparatus.[49] The time required to sinter the cemented carbides is not mentioned explicitly, but Taylor implies the current is only applied for a second or less.[49] The apparatus described by Taylor relies on atmospheric or low applied pressures on the top punch to maintain electrical contact with the powders during sintering.[49]

Another patent, awarded in 1944 to Cremer, described the use of a uniaxial die setup connected to an alternating current power source to densify nonferrous metallic powders.[50] The apparatus uses a metallic die coated with non-conductive particles, specifically aluminum powders coated with stearic acid.[50] According to the patent, this non-conductive coating forces the electrical current to travel from the punches through the sample.[50] This patent specifies an alternating current at 60 Hz applied for one or two cycles bonds the metallic powders.[50]

A year later, another current-assisted hot pressing patent submitted by Ross was approved.[51] The machine described was for production of ferrous powder metallurgy products, and was designed to have four non-conductive dies used in tandem.[51] Unlike previous patents and reported current-assisted sintering techniques, this patent was the first source to mention pulsing the electrical current.[51] The reasons for a pulsed current were to reduce the heating of the die material and to better control the temperature relative to a continuously-supplied current.[51] Although the patent makes these claims, no

data or direct comparisons to ferrous materials sintered by a continuous current are given.[51]

In 1955, Lenel connected a specially-made spot welding power supply to two pressure cylinders.[52] The dies used were made from brass with a ceramic insert to prevent current flow through the die body.[52] The punches were constructed from a copper alloy.[52] To prevent the metal powders from sintering to the copper, metal wafers made of Monel, steel, molybdenum, or tungsten were placed between the punch and metal powder.[52] The powders were sintered using a single 1/60 sec pulse of single-phase alternating current followed by 1/60 sec of no current.[52] This cycle was repeated between 2 and 30 times to produce high-density metal parts.[52] Lenel states that current densities between 25,000 and 125,000 A/in^2 (approximately 3900 and 19,000 A/cm^2) in 10 to 30 cycles are required to sinter compacts of 0.5 in diameter (1.27 cm).[52] A variety of sintered metals were produced by this method, including zirconium, molybdenum, brass, and commercial alloys.[52]

During the 1960s, Inoue filed two patents[53,54] related to current-enhanced hot pressing, and made multiple claims about the mechanisms of the process. Inoue claimed the electrical current forms a "spark" effect between particles, leading to the ionization of the particulate surfaces, and enhancing sintering.[53,54] The patents also claimed the large current forces the particles into contact, and these forces largely outweigh any effects of an applied force on the compacts during densification.[53,54] Although Inoue does not provide direct evidence of a spark discharge within the powders, sparking has been repeatedly cited in the literature as enhancing sintering.[16,55-59] Despite the lack of

evidence of sparking in current sintering processes, this method of sintering is commonly referred to as spark plasma sintering (SPS).[14,60]

Other names for this process and similar processes include plasma pressure compaction (P^2C),[61] plasma-activated sintering (PAS),[16,62] pulsed electric current sintering (PECS),[63,64] and the field-assisted sintering technique (FAST).[55,58,59,65] Recent papers on the fundamentals of this process have disputed the existence of a spark or plasma,[14,60,66,67] and alternative models have been proposed to explain the sintering enhancement effects of current and temperature gradients.[1,15,68] Although electric current pressure-assisted sintering may not produce a spark or plasma, this process will be referred to as spark plasma sintering for the remainder of this work.

2.5.2. Spark Plasma Sintering Process

The spark plasma sintering uses a pulsed high direct current (up to 5000 A) and low voltage (less than 5 V) applied simultaneously with a uniaxial force (typically 5-50 kN) on metallic or ceramic powders in a die.[14] Graphite is often used for the die and punch material because graphite maintains high strength at high temperatures and it is electrically conductive.[14,66] The die-and-punch assembly is situated between two water-cooled electrodes, and the system is contained within an atmosphere-controlled chamber (Figure 2.4). A mechanical pump is used to maintain a vacuum of about 1 Pa; however, the chamber can also be evacuated further with a diffusion pump, or the chamber may be filled with an inert gas such as argon. During the SPS process, force is applied to the punches. This force is used to promote consolidation of the powder compact, as well as maintaining electrical contact with the die, thereby preventing short-circuiting of the system.[14]

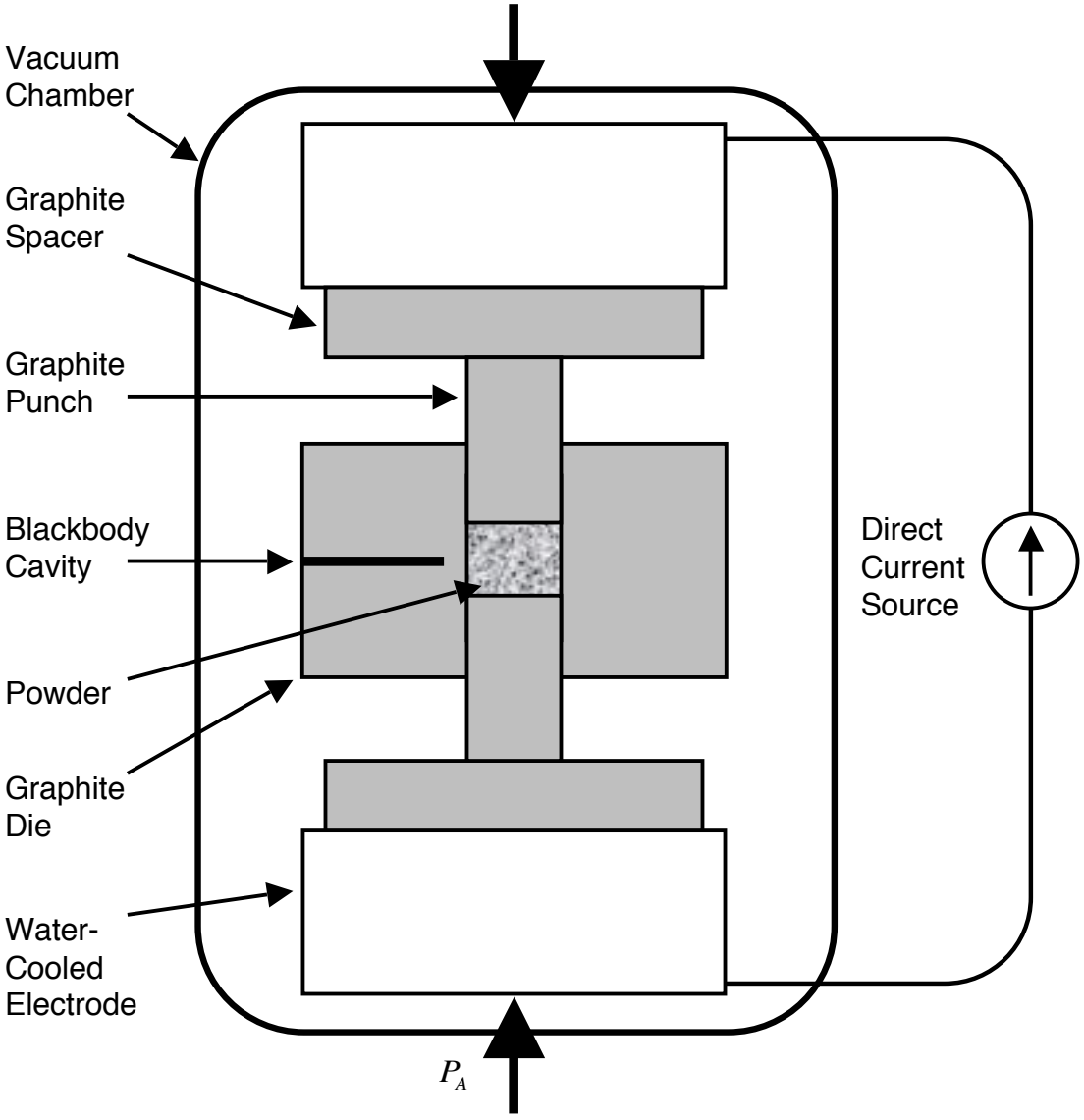

Figure 2.4. Schematic representation of the SPS setup. The powder is pressed with force P_A and heated using a pulsed direct current. The temperature is measured by an infrared thermometer focused on the blackbody cavity.

2.5.3. Spark Plasma Sintering of Metals, Ceramics, and Composite Powders

SPS is advantageous for the production of many materials that are otherwise difficult to produce by other sintering techniques. Direct heating of the die and powder allows rapid heating as high as 1000 ºC/min, rapid quench times, and typically reduces sintering times from hours to minutes.[14] These advantages are also coupled with reported lower sintering temperatures,[66] improved mechanical properties,[29,69,70] and smaller grain sizes.[71,72] Although metals with native oxide layers can be difficult to sinter without sintering aids, aluminum[16] and tungsten[55] powders have been sintered in their pure forms using SPS. In these metal studies, the grain boundaries were found to be free of oxides and other impurities, which has been attributed to a surface cleaning effect of the SPS process.[55,58]

In addition to powder metal compacts, ceramic powders can be rapidly consolidated by SPS. In non-conductive powders, the current pathway is through the die body, and the heat from the die diffuses towards the center of the ceramic powders.[73] The application of high pressures and high heating rates has been used to produce fully-dense ceramics with average grain sizes as small as 10 nm.[74] The vacuum environment and graphite dies used in SPS result in a reducing atmosphere, and many oxide ceramics exhibit strong shifts in stoichiometry near the die-compact interface.[73]

Composite systems including alumina-carbon,[75] zirconia-based systems, silicon carbide-molybdenum disilicide, and silicon nitride-titanium nitride have been produced by SPS.[76] In addition to ceramic-ceramic composites, cermets have also been produced using SPS. Some of these cermet systems include tungsten mixed with rare earth oxides[77] and aluminum with silicon carbide.[76]

2.5.4. Proposed Mechanisms of Sintering Enhancement in Spark Plasma Sintering

Direct current resistance sintering was originally reported to be a product of Joule heating,[48] and was later attributed to a spark-discharge between particle contacts.[53,54] A current arc (spark) or plasma between the surfaces of the metallic particles was thought to form during SPS, and this arc would aid in neck formation and sintering.[16,55] This concept of a spark-discharge causing the bonding and sintering of particles was accepted without evidence for a spark-discharge actually occurring, and this concept has come under experimental scrutiny in recent studies of the SPS process.[14,60,66,67,73] For a plasma to form, the atoms in a material must become ionized; to do this, free electrons must be generated and then accelerated by an electric field to the required energy for ionization.[60] The energy required to produce an arc between particles requires about 20 V and a current of at least 10 A, and other discharge phenomena require much higher potentials and currents.[60,78] Typical commercial SPS units operate at less than 5 V, so the potential required to create a discharge is not present in the SPS process.[60] Experiments using atomic emission spectroscopy, high-speed voltage measurements, and direct observation have shown no evidence of electrical discharge during SPS.[60]

The presence of an electrical current can enhance the chemical potential for the mass transport of atoms, accelerating the rate of sintering.[68,79] Because the current also contributes directly to heating of the sample (ohmic heating), the influence of electromigration is difficult to resolve.[79] Although current can increase the diffusion rate, in a study by Anselmi-Tamburini *et al.*, the activation energy for the formation of molybdenum disilicide by SPS was in agreement with the activation energy of formation in the absence of current.[67] The effect of an electron-wind force, whereby atoms move in

the direction of the current due to momentum transfer from the electrons to the atoms, does not contribute significantly to mass transport in SPS.[68]

Kornyushin modeled the effects of an applied electrical current during sintering, and the model shows that the initial application of current leads to sharp differences in the temperature at different locations in the powder compact.[80] As the temperature gradient is increased, the thermal diffusion rate of vacancies is increased.[80] Based on modeling work by Olevsky and Froyen, the influence of local thermal gradients by rapid heating has a more profound effect on the sintering of particles in SPS than the applied current[1]; however, no experimental work has been published showing enhanced densification in SPS is due to the electrical current or thermal gradients.

Kornyushin derived a relationship between the sintering rate and the diffusion mechanisms responsible for sintering.[80] In his derivation, Kornyushin attributed the densification to contributions from conventional mechanisms of sintering, local temperature gradients, and surplus vacancies formed during current-assisted sintering.[80] According to the model by Kornyushin, current pulsing increases the equilibrium concentration to vacancies.[80] As the vacancy concentration increases, the mean free path between vacancies is decreased, allowing atoms to diffuse faster through the lattice.[80] This enhanced diffusion results in an increase in the sintering rate.[80] Experimental work on the effect of current pulsing on a molybdenum-silicon interface showed the growth of the molybdenum disilicide layer was independent of the pulse pattern.[66] No papers are currently available in the open literature that experimentally show current pulsing enhances the kinetics of sintering.

2.6. Sintering of Tungsten

Tungsten has the highest melting point (3422 ºC) and the lowest vapor pressure of pure metals.[18] These properties, coupled with high tensile strength and good creep resistance, make tungsten and its alloys important in applications requiring mechanical stability at high temperatures.[81] Applications of pure tungsten include light bulb filaments, electron emission sources, rocket nozzles, and nuclear fuel cladding.[18] The high melting point of tungsten prevents practical casting, and tungsten is typically processed by powder metallurgy techniques. Conventional sintering of pure tungsten is commonly performed in a hydrogen atmosphere at temperatures greater than 2000 ºC.[18] At temperatures below 2000 ºC it can take more than 50 hours to sinter tungsten to 90% density.[18] Pressure-assisted sintering techniques are used to reduce the sintering time and sintering temperature of tungsten.[82,83] Tungsten may also be alloyed with nickel and iron and processed by liquid-phase sintering.[84] Tungsten alloys sinter by different mechanisms than pure tungsten and are not covered in this review.[25]

2.6.1. Diffusion-Controlled Transport Mechanisms in Tungsten

As stated in Section 2.1, the diffusion-controlled sintering mechanisms include evaporation-condensation, surface diffusion, boundary diffusion, lattice diffusion, and power-law creep. Surface diffusion in tungsten has been studied primarily in relation to field-emission applications[85,86] and light bulb filaments.[87] Radioactive tracers were used to study boundary diffusion and lattice diffusion in tungsten. Boundary diffusion was studied by Kreider and Bruggeman,[88] and lattice diffusion was studied by Andelin *et al.,*[89] and Pawel and Lundy.[90] The activation energy for tungsten creep was studied by Green,[91] King and Sell,[92] and Robinson and Sherby.[93] A summary of the diffusion-

controlled mechanisms in tungsten, including the temperature ranges studied and the activation energies for these mechanisms, is given in Table 2.2 at the end of this section.

Tungsten has the lowest vapor pressure of the pure elements, and evaporation-condensation does not contribute significantly to mass transport in pure tungsten.[18] In the presence of oxygen or water vapor, mass transport of tungsten by evaporation-condensation does occur and leads to enhanced grain growth.[18,94] In this thesis, tungsten was sintered in a vacuum environment, and the effects of evaporation-condensation were assumed insignificant relative to other mass transport mechanisms.[95]

Barbour *et al.*,[86] Bettler and Charbonnier,[85] and Ehrlich and Hudda[96] studied the surface diffusion of tungsten using field emission microscopy. In the study by Barbour *et al.*, the activation energy of surface migration was determined to be 301 kJ/mol using pulsed field emission microscopy on a tungsten field emitter tip.[86] The applied electric field was pulsed, and assumed to have a negligible effect on the surface diffusion of tungsten atoms relative to the thermal diffusion of atoms between 1527 and 2427 ºC.[86] Bettler and Charbonnier investigated the effect of high electric fields on the surface diffusion of tungsten.[85] In a high electric field with potentials exceeding 8000 V, the activation energy for self migration of tungsten was reduced from 301 kJ/mol[86] to 269 kJ/mol for the (100), (110), and (211) planes at temperatures from 1427 to 1827 ºC.[85] Bettler and Charbonnier concluded that the activation energy is lowered by the polarization of surface atoms in a high electric field, and the activation energy required to cause transport of surface atoms is lowered.[85] Ehrlich and Hudda investigated the activation energy of adatom diffusion for the (110), (321), and (211) planes at -253 ºC,

and found the self-diffusion activation energies were 92, 84, and 54 kJ/mol, respectively.[96]

Peacock and Wilson studied the surface diffusion of tungsten using tungsten light bulb filaments in a 250 V/m electric field, with a 500 MA/m^2 current density, and at 1762 ºC.[87] In this study, the surface migration activation energy was measured to be 232 kJ/mol. The decreased activation energy in relation to the activation energy found by Barbour *et al*.[86] was attributed to the effects of the electric field and high temperature,[87] which is in agreement with the findings of Bettler and Charbonnier.[85]

Bowden and Singer studied the self-diffusion of tungsten along the (100) plane and in the <110> direction using single crystal tungsten heated to between 2287 and 2877 ºC.[97] The researchers found the activation energy for surface diffusion to be 536 kJ/mol, and the difference in activation energy between their study and the study by Barbour *et al*.[86] was attributed to a change from vacancy diffusion to adatom diffusion.[97]

Bulk transport mechanisms in tungsten include grain boundary diffusion, volume diffusion, and power-law creep.[91-93,98] Kreider and Bruggeman used radioactive tracer diffusion on polycrystalline tungsten to determine the activation energy for grain boundary diffusion in tungsten.[88] A 1 μm layer of radioactive W^{185} was deposited on swaged polycrystalline tungsten, and the samples were then annealed for up to 10 hours at temperatures between 1400 and 2200 ºC.[88] Removal of 1 to 2 μm of material from the surface was performed, followed by the use of a Geiger-Müeller counter to measure the activity of the W^{185}, and the procedure was repeated until no radioactive tungsten was present in the sample.[88] Using this method, the activation energy for tungsten grain boundary diffusion was calculated to be 385 kJ/mol.[88] According to the authors, the

diffusion rate and activation energy of the radioactive tracers appeared to be independent of whether the grain boundaries were high angle (>15º) or low angle boundaries.[88] The activation energy for grain boundary diffusion found by Kreider and Bruggeman is in agreement with the activation energy for pressureless sintering of tungsten, and is described in greater detail in Section 2.6.2.[95,99-102]

Andelin *et al.* used radioactive tracers to measure the self-diffusion of tungsten through the lattice.[89] Single crystals of tungsten were bombarded by deuterons to produce W^{185} on the surface of the tungsten, and the samples were annealed from 2660 to 3230 ºC.[89] Similar to the grain boundary diffusion experiments, the activity of W^{185} was measured to determine the self-diffusivity of tungsten, and the activation energy was measured to be 641 kJ/mol.[89] Pawel and Lundy performed a similar experiment with radioactive tungsten tracers to determine the self-diffusion activation energy of tungsten.[90] The samples were annealed between 1300 ºC and 2400 ºC, and the activation energy for self-diffusion of tungsten was found to be 587 kJ/mol.[90]

Stress fields produced by externally applied forces also contribute to the mass transport of tungsten at high temperatures and high pressures. The measured values of the creep activation energy vary widely in the literature, depending on the strain rate and temperature at which the tests were performed. Green produced swaged tungsten parts and creep tested them from 2250 to 2800 ºC at strain rates between 6×10^{-7} and 10^{-3} s^{-1}, and the activation energy of creep was found to be 670 kJ/mol.[91] The high activation energy was attributed to the high melting point of tungsten.[91] King and Sell creep tested swaged tungsten at temperatures from 800 to 2400 ºC to determine the activation energy of creep.[92] Stresses between 17 and 138 MPa and strain rates between 8.4×10^{-5} and

3.3×10^{-2} s^{-1} were applied in the creep tests, and the activation energies were found to be dependent on the applied stress, and varied from 301 kJ/mol to 565 kJ/mol.[92] A re-evaluation of tungsten creep data by Robinson and Sherby was performed to account for the change in elastic modulus as a function of temperature, and the mechanism of creep was found to change at about 2200 ºC.[93] Robinson and Sherby found that at temperatures between 1200 and 2200ºC the activation energy for creep is 376 kJ/mol, and above 2200 ºC the activation energy for creep is 140 kJ/mol.[93] From these results and later creep testing by King,[98] it was found that power-law creep breaks down at high stress, and the creep properties are not controlled by a dominant mechanism over a wide range of stresses or temperatures.

Table 2.2. Summary of surface, boundary, lattice, and creep self-diffusion mechanisms in tungsten.

Mechanism	Temperature (ºC)	Diffusion constant* (m^2/s)	Activation energy (kJ/mol)	Source	Comments
Surface diffusion	-253	2×10^{-11}	54	Ehrlich and Hudda[96]	(211) plane
	-253	1×10^{-7}	84	Ehrlich and Hudda[96]	(321) plane
	-253	3×10^{-6}	92	Ehrlich and Hudda[96]	(110) plane
	1427-1827	-	269	Bettler and Charbonnier[85]	(100), (110), (211) planes, high electric field
	1527-2427	4×10^{-4}	301	Barbour *et al.*[86]	(100), (110), (211) planes
	1762	-	232	Peacock and Wilson[87]	High electric field
	2287-2877	7.6×10^{1}	536	Bowden and Singer[97]	(100) plane
Boundary diffusion	1400-2200	3.3×10^{-3}	385	Kreider and Bruggeman[88]	Tracer diffusion
Lattice diffusion	1300-2400	1.9×10^{-4}	587	Pawel and Lundy[90]	Tracer diffusion
	2660-3230	4.3×10^{-3}	641	Andelin *et al.*[89]	Tracer diffusion
Creep	800-2400	-	301-565	King and Sell[92]	Strain rate = 8.4×10^{-5} to 3.3×10^{-2} s^{-1}
	1200-2200	5.6×10^{-4}	376	Robinson and Sherby[93]	Attributed to lattice diffusion
	2250-2800	-	670	Green[91]	Strain rate = 6×10^{-7} to 1×10^{-3} s^{-1}
	2200-2800	1×10^{-7}	140	Robinson and Sherby[93]	Attributed to dislocation diffusion

* = Diffusion constant not available for all studies

2.6.2. Pressureless Sintering and Pressure-Assisted Sintering of Tungsten

Sintering of green tungsten compacts was studied primarily in the 1960s, and limited studies on uniaxial hot pressing were performed during the 1970s. Due to the technical limitations and practicality of producing fully-dense tungsten,[103] much of the research on tungsten became focused on tungsten heavy alloys. Since many of these alloys rely on a liquid phase to promote sintering, the dominant mechanism is different than in pure tungsten sintering,[25] and these alloys are not covered in this review. A summary of the activation energies and proposed mechanisms of tungsten sintering is given at the end of this section in Table 2.3.

Extensive tungsten sintering research was performed by NASA during the 1960s.[104] For tungsten parts that were pressed into green compacts and then sintered, the parts were pre-sintered between 1100 and 1300 ºC by indirect heating, and then self-resistance sintered to 90% theoretical density.[104] The parts were then forged into the shapes necessary for their applications.[104] NASA also worked with hot pressing of tungsten, however the short die lifetimes and the required machining to remove the carburized surfaces were cost prohibitive in most circumstances.[104] For the hot pressing performed by NASA, tungsten powders were sintered from 1500 to 1800 ºC, and pressures of 34.5 to 55.2 MPa were used for tungsten powders less than 5 μm in diameter.[104]

Pugh and Amra studied vacuum sintering of tungsten powder between 1800 and 3100 ºC.[105] Tungsten powders with an average particle size of 4.53 μm were cold pressed and presintered for 60 min at 1200 ºC in a hydrogen atmosphere.[105] The tungsten ingots were then moved to a vacuum furnace and up to 720 kW of power was applied to

the ingots to heat them at 20 ºC/min to a maximum temperature between 1800 and 3100 ºC; the ingots were sintered at maximum temperature between 15 and 480 min.[105] The researchers calculated the apparent activation energy for sintering tungsten, and they found that the activation energy changes during sintering from 230 kJ/mol at a fractional density of 0.80 to 440 kJ/mol at a fractional density of 0.96.[105] In the study, it was noted that there was not great precision in determining the activation energies, and no rate-limiting mechanisms for tungsten sintering were proposed.[105]

The mechanism of sintering in tungsten at low temperature was investigated by Hayden and Brophy.[106] In this study, pure, submicron tungsten powder was first formed into compacts by cold pressing, and then sintered isothermally between 1050 and 1200 ºC.[106] The tungsten compacts were sintered between 30 and 240 min in a purified hydrogen atmosphere.[106] Hayden and Brophy evaluated the kinetics of sintering by measuring the linear shrinkage of the parts as a function of time, and found the shrinkage fit the two-sphere sintering model for boundary diffusion.[106] The researchers derived an activation energy of 380 kJ/mol from the linear shrinkage data, and the mechanism of densification was speculated to be boundary diffusion.[106]

Kothari studied both the densification[95] and the grain growth[101] of tungsten sintering. Densification experiments were performed between 1100 and 1500 ºC in vacuum furnaces.[95] Kothari used two different methods to calculate the activation energy for densification of tungsten between 1100 and 1500 ºC, and both methods yielded an activation energy of 420 kJ/mol.[95] Based on this activation energy, Kothari concluded boundary diffusion is likely the rate-limiting mechanism of sintering between 1100 and 1500 ºC.[95] In a separate paper, Kothari found that below 1400 ºC tungsten grain growth

is negligible, but between 1425 and 1650 ºC, the activation energy for grain growth is 385 kJ/mol, which is in agreement with the activation energy of boundary diffusion.[101]

Vasilos and Smith studied tungsten sintering kinetics between 1300 and 1750 ºC, and found the activation energy for sintering to be about 465 kJ/mol.[99] The diffusivities found in this study were compared with tungsten tracer diffusion performed between 2100 and 2600 ºC in tungsten single crystals.[99] The diffusion rates for tungsten sintering were found to be more than five orders of magnitude faster than the tracer diffusion.[99] Vasilos and Smith concluded that the faster diffusivity found in tungsten sintering was likely due to boundary diffusion.[99]

Chen investigated the sintering kinetics of tungsten and tungsten with dispersions of ceria and hafnia between 1000 and 1750 ºC.[102] The experiments were performed using a dilatometer to measure shrinkage of the parts during sintering. [102] Chen used heating rates of 2, 5, 10, and 20 ºC/min to determine the sintering rates for tungsten, tungsten with 1 wt% ceria, and tungsten with 1 wt% hafnia.[102] Using the sintering rate curves, Chen found the activation energy for tungsten densification was 318±21 kJ/mol for a starting powder size of 1.2 μm.[102] In the experiment with tungsten with 1 wt% ceria, the activation energy for densification was determined to be 385±15 kJ/mol.[102] Chen attributed the higher activation energy for tungsten with 1 wt% to the ceria particles wetting to the surface of the tungsten, which formed a diffusion barrier between the tungsten particles.[102] The activation energy found in this study was compared to the activation energies of lattice diffusion, boundary diffusion, and surface diffusion in tungsten, and Chen concluded the likely rate-controlling densification mechanism was boundary diffusion for both pure tungsten and tungsten with 1 wt% ceria.[102]

Karpinos *et al.* studied hot pressing of tungsten between 1800 and 2300 ºC.[82] After 30 minutes of isothermal sintering, the tungsten parts were to between 70.5 and 94.0% dense.[82] The researchers determined the densification mechanisms of hot pressing of tungsten are separated into three regimes: between 45 and 58% dense, particle rearrangement is dominant; between 58 and 75% dense, plastic flow is dominant; and above 80% dense, boundary diffusion is dominant.[83] The researchers determined the activation energies for the three regimes were 50±4, 140±4, and 414±13 kJ/mol, respectively.[83] Karpinos *et al.* also reported reactions between the graphite dies used and the tungsten powders.[107] For tungsten hot pressed between 1800 and 2300 ºC for 60 min with an applied pressure of 15 MPa, a tungsten carbide layer formed that was between 200 and 1000 μm.[107] The researchers concluded that the diffusion of carbon into tungsten beyond the carbide layer was negligible, and that the carbide thickness could be reduced by using higher heating rates.[107]

Table 2.3. Summary of the apparent activation energies and proposed rate-limiting mechanisms in sintering and hot pressing of tungsten.

Temperature range (ºC)	Activation energy (kJ/mol)	Proposed rate-limiting mechanism	Source	Comments
1000-1750	318±21	Boundary diffusion	Chen[102]	Dilatometry study using 1.2 μm tungsten
1050-1200	380	Boundary diffusion	Hayden and Brophy[106]	Activation energy found by linear shrinkage
1100-1500	418±20	Boundary diffusion	Kothari[95]	Activation energy found by volume shrinkage and degree of sintering
1300-1750	465	Boundary diffusion	Vasilos and Smith[99]	Activation energy found using model by Coble[39]
1800-3100	440	None given	Pugh and Amra[105]	Activation energy for 95% dense tungsten
1800-2300	50±4	Particle rearrangement	Karpinos *et al.*[82]	Activation energy for 45-58% dense tungsten
1800-2300	140±4	Plastic flow	Karpinos *et al.*[82]	Activation energy for 58-75% dense tungsten
1800-2300	414±13	Boundary diffusion	Karpinos *et al.*[82]	Activation energy for >80% dense tungsten

2.6.3. Electrical Resistance Sintering of Tungsten for Industrial Use

During the 1950s, the General Electric Company produced fully-dense, pure tungsten bar stock by passing an electrical current through tungsten powder compacts.[108] This method of sintering was referred to as “direct sintering” in the tungsten industry.[18,108] Prior to final sintering, pressed powder bars were presintered at temperatures between 1100 and 1300 ºC in dry hydrogen, and then transferred to water-cooled copper bell jars, where they were direct sintered to high densities.[108] The copper bell jars were designed to have an upper tungsten electrode that could move during sintering as the tungsten bars contracted.[18] Dry hydrogen was flowed through the bell

jars during sintering.[108] For large tungsten bars, up to 50,000 A of direct current was applied to the bars for 20 to 45 minutes.[108] During this sintering process, the tungsten bars reached approximately 3000 ºC and contracted 16 to 18% in length.[108] The cross-section of the bar stock could not be increased substantially due to the temperature gradient between the surface of the bars and the core of the bars.[108] The primary advantages for producing tungsten bar stock by direct sintering were shorter sintering times, higher purity bars, and relatively low maintenance costs relative to pressureless sintering.[18]

The direct sintering method and spark plasma sintering both rely on an electrical direct current to heat the tungsten parts; however, the two processes are distinctly different. In direct sintering, the tungsten parts are not constrained within uniaxial dies or subjected to external pressures, the atmosphere is hydrogen rather than a vacuum, and the current is not pulsed.[18,108]

2.6.4. Spark Plasma Sintering of Tungsten

Oxygen and other impurities along the grain boundaries of tungsten make the material brittle and easily susceptible to intergranular fracture.[18] Spark plasma sintering provides an apparent advantage over traditional sintering techniques as it provides a surface cleaning effect.[55] This effect in tungsten was first reported by Jones *et al.*[62] in 1994, when tungsten powders were consolidated by a 600 to 4000 A pulsed current at 25 V. X-ray diffraction was performed on the sintered compacts, and the researchers determined no tungsten oxides were present in the compact.[62] Removal of oxides from the tungsten powders was later shown using high resolution TEM on tungsten consolidated by spark plasma sintering.[55]

These early papers[55,62] also showed limited grain growth in spark plasma sintered tungsten. During this period, the Army Research Laboratory was interested in replacing uranium kinetic energy penetrators with a different metal or alloy.[61] Modeling of highly pure tungsten has been shown to greatly increase the strength and ductility of tungsten, making it an ideal candidate material for new kinetic energy penetrators.[61] For tungsten to have these desirable properties, the grain sizes must be reduced to the nanometer scale.[103,109] Traditional consolidation techniques, such as pressureless sintering and hot pressing, are too slow to maintain a small grain size,[103] and spark plasma sintering studies on tungsten have focused on high-pressure sintering at high heating rates (upwards of 1000 ºC/min).[110] Zhou *et al.* spark plasma sintered nanometer-sized tungsten with an applied pressure greater than 3 GPa to produce parts that are high density and have limited grain growth.[111] Zhou *et al.* reported that grain growth is inhibited and compacts with densities greater than 90% theoretical density were produced below 1200 ºC.[111]

In 2009, Kim *et al.* reported spark plasma sintering tungsten with up to 5 wt% yttria, hafnia, and lanthia to produce an oxide dispersion strengthened alloy.[77] In this study, all three oxides restricted tungsten grain growth.[77] The addition of yttria to tungsten produced near full density materials, but the addition of hafnia and lanthia did not produce materials of such high density.[77] The tungsten-yttria parts were analyzed by energy dispersive spectroscopy in a transmission electron microscope, and the yttria phase was found to contain tungsten.[77] The higher sintered density of the tungsten-yttria parts and the presence of tungsten in the yttria phase was attributed to a possible eutectic formation in the tungsten-yttrium-oxygen system.[77]

CHAPTER 3: EXPERIMENTAL PROCEDURES

This study was designed to determine the densification kinetics and grain growth kinetics during spark plasma sintering (SPS) of pure tungsten powders and tungsten-ceria powders, as well as to characterize the resulting tungsten and tungsten-ceria microstructures. The powders were prepared from commercially supplied tungsten and ceria powders, and were subsequently processed by spark plasma sintering and hot pressing techniques. Two separate experiments were performed on tungsten and tungsten-ceria powders.

In the first experiment, powder compositions were varied between 0 wt% ceria and 20 wt% ceria.[†] These powders were processed at two constant pressures of 42 MPa and 64 MPa, heated at 40 ºC/min to maximum temperatures of 1300 to 1700 ºC, and soaked at the maximum temperature between 0 and 4 minutes. In the second set of experiments, tungsten and W-10CeO_2 powders were processed at 64 MPa, heated at 100 ºC/min to temperatures between 800 and 1800 ºC, and soaked for 2 minutes. To compare the SPS process to more conventional sintering techniques, hot pressing was used to produce tungsten and W-4CeO_2. The hot pressed powders were held at a constant pressure of 42 MPa, heated at 30 ºC/min, and soaked for 30 minutes between 1300 and 1600 ºC.

[†] For the remainder of this thesis, the tungsten-ceria compositions will be written in a shorthand notation such that the weight percent of ceria will only appear as a number and the chemical formulas will be used. For example, tungsten with 10 wt% ceria will appear as W-10CeO_2.

The bulk density of the sintered compacts was determined by standard water displacement methods, and the tungsten grain size distribution of the compacts was determined by electron backscatter diffraction (EBSD). Backscatter electron (BSE) imaging coupled with digital image analysis was used to determine the 2-dimensional pore size distribution and the area concentration of tungsten and ceria. The oxidation state of the cerium ions in the W-15CeO_2 compacts was measured by x-ray photoelectron spectroscopy (XPS). Vickers microhardness testing was performed on all samples soaked for 2 minutes. A more complete description of the experimental methods employed in this study is contained in this chapter.

3.1. As-Received Tungsten and Ceria Powders

3.1.1. Tungsten Powder

Two lots, Lot C3-525 and Lot C3-533, of submicron tungsten powder (99.99% pure) were used in this study (Buffalo Tungsten Inc., Depew, NY, USA). According to the manufacturer, the C3-525 tungsten powder had an average particle size of 0.81 μm, and the C3-533 tungsten powder had an average particle size of 0.84 μm. Secondary electron imaging in a Hitachi S-4500 FESEM was used to confirm the size of the as-received powders and to determine the powder morphology.

Electron backscatter diffraction (EBSD) was used to determine the mean particle size and particle size distribution of the tungsten powder. To prepare the tungsten powder for EBSD, a sample of the powder was dispersed in a graphite-filled phenolic thermoset resin (KonductoMet®, Buehler, Lake Bluff, IL, USA) and hot mounted. The hot-mounted sample was then ground with 1200 grit silicon carbide abrasive paper,

polished with a 1 μm alumina suspension, and then polished with a 0.3 μm alumina suspension. Final polishing of the mounted sample was done in a vibratory polisher (Vibromet 2®, Buehler, Lake Bluff, IL, USA) containing a 0.05 μm alumina suspension, and the sample was polished for 24 h. The mounted powder was analyzed using EBSD mapping of a 10 μm × 10 μm area with a point resolution of 0.03 μm.

3.1.2. Ceria Powder

The cerium (IV) oxide powder used in this study was <25 nm particle size, and was supplied by Sigma-Aldrich Co. (Milwaukee, WI, USA). The as-received ceria powder (Lot 03118JJ) was reported by Sigma-Aldrich to have an equivalent spherical diameter of 13.8 nm, as determined by the Brunauer-Emmett-Teller method. The oxygen loss on ignition was reported to be 1.6% at 800 ºC for 1 h. No independent analysis of the ceria powder was performed in this study.

3.2. Hydrogen Reduction of Tungsten Powder

An initial concern in this study was the influence of oxygen on the sintering of tungsten. In many tungsten sintering studies,[61,95,99,101,102,105] the precursor powders were reduced in hydrogen prior to sintering. In industrial sintering of tungsten, dry hydrogen is used to remove impurities during densification.[18,108] For the first set of experiments, the as-received tungsten powders were treated with dry hydrogen to remove oxides on the particle surfaces.

The tungsten was loosely packed into high-purity alumina sintering dishes to a height of 4 mm (Figure 3.1). The powder height directly influences the diffusion rate of water removal from the powder, and the higher humidity near the bottom of the alumina

boat aids in the nucleation and growth of tungsten particles.[94] The alumina boats with the powder were loaded into a CM Furnace, Inc. (Bloomfield, NJ, USA) 1730-12 HT furnace equipped with a 50 mm diameter 99.8% alumina tube (CoorsTek, Golden, CO, USA). Stainless steel caps with rubber seals were placed on the ends of the alumina tube. A mixture of 6% H_2, balance N_2 certified gas (Praxair, Salt Lake City, UT, USA) was continuously flowed across the powders for the entirety of the reduction cycle. The exhaust gas was bubbled through water, and the flow rate was adjusted to create a constant bubbling during reduction. Tungsten nitrides do not form at the temperatures and pressures used during reduction,[18] and nitrogen was considered to be an inert gas. The furnace was heated at 4 ºC/min to 850 ºC and held at 850 ºC for 360 min. Upon completion of the soak, the furnace was cooled to room temperature at 4 ºC/min.

The soak temperature was selected to promote the reaction of hydrogen with the adsorbed oxygen, forming water vapor that was exhausted from the system by the flow gas, and creating an oxygen-free surface on the tungsten. The temperature was low enough to limit particle coarsening during reduction. The tungsten powders were then removed from the tube furnace and immediately placed in an argon-atmosphere Plas-Lab 870-CLC glove box (Lansing, MI, USA) to prevent oxygen from adsorbing to the tungsten surface.

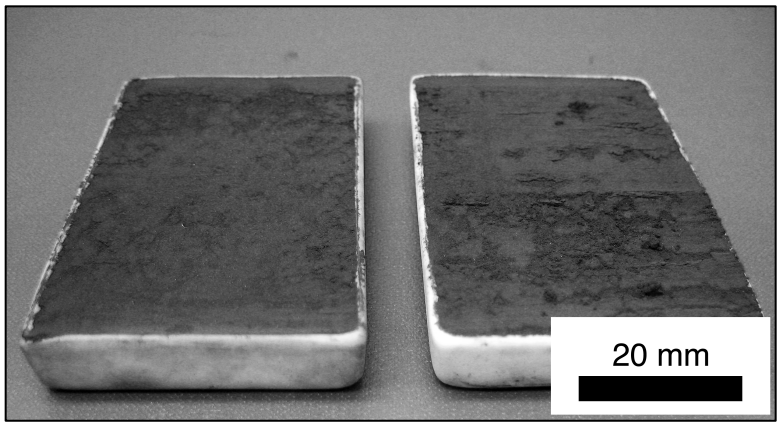

Figure 3.1. As-received tungsten loosely packed into high-purity alumina boats. The powder was leveled to the top of the alumina boats to give a bed height of 4 mm. This procedure was observed for all tungsten reduction cycles to ensure all batches maintained a similar particle size distribution.

3.3. Homogenization of Tungsten and Ceria Powders

3.3.1. Planetary Ball Milling of Powders

To homogenize the reduced tungsten and ceria powders, the powders were planetary ball milled. To ensure oxygen would not contaminate the powder samples, the powders were placed in a 250 ml ball-milling vessel with 2 mm yttria-stabilized zirconia spheres (Tosoh USA, Inc., Grove City, OH, USA) while in the argon-filled Plas-Lab 870-CLC glove box (Lansing, MI, USA). A consistent 1.4:1 ratio of powder-to-media (by mass) was used in each ball milling run; the maximum powder mass used in the ball milling runs was 250 g. The reduced tungsten powder was mixed with 1, 4, 10, 15, or 20 wt% ceria powder in the milling jar, and the jar was sealed in the argon-atmosphere glove box. In addition to milling the tungsten and ceria powders to homogenize them, the

reduced tungsten that was used in hot pressing and spark plasma sintering was also milled to ensure the pure tungsten powder had an identical process history to that of the tungsten-ceria composite powders.

For each milling run, the sealed milling vessel was removed from the glove box and placed in a PM 100 planetary ball mill (Retsch GmbH, Haan, Germany). The powders were milled at 300 rpm for 6 h, after which the sealed milling jar was removed to the argon-atmosphere glove box. The powders were extracted from the milling jar and the packed powders were broken apart by a mortar-and-pestle, and then divided into 6.0 to 8.0 g partitions and packaged separately in sealed plastic containers. Each powder sample was weighed to two significant figures on a scale contained within the glove box. The powders were partitioned such that each sample would be approximately 0.42 ml in volume, assuming full density. The sealed plastic containers were transferred to a sealed metal container and shipped to Idaho National Laboratory or the Center for Advanced Energy Studies in Idaho Falls, ID to be spark plasma sintered.

3.3.2. Suspension Mixing of Powders

In the second set of experiments, the tungsten powders did not undergo the hydrogen reduction process outlined in Section 3.2, and instead of homogenizing the tungsten and ceria powders by ball milling, the powders were mixed in cyclohexane. Cyclohexane was chosen as the mixing solution as it would not oxidize or reduce the tungsten and ceria powders. The powder composition W-10CeO_2 was studied, and 24.75 g of ceria was mixed with 222.75 g of tungsten. The powders were placed in a 1000 ml beaker and 600 ml of cyclohexane was added to the powders. A magnetic stir bar was placed in the bottom of the beaker, and the mixture was stirred at 360 rpm at 70 ºC. After

1 h of mixing, the stir speed was reduced to 300 rpm and the temperature was increased to 85 ºC to promote the evaporation of the cyclohexane. The beaker was held at 85 ºC until the powder was dried, and the composite powder was separated into 6.9 g lots (the same mass used in the W-10CeO_2 powders that were reduced-and-milled). Each lot was individually packed in a plastic container, and the containers were shipped to the Center for Advanced Energy Studies in Idaho Falls, ID.

3.4. Graphite Dies

The dies used for hot pressing and spark plasma sintering were constructed from pure graphite rods, grade AXF-5Q (POCO Graphite Inc., Decatur, TX, USA). Each die body had an outer diameter of 44.5 mm, an inner diameter of 12.7 mm, and a height of 30 mm. A hole was drilled along the radius of the die body at the center of the curved surface. This hole was 1.6 mm in diameter, and extended 11.1 mm into the die body. The purpose of this hole was to produce a blackbody cavity to measure the die temperature by an infrared thermometer; however, the outer diameter and inner diameter of the die limited the cavity size to a 1:7 ratio. The validity of this hole as a blackbody cavity is discussed in Section 4.2. The die punches were also manufactured from AXF-5Q graphite, and measured 12 mm in diameter and 20 mm in length (Figure 3.2). Three dies were manufactured with two blackbody cavities, each with a 1.6 mm diameter and 11.1 mm deep, and set 90º from each other on the curved surface.

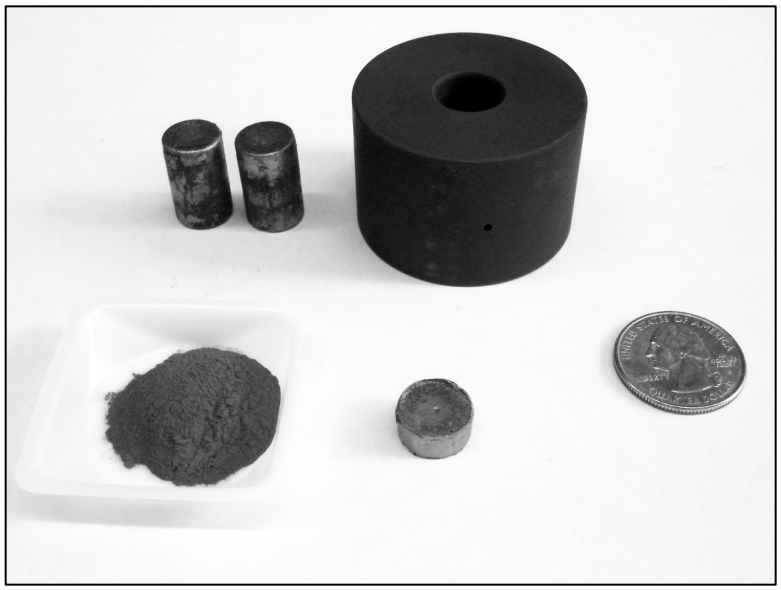

Figure 3.2. Graphite punches, graphite die, quarter for scale, consolidated tungsten pellet, and tungsten powder. The die and punch sizes were constant throughout the SPS and HP experiments. The mass of powder varied between 6.0 and 8.0 g, depending on the powder composition.

Prior to pouring the powder into the die, the interior of the die was lined with a layer of 0.37 mm high-purity graphite foil (Union Carbide). A single 12 mm diameter 0.37 mm-thick high-purity graphite foil disk was placed on the end of one of the punches, and the punch was inserted into the die lined with graphite foil. The pre-portioned powder was poured into the die assembly, and distributed uniformly in the die by a metal spatula. A 12 mm diameter graphite disk was placed on top of the powder, and the second graphite punch was inserted into the die. The assembly was pressed by hand to ensure the powder was fully secured within the die.

To prevent excessive heat loss through the die during spark plasma sintering, the graphite dies were insulated by 4-mm-thick high purity graphite felt (Fiber Materials, Inc., Biddeford, ME, USA). The felt was wrapped around the die body and secured using

carbon fiber string (Structure Probe, Inc., West Chester, PA, USA). A square of felt surrounding the blackbody cavity was cut away to allow the blackbody cavity to be visible to the infrared thermometer. Circles of felt were cut to cover the top and bottom of the die body, and 12 mm holes were made in the center to accommodate the punches.

3.5. Spark Plasma Sintering of Tungsten and Tungsten-Ceria Powders

3.5.1. Preparation for SPS

A Dr. Sinter Lab SPS-515S (SPS Syntex Inc., Kanagawa, Japan) was used to produce the spark plasma sintered samples. The SPS unit is owned by Boise State University, and is located at the Center for Advanced Energy Studies in Idaho Falls, ID (Figure 3.3). The process chamber contains upper and lower water-cooled stainless steel electrodes. Prior to placing the die assembly into the chamber, graphite spacers were placed on the bottom electrode. The graphite spacer in contact with the electrode was a cylinder 152.4 mm in diameter and 25.4 mm in height. A second cylindrical spacer measuring 38.1 mm in diameter and 25.4 mm in height was centered on the first spacer. The die assembly was centered on the second spacer, and the blackbody cavity was directed toward the infrared thermometer. Two cylindrical spacers were applied to the top of the die assembly, and had the same dimensions as the bottom spacers (Figure 3.4).

Figure 3.3. Dr. Sinter Lab SPS-515S spark plasma sintering unit located at the Center for Advanced Energy Studies. The infrared thermometer and sintering chamber are located on the left; the temperature controller, atmosphere control, and direct current generator are located in the middle unit; the data acquisition and pressure controls are located on the right unit.

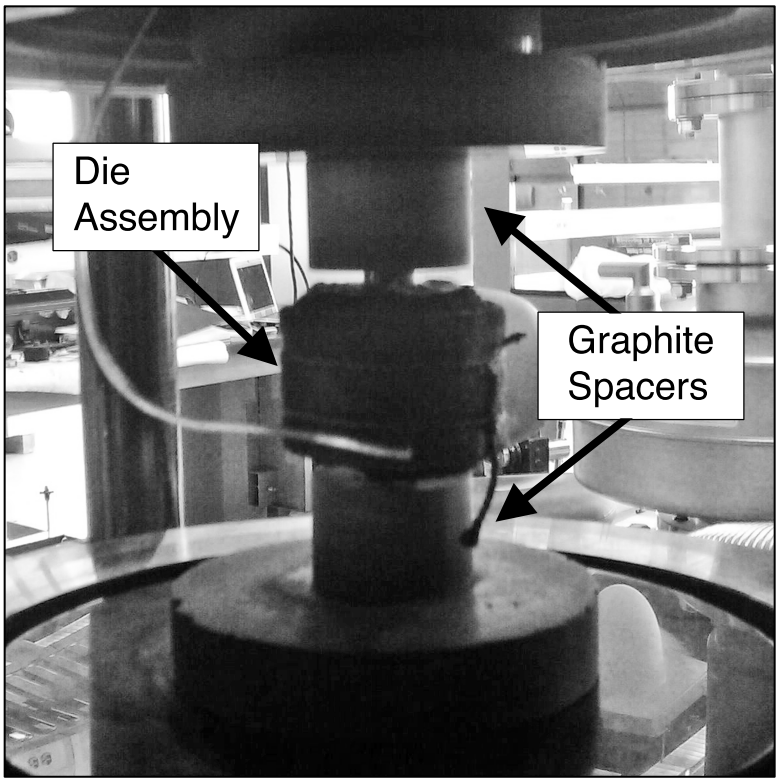

Figure 3.4. Die assembly in SPS unit. Graphite spacers were placed between the hydraulic rams and the die assembly to center the die in the SPS chamber. The die was wrapped with graphite felt secured with carbon fiber string. The die was rotated to align the blackbody cavity with the infrared thermometer (not visible).

An IR-AHS infrared thermometer (Chino Corporation, Tokyo, Japan) was optically aligned with the blackbody cavity by the aid of a viewfinder. The lens was manually adjusted until the surface of the blackbody cavity was in focus (Figure 3.5). The IR-AHS infrared thermometer was capable of measuring temperatures between 600 and 1500 ºC with an accuracy of ±0.5% of the measured temperature, and between 1500 to 2000 ºC with an accuracy of ±1.0% of the actual temperature, according to the manufacturer.[112] The infrared thermometer was not calibrated prior to spark plasma

sintering, and a discussion of the temperature measurement is contained in Section 4.2 of this thesis. For the experiments in which the temperature was recorded by two independent methods, the infrared thermometer was aligned with one of the blackbody cavities, and a type-K thermocouple (Omega Engineering Inc., Stamford, CT, USA) was inserted fully into the second blackbody cavity. A Cole Parmer Digi-Sense temperature controller recorded the thermocouple output and corresponding temperature at a temporal resolution of 1 Hz.

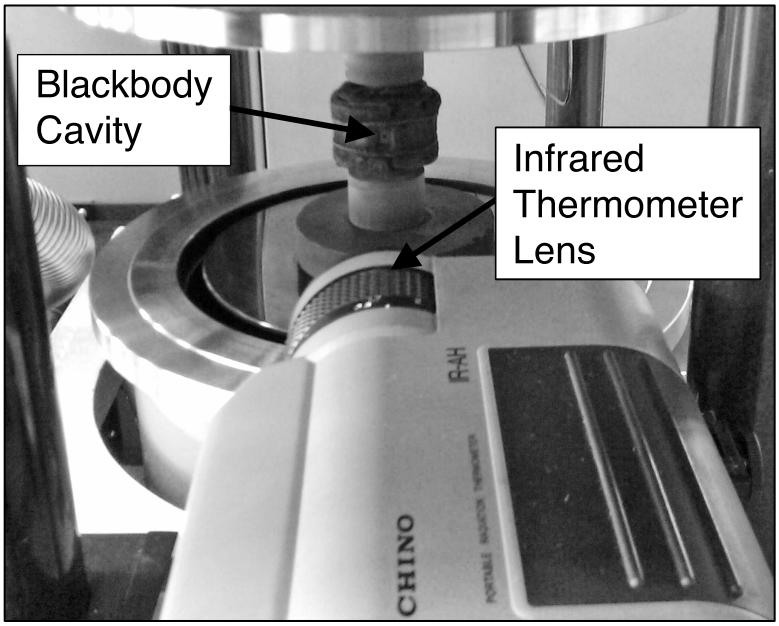

Figure 3.5. Alignment of the blackbody cavity of the die and the optical pyrometer prior to SPS. Due to die displacement, the pyrometer was adjusted during the sintering cycle to maintain alignment with the blackbody cavity.

The SPS chamber was sealed and evacuated to approximately 1 Pa by a mechanical pump once the infrared thermometer was aligned with the die blackbody. The chamber was then purged with argon to laboratory air pressure, and evacuated by the

mechanical pump again. This process was repeated three times to rid the chamber of oxygen and other reactive gases, and the mechanical pump was operated for the duration of each SPS cycle.

Two independent Chino KP1000 programmable controllers (Chino Corporation, Tokyo, Japan) were used to set the temperature and pressure profiles. During spark plasma sintering, the temperature controller adjusted the current to raise or lower the temperature to the programmed temperature. The pressure controller maintained the programmed pressure by adjusting the hydraulic ram. The direct current was pulsed during sintering, and the factory default setting 12:2 was used for all experiments. According to the manufacturer, this pulse pattern produces a cycle of 12 ms of current, and 2 ms of no current. The temperature, voltage, current, and hydraulic ram displacement during spark plasma sintering were recorded by LabView® v8.2 (National Instruments Corp., Austin, TX, USA).

3.5.2. SPS Processing Profiles

Two different sintering profiles were used to consolidate the tungsten and tungsten-ceria powders in this study. In the first profile, the reduced-and-milled powders (pure W, W-1CeO_2, W-4CeO_2, W-10CeO_2, W-15CeO_2, and W-20CeO_2) were heated at 40 ºC/min to between 1300 and 1700 ºC, and the samples were soaked at maximum temperature for 0, 2, or 4 min. The applied pressure on the samples was constant at 42 or 64 MPa for each of these experiments. The second sintering profile was used to consolidate the as-received tungsten powder and W-10CeO_2 mixed in cyclohexane. The powders were pressed with a constant 64 MPa, heated at 100 ºC/min to maximum temperatures between 800 and 1800 ºC, and soaked at maximum temperature for 2 min.

In addition to these experiments, the as-received tungsten and W-10CeO_2 were processed at 64 MPa at 900, 1200, 1500, and 1800 ºC for soaks between 2 min and 26 min.

In the first sintering profile, the SPS was heated to 620 ºC in 3 minutes. This was done to ensure the infrared thermometer was providing feedback to the controller (the minimum temperature measurable by the infrared thermometer was 570 ºC). After the first 3 minutes had elapsed, the controller was programmed to raise the temperature at 40 ºC/min to a maximum temperature of 1300, 1400, 1500, 1600, or 1700 ºC. For samples with no soak times, the current was shut off at the programmed time, regardless of the measured temperature. For the samples soaked for 2 min or 4 min, the current was shut off at the end of the soak. Two constant applied pressures were investigated with these samples, 42 MPa and 64 MPa (Table 3.1). For samples sintered with an applied pressure of 42 MPa, the SPS minimum pressure was maintained automatically without the use of the pressure controller. For the samples sintered with an applied pressure of 64 MPa, the pressure controller was programmed to raise the pressure from 42 to 64 MPa during the first minute of sintering, and was maintained at 64 MPa for the duration of the sintering cycle. Some of the sintering profiles were repeated on multiple samples to ensure the reproducibility of the SPS process (Table 3.1).

Table 3.1. Processing parameters and number of samples produced for spark plasma sintering of reduced-and-milled powders. The number for each process parameter indicates the number samples produced.

Powder Composition	Pressure (MPa)	Soak Time (min)	Temperature (ºC)				
			1300	1400	1500	1600	1700
Pure W	42	0	2		1		2
	42	2	2	2	2	2	2
	42	4	1		2		1
	64	0	1	1		1	1
	64	2	2	2	2	2	2
	64	4	1		1		1
W-1CeO_2	42	0	1		1		1
	42	2	1	1	1	1	1
	42	4	1		1		1
	64	2	1	1	1	1	1
W-4CeO_2	42	2	1	1	1	1	1
	64	2	1	1	1	1	1
W-10CeO_2	42	2	1	1	1	1	1
	64	2	1	1	1	1	1
W-15CeO_2	42	2	1	1	1	1	1
	64	2	1	1	1	1	1
W-20CeO_2	42	2	1	1	1	1	1
	64	2	1	1	1	1	1

Based on analysis of the temperature and current curves of the reduced-and-milled experiments and the constant heating rate experiments, the sintering profiles were adjusted for the as-received powders and mixed powders. The die was heated to 600 ºC in 5 min and held for 4 min to ensure the current and temperature were in equilibrium prior to sintering the powders. During the initial heating, the applied pressure was raised to 64 MPa in the first minute and held constant during the sintering and cooling cycle. To study the consolidation as a function of temperature, the tungsten powders were heated at 100 ºC/min to maximum temperatures between 800 and 1800 ºC, in 100 ºC increments, and soaked for 2 min. The W-10CeO_2 samples were sintered between 800 and 1600 ºC,

in 100 ºC increments, and soaked for 2 min. The as-received tungsten and W-10CeO_2 powders were also spark plasma sintered at 900, 1200, 1500, or 1800 ºC for 5, 8, 14, 20, and 26 min to study the effects of dwell time on the sintering kinetics. A summary of the samples produced from the as-received and mixed powders is given in Table 3.2.

Table 3.2. Processing parameters and number of samples produced for spark plasma sintering of the as-received tungsten powders and as-received tungsten with 10 wt% ceria. The sintering pressure was constant at 64 MPa. The number for each process parameter indicates the number of samples produced.

Powder Composition	Soak Time (min)	Temperature (10^{-2} ºC)										
		8	9	10	11	12	13	14	15	16	17	18
Pure W	2	2	3	2	2	3	3	2	2	2	2	3
	5		2			2			2			2
	8		2			1			1			2
	14		1			2			2			2
	20		1			1			1			2
	26		1			2			2			2
W-10CeO_2	2	2	2	1	1	2	2	1	1	2		
	5		2			1			2			
	8		1			1			1			
	14		2			2			2			
	20		1			1			1			

3.6. Hot Pressing of Tungsten and Tungsten-Ceria Powders

Hot pressing was performed on reduced-and milled tungsten and reduced-and-milled W-4CeO_2. The powders were packed in 8.0 g and 7.8 g lots of pure tungsten and W-4CeO_2, respectively, in the same manner discussed in Section 3.3.1. The powders were then shipped to Colorado School of Mines, Golden, CO to be hot pressed.

A graphite-interior programmable vacuum hot press (Astro Division, Thermal Technologies Inc., Santa Barbara, CA, USA) equipped with two type-C thermocouples (Omega Engineering, Stamford, CT, USA) was used to sinter the reduced-and-milled powders (Figure 3.6). The same die set used in spark plasma sintering was used for hot pressing, however the dies were not wrapped in graphite felt in these experiments. A uniaxial load was applied and a constant 42 MPa was maintained on the punches during sintering. The hot press chamber was evacuated by a mechanical pump and purged with argon; this process was repeated three times prior to sintering. The atmosphere was maintained at about 1 Pa during hot pressing by the mechanical pump. All samples were heated at 30 ºC/min and soaked at the maximum temperature for 30 min. The samples were processed at 1300, 1400, 1500, and 1600 ºC. At the end of the 30 min soak, the heating elements were shut off, and the samples were cooled in vacuum to room temperature before being removed from the hot press. During sintering, the temperature, pressure, and displacement were recorded at 1 Hz by a digital acquisition system.

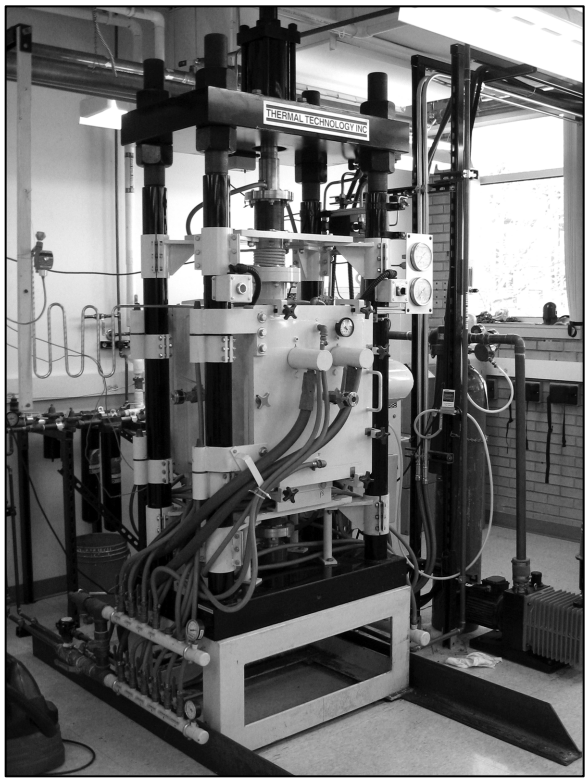

Figure 3.6. Thermal Technologies Inc. hot press located at Colorado School of Mines. Pure tungsten and W-4CeO_2 powders were hot pressed between 1300 and 1600 ºC with an applied pressure of 42 MPa.

3.7. Bulk Density Measurement of Sintered Samples

3.7.1. Preparation for Bulk Density Measurement

During sintering, the tungsten bonded to the graphite foil, and prior to density measurements being performed, the carbide layer had to be removed. For the parts produced from the reduced-and-milled powders, the parts were sectioned in half along the diameter, and the carbide layer was only removed from one half of each specimen. For the parts produced from the as-received powder and mixed powder, the carbide layer was removed from the entire specimen. Grinding discs embedded with 74 µm diamonds

were used to remove the carbide layer on all samples. The samples were ground until the carbide layer (dull grey) was no longer visually observed on the specimens.

3.7.2. Density Measurement by ASTM B311-93

The density of the first set of SPS samples and the hot pressed samples was determined by the water displacement method described in ASTM B311-93.[113] An AB-54-S/FACT digital analytical scale (Mettler Toledo Inc., Columbus, OH, USA) with a density measurement kit were used to for the density measurements. The water temperature was measured with a Hediger AG Ch-8706 alcohol thermometer graduated in 0.2 ºC increments. Each sample mass was measured in air three times, and the suspended mass was measured three times. During the suspension measurements, the water temperature was also recorded. Between suspended measurements, the parts were dried with compressed air.

3.7.3. Density Measurement by ASTM B962-08

The water displacement method used to measure the sample densities in the first set of experiments was found to have large errors due to water infiltrating the pores of the specimens. An alternative water displacement method for determining density, ASTM B962-08,[114] was used for the second set of experiments to reduce the errors caused by the specimen pores being infiltrated with water. A discussion of the error of the water displacement techniques is contained in Section 4.3.1. The same scale and density measurement kit used to find the densities by ASTM B311-93 were used to measure the density of the second set of samples.

The dry mass of each sample was measured in air three times. The samples were then placed in deionized water, and placed in a vacuum chamber for 24 h. The purpose

of this step was to infiltrate the surface-connected pores so that no gain in mass would be observed when the suspension measurements were taken. The water-impregnated samples were then removed from the water and the surface was dabbed with a lint-free cloth to remove any surface moisture. The mass of the impregnated samples was then measured in air three times, and the samples were placed back in the deionized water. The suspended mass or each specimen was then measured three times, and the water temperature was recorded.

3.8. Sample Preparation for Grain Size, Porosity, and Hardness Testing

3.8.1. Sectioning and Mounting of Samples

The SPS samples produced from the reduced-and-milled powders and the hot pressed samples were sectioned on a TechCut 4 low speed saw with a high concentration diamond blade (Allied High Tech Products Inc., Rancho Dominguez, CA, USA). The samples were first cut along the diameter of the part, and one of the halves was used for bulk density determination, and the other half was sectioned again along the radius of the part. One of the quarters was hot mounted for use in this study, and the other quarter was set aside for future studies. The samples were mounted in Bakelite thermosetting powder (Leco Corp., St. Joseph, MI, USA).

For the SPS samples produced from the as-received and mixed powders, the samples were secured in a vise and fractured along the diameter with a diamond-tipped chisel. One half was ground flat on the interior surface and hot mounted, and the other half was preserved with the fracture surface for future studies. The samples were

mounted in an electrically conductive graphite-filled thermoset plastic (KonductoMet, Buehler, Lake Bluff, IL, USA).

3.8.2. Preparation of Metallographic Samples

Coarse grinding of the mounted specimens was performed using diamond-embedded grinding discs, and grinding sequentially from 74 μm diamond to 40 μm diamond to 10 μm diamond. Fine grinding was performed using 800 grit and 1200 grit silicon carbide paper. Polishing was performed using 0.3 μm alumina on a nylon felt nap, and final polishing was performed by placing the samples in a vibratory polisher (Vibromet 2, Buehler, Lake Bluff, IL, USA) for 6 h. A 0.05 μm alumina suspension was used during vibratory polishing.

Murakami's reagent (10 ml water, 1 g potassium ferricyanide, 1 g sodium hydroxide) was applied with a cotton-tipped swab to the polished tungsten between 5 and 15 s to produce grain boundary relief.[115] The etchant was washed from the surface with deionized water, followed by an ethanol wash, and then dried with compressed air. To slow the rate of surface oxidation, the samples were stored in a vacuum desiccator.

3.9. Grain Size Measurement by Electron Backscatter Diffraction

A Leo 1430VP scanning electron microscope equipped with an EDAX/TSL Digiview III electron backscatter detector (Ametek Inc., Mahwah, NJ, USA) was used to measure the grain size. Copper tape was adhered to the samples mounted in Bakelite to provide a conductive path, but was unnecessary for the samples mounted in the graphite-filled resin. The samples were placed in the SEM and tilted such that the surface of the sample was 70º relative to the beam direction. The accelerating potential of the electron

beam was set to 25 kV. The EDAX/TSL Digiview III captured the electron backscatter diffraction patterns, and the TSL OIM™ Data Collection 5 software (Ametek Inc., Mahwah, NJ, USA) collected the pattern data.

The TSL OIM™ Data Collection 5 software was used to measure the grain size of the tungsten by an automated lineal intercept method. A random spot near the center of each sample was located and the microscope magnification was set to 1000x. A 10 × 10 grid was imposed over the visible SEM image (approximately 310 μm × 320 μm) to give a total line length of approximately 6.3 mm, and the step size was set to 0.1 μm. This process was repeated for two more randomly selected spots near the sample middle. After all data were collected, the three data sets containing the measured grain sizes were combined; in all combined data sets, at least 1000 grains were measured. The combined grain size data were exported and analyzed using Mathematica.[116]

The automated lineal intercept method uses an algorithm whereby the phase is first identified (only tungsten grains for this study), and the misorientation between two data points is measured. If the misorientation is less than 5º, the software recognizes the two points as belonging to the same grain. If the misorientation is great than 5º between neighboring points, the software expands the neighborhood to include more points to determine whether the data point was correctly identified. If the neighborhood has a misorientation of 5º or greater, a new grain is added to the data set. For the samples containing ceria, the cerium dioxide phase was not identified, and the software effectively ignored the phase.

3.10. Vickers Microhardness Indenting of Tungsten and Tungsten-Ceria Samples

Hardness testing was performed on all samples soaked for 2 min from the first set of spark plasma sintered parts, all hot pressed samples, and all samples produced in the second set of experiments. Before hardness testing was performed, the samples were hand polished with 0.3 μm alumina to reduce the visibility of grain boundaries and to remove the oxide layer on the samples. A DM-400F microhardness indenter (Leco Corp., St. Joseph, MI, USA) was used to make all indents and to optically measure the size of the indents. The procedure given by ASTM E384-09 was followed to perform the indentations and measurements.[117] The indents were spaced 1 mm apart, and 6 indents were made on each sample; all indentations were made with 1 kgf applied for 15 s. Both diagonals of each indent were measured optically.

3.11. Backscatter Electron Imaging

Backscatter electron imaging of the pure tungsten samples produced from the as-received powder was done in a Leo 1430VP SEM. The surfaces were polished again to remove the grain boundary grooves from the etchant prior to imaging. Images were taken for all samples processed between 800 ºC and 1700 ºC with a 2 min soak. Each sample was imaged at 1000x magnification. These images were analyzed using Mathematica[116] to determine the pore area fraction and the pore size distribution of each sample.

Backscatter electron imaging was also performed on the tungsten-ceria samples. Spark plasma sintered W-4CeO_2, W-10CeO_2, W-15CeO_2, and W-20CeO_2 and hot pressed W-4CeO_2 were imaged using a Hitachi S-4500 FESEM. The images were taken

with high-contrast settings to easily distinguish between the tungsten phase, the ceria phase, and the pores. The images were then analyzed to determine the area fractions of tungsten, ceria, and pores in each sample.

3.12. Cerium Oxidation State by X-ray Photoelectron Spectroscopy

X-ray photoelectron spectroscopy (XPS) was performed on all of the W-15CeO_2 samples. The objective of doing XPS was to determine the oxidation state of the cerium ion to indicate whether or not the ceria released oxygen during the sintering process. The 3d peaks of Ce (IV) (which are present in stoichiometic CeO_2) and Ce (III) (which are present in Ce_2O_3) were used in this comparison. The spectrometer used was a Physical Electronics Versaprobe located in the Physics department at Boise State University. The samples were irradiated with an Al-Kα x-ray beam approximately 100 μm in diameter at 25 W. To prevent the ceria grains from charging during data collection, a 10 eV electron beam and a 10 eV Ar^+ beam were focused on the sample surface. A 2 mm × 2 mm area near the center of the sample was sputtered with 4 kV Ar^+ for 30 s to reveal a virgin surface. Spectra for the cerium 3d transition were collected with an energy resolution of 23.5 eV. The binding energy scale was calibrated with 99.9% pure copper and aluminum foils.

CHAPTER 4: RESULTS AND DISCUSSION

The results of the experiments outlined in the previous chapter are presented in this chapter. The initial tungsten powders, and the hydrogen-reduced and ball-milled tungsten and tungsten-ceria powders, were characterized using secondary electron imaging and electron backscatter diffraction. The accuracy of temperature measurement during SPS is discussed, and methods to refine the temperature measurement are proposed.

The microstructures of SPS tungsten and tungsten-ceria are presented and discussed. The final densities, grain sizes, and hardnesses of spark plasma sintered tungsten and tungsten-ceria compacts are compared as functions of sintering temperature, isothermal dwell time, applied pressure, and ceria content. The final densities, grain sizes, and hardnesses are also compared to one another. Tungsten and W-4CeO_2 were hot pressed and are compared with samples produced by spark plasma sintering. The results of spark plasma sintered and hot pressed tungsten are also compared to published studies of tungsten processed by spark plasma sintering, hot pressing, and pressureless sintering (when available). A complete summary of all densities, grain sizes, and hardness results is given in the appendix.

In spark plasma sintered tungsten-ceria, the resulting compacts had evidence of ceria loss in the microstructure. Backscatter electron images of the tungsten-ceria parts were analyzed to determine the ceria content of each sample. At sintering temperatures

above 1500 ºC, the loss of ceria became more significant; this apparent ceria loss is discussed. The thermodynamics of the cerium-tungsten-oxygen system is discussed, as well as the possible reactions within the tungsten-ceria system that might lead to the loss of ceria.

In the last two sections of this chapter, the densification kinetics and grain growth kinetics of SPS tungsten are discussed. The diffusion coefficients, diffusion pre-exponentials, activation energies for densification were found using nonisothermal sintering models. The grain growth kinetics of SPS tungsten were determined using the isothermal grain growth law. The potential mechanisms of densification and grain growth are discussed, and the kinetics results are compared to studies in the literature. The validity of using traditional sintering models to determine the sintering kinetics of spark plasma sintered tungsten is also discussed.

4.1. Powder Characterization

4.1.1. As-Received Tungsten Powders

Based on visual analysis of secondary electron images of the as-received tungsten powder, the powder is composed of single crystals and does not contain large tungsten agglomerations (Figure 4.1). Electron backscatter diffraction (EBSD) was used to determine the particle size distribution of the tungsten powder, and a total of 1323 crystallites were measured using the lineal intercept method (Figure 4.2).

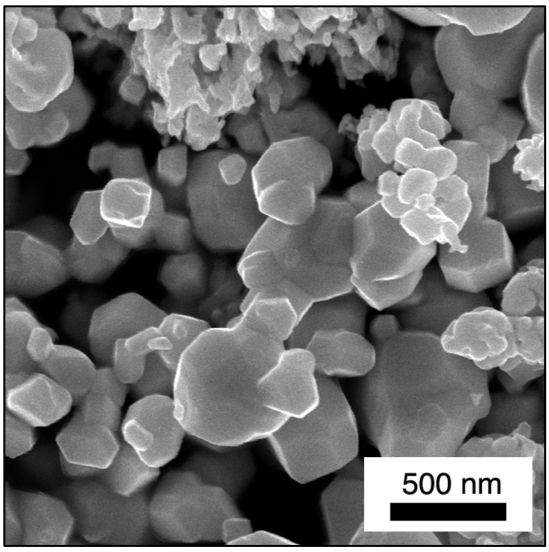

Figure 4.1. Secondary electron image of the as-received tungsten powder. The faceted edges and smooth faces indicate the tungsten powder is monocrystalline.

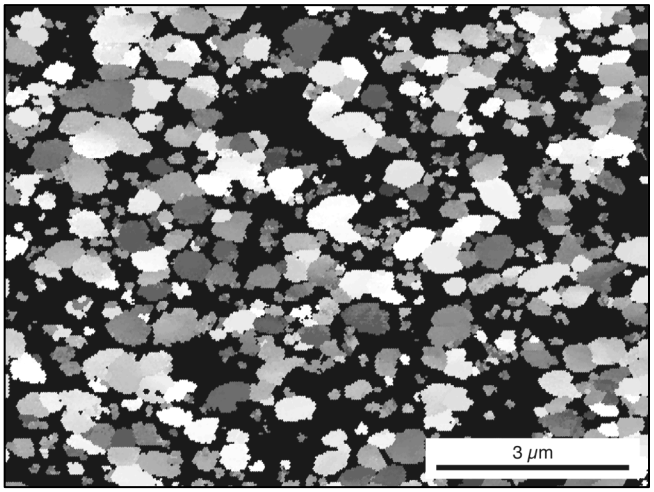

Figure 4.2. Inverse pole figure map showing the particle size and morphology of the as-received tungsten powder. The map was produced from EBSD data, and the shaded regions (all areas not in black) are representative of the tungsten crystallites. The resolution of each hexagonal pixel is 0.01 μm.

The crystallite size measurements acquired by EBSD were binned logarithmically and fit to the lognormal probability distribution (Figure 4.3). The particle size distribution fits the lognormal probability distribution well, which is common for small particle sizes.[118] The average of the particle intercepts was 0.26 μm, and using confidence intervals on the lognormal distribution by the Cox method,[119] the average crystallite size is between 0.25 and 0.27 μm within a 99% confidence interval.

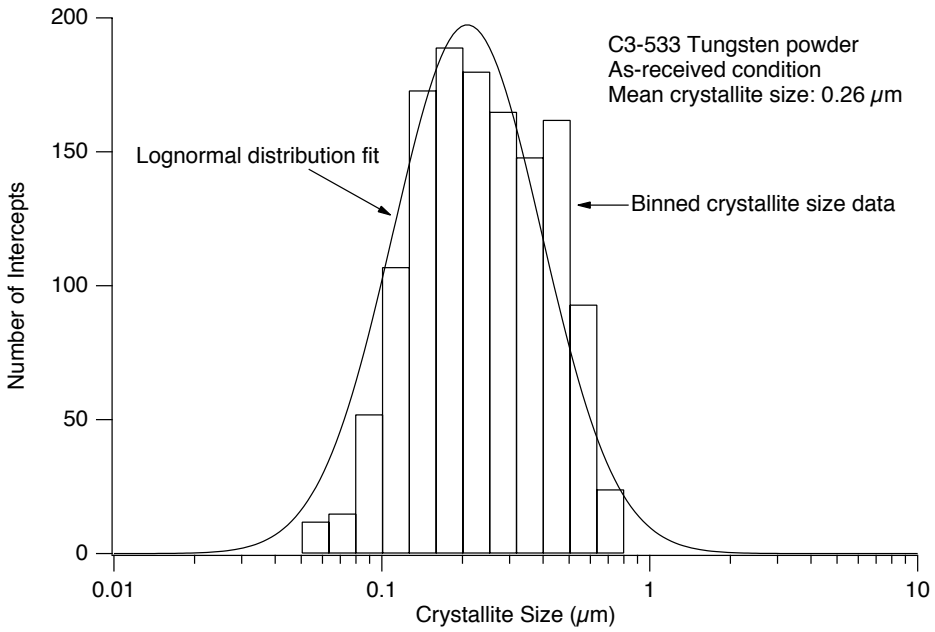

Figure 4.3. Crystallite size distribution in the tungsten powder obtained from 1323 intercepts measured using EBSD. The data were binned logrithmically and fit to the lognormal probability distribution. At a 99% confidence level, the mean crystallite size is between 0.25 and 0.27 μm.

4.1.2. Post-Reduction and Ball-Milled Composite Powders

During the hydrogen reduction of the tungsten powders, structures similar in shape and size to $WO_{2.9}$ were formed (Figure 4.4).[94] This conclusion was reached based on comparison of the image in Figure 4.4 with the SEM images of reduced tungsten

powders published by Schubert.[94] Pure tungsten can retain the structure of the precursor $WO_{2.9}$, and based on the presence of these structures in the final reduced tungsten, the most likely reaction scheme during reduction was WO_3 to $WO_{2.9}$ to β-W to α-W (Figure 4.5).[94] This reduction path is the most likely for this experiment since dry hydrogen was used, and moisture is necessary for $WO_{2.72}$ or WO_2 to form.[94]

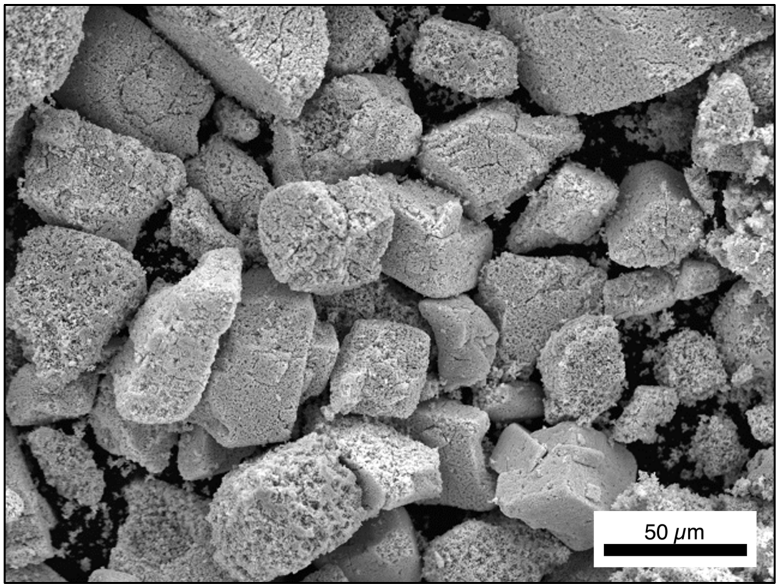

Figure 4.4. Secondary electron image of pure tungsten structures likely formed during the hydrogen reduction of $WO_{2.9}$ to W.

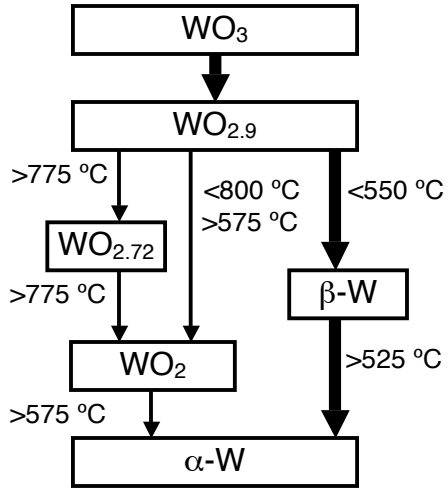

Figure 4.5. Reduction schemes for tungsten reduction. In this study, the tungsten reduction likely followed the path shown in bold arrows. This is based on comparing the image in Figure 4.4 to the literature. Figure reproduced from Schubert.[94]

The tungsten structures shown in Figure 4.4 were refined into individual crystallites by ball milling the tungsten powder. After milling, the structures in Figure 4.4 were no longer present, based on secondary electron images of the milled powder (Figure 4.6). The well-defined facets and smooth faces present in the as-received tungsten powder could no longer be observed in the ball-milled tungsten powder. The absence of these facets and smooth faces may indicate surface deformation of the powder surfaces. If the powder was deformed by ball milling, the concentration of dislocations on the surfaces of the particles may have been greater than that of the as-received powders.[37] A higher density of dislocations on the powder surfaces may have led to faster initial stage sintering[25]; however, the spark plasma sintering data collected during sintering of ball-milled tungsten and as-received tungsten cannot substantiate this

hypothesis. Future studies using highly sensitive equipment to measure the initial stage shrinkage may be used to ascertain whether or not the initial stage sintering rate is affected by ball-milling of tungsten and ceria powders.

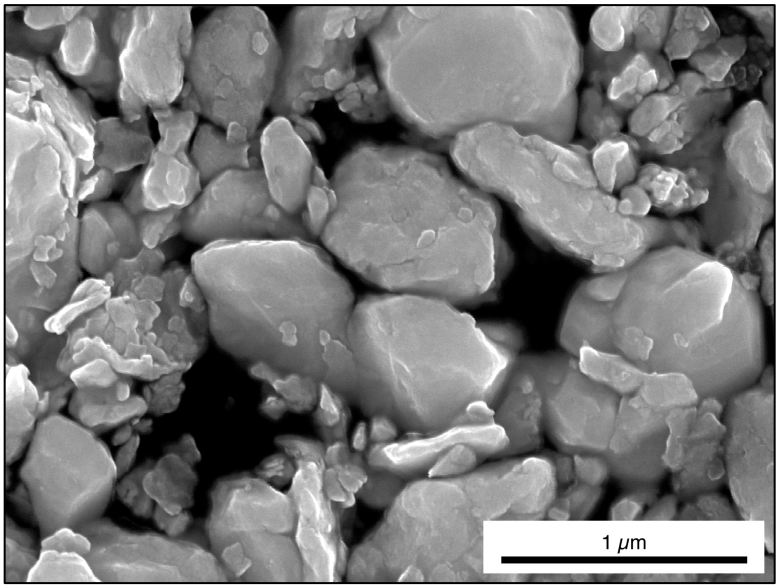

Figure 4.6. Secondary electron image of pure tungsten powder after hydrogen reduction and ball milling. The large tungsten agglomerations formed during the hydrogen reduction are no longer present, and the crystallite faces are not as well defined as the as-received tungsten powder.

4.2. Temperature Measurement in SPS

One of the primary sources of error in measuring the temperature during SPS was the unknown emissivity of the blackbody cavity. The graphite dies used in this study were designed with a 1:7 diameter-to-depth cavity, and it was uncertain if an emissivity of one (perfect blackbody) was a valid assumption. The emissivity of an object can be determined by simultaneous measurement of the wavelengths of light emitted from the

object and the actual temperature of the object.[120] To estimate the emissivity of the blackbody cavity, the infrared thermometer recorded the apparent temperature of the cavity, and simultaneously a type-K thermocouple measured the actual temperature of the die. The type-K thermocouple was inserted into a second 1:7 diameter-to-depth cavity in the die. The infrared thermometer and a thermocouple were used simultaneously in three spark plasma sintering runs of pure tungsten heated at 100 ºC/min from 630 to 1200 ºC (as recorded by the infrared thermometer). The 630 ºC lower limit was used due to the lower temperature limit of the infrared thermometer.[112] The 1200 ºC upper limit was used since the maximum working temperature of the type-K thermocouple is 1250 ºC.[121] The results of the temperature measured by the thermocouple and the temperature measured by the infrared thermometer are given in Figure 4.7.

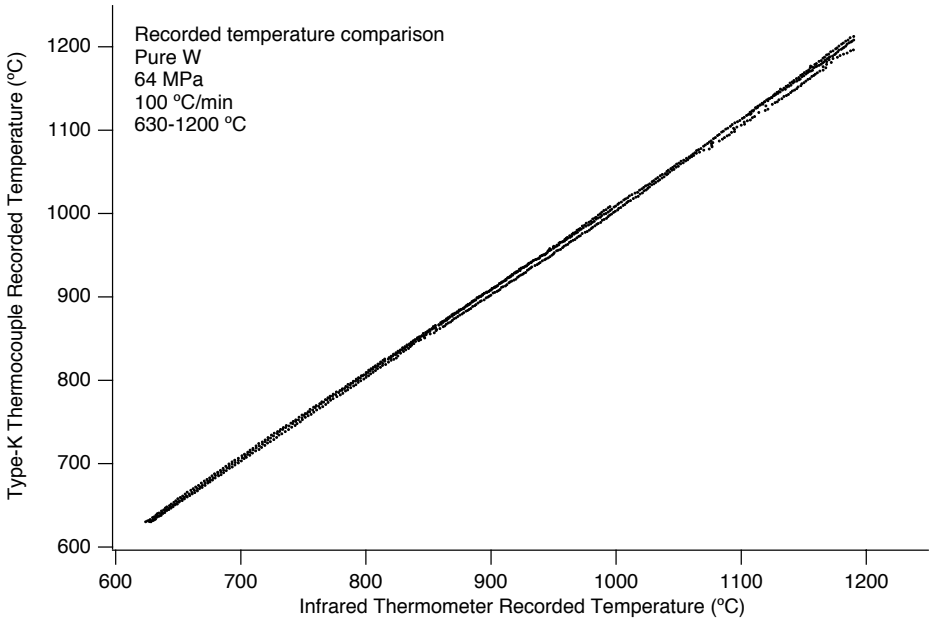

Figure 4.7. Comparison of the temperature measured by a type-K thermocouple and by an infrared thermometer in spark plasma sintering. The data were acquired from three spark plasma sintering cycles with heating rates of 100 ºC/min. The data from the three cycles is virtually identical and the three data sets cannot be easily distinguished from one another.

The data from the thermocouple and infrared thermometer were then used to estimate the emissivity of the die during sintering. To calculate the emissivity of the die, the following equation was used:

$$\varepsilon = \frac{T_{meas}^4}{T_{actu}^4} \qquad 4.1$$

where ε is the emissivity, T_{meas} is the measured temperature, and T_{actu} is the real temperature of the material.[120] The temperature recorded by the infrared thermometer was substituted for T_{meas}, and the temperature recorded by the type-K thermocouple was

substituted for T_{actu}. Using Equation 4.1, the emissivity of the blackbody was estimated using the 906 data points collected in the three spark plasma sintering runs where the temperature was recorded by the thermocouple and the infrared thermometer. The average emissivity was found to be 0.97, with a normal standard error of 0.01.

Because the infrared thermometer was set to a value of one for the emissivity, and the emissivity of the dies was found to be 0.97, the temperatures recorded by the infrared thermometer had to be adjusted accordingly. To adjust the temperature measured by the infrared thermometer, Equation 4.1 was solved for the actual temperature:

$$T_{adju} = \frac{T_{infr}}{\varepsilon_{calc}^{1/4}} \qquad 4.2$$

where T_{adju} is the adjusted temperature, T_{infr} is the temperature recorded by the infrared thermometer, and ε_{calc} is the emissivity calculated in Equation 4.1. The accuracy of the infrared thermometer was within 0.5% of the measured temperature for temperatures below 1500 ºC, and within 1% of the measured temperature above 1500 ºC, according to the manufacturer.[112] For the remainder of this thesis, all reported temperatures and calculations involving temperature are adjusted from the measured temperatures using Equation 4.2 and assuming an emissivity of 0.97. The error associated with the adjusted temperature is based on the stated accuracy of the infrared thermometer.

In future experiments, to ensure more accurate temperature measurement by the infrared thermometer, the first experiment of every day should be a spark plasma sintering run with a maximum temperature below the working limit of the type-K thermocouple (1250 ºC).[121] In the first experiment, the infrared thermometer emissivity setting should be set to one (perfect blackbody emissivity). The thermocouple should be used in tandem with the infrared thermometer, and after the sintering cycle, Equation 4.1

should be applied to the recorded temperatures to find the average emissivity. The infrared thermometer should then be calibrated according to the average emissivity to record more accurate temperatures during SPS.

Another potential source of error in temperature measurement by the infrared thermometer was the clarity of the amorphous silica window. Impurities within the SPS chamber (e.g., hand oils, vacuum grease) were volatilized and deposited on the SPS chamber windows during sintering (Figure 4.8), and these deposits may have impeded light emitted from the die from being transmitted though the window. These deposits may have resulted in inaccurate temperatures recorded by the infrared thermometer. To reduce the effects of these deposits, the amorphous silica window was removed from the SPS chamber after each sintering run and cleaned with ethanol and a non-abrasive cloth. Although the deposited material could be removed between sintering runs, materials deposited during the sintering process could not be removed *in-situ*. It was assumed that the emissivity calculated in Equation 4.2 is also a function of the silica window, and no further adjustments were made to the recorded temperatures.

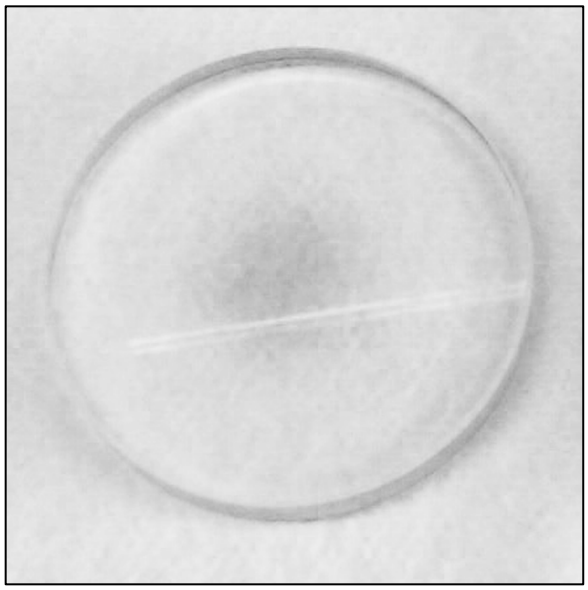

Figure 4.8. Material deposited (dark shading in center) on the amorphous silica window. The material is deposited during SPS and may obstruct certain wavelengths of light from reaching the infrared thermometer, leading to an inaccurate temperature measurement. The streak of white in the image is the reflection of a fluorescent light and not a real artifact.

4.3. Densification of SPS Tungsten and Tungsten-Ceria

4.3.1. Estimated Error of Density Measurements

The densities for all spark plasma sintered and hot pressed samples were determined using water displacement methods outlined in ASTM Standard B311 and ASTM Standard B962, and the methods are described in Sections 3.7.2 and 3.7.3, respectively. The balance used had an accuracy of ±0.001 g and the thermometer had an accuracy of ±0.1 ºC. The error associated with the mass of the samples immersed in water was assumed to be ±0.005 g due to the possibility of the samples absorbing water or containing trapped air bubbles. The error of the densities reported in the remainder of

this thesis are based on the multivariate propagation of error formula given by Navidi,[122] and typically range between 0.02 and 0.05 of the fractional densities for pure tungsten.

4.3.2. Effects of Pressure, Temperature and Time on Densification of Tungsten and Tungsten-Ceria

Two applied pressures, 42 and 64 MPa, were used in this study to determine whether pressure has a significant effect on the densification of SPS tungsten and SPS tungsten-ceria. Samples of pure tungsten, W-1CeO_2, W-10CeO_2, and W-20CeO_2 were spark plasma sintered at 1300, 1400, 1500, 1600, and 1700 ºC for 2 min with an applied pressure of 42 or 64 MPa (Figure 4.9).

Based on the plots in Figure 4.9, the increased pressure appears to have the greatest effect on the density of pure tungsten between 1300 and 1500 ºC, while the increase in pressure does not seem to affect the ceria-bearing samples. The higher densities observed in the pure tungsten sintered with 64 MPa might imply that higher pressures aided particle packing, or that the mechanism of densification may have changed with the increased pressure. In sintering, powder compacts with higher initial densities typically produce sintered compacts with higher final densities.[25] However, if particle rearrangement was responsible for the difference in final density of pure tungsten, the same effect would be anticipated in the tungsten-ceria samples.

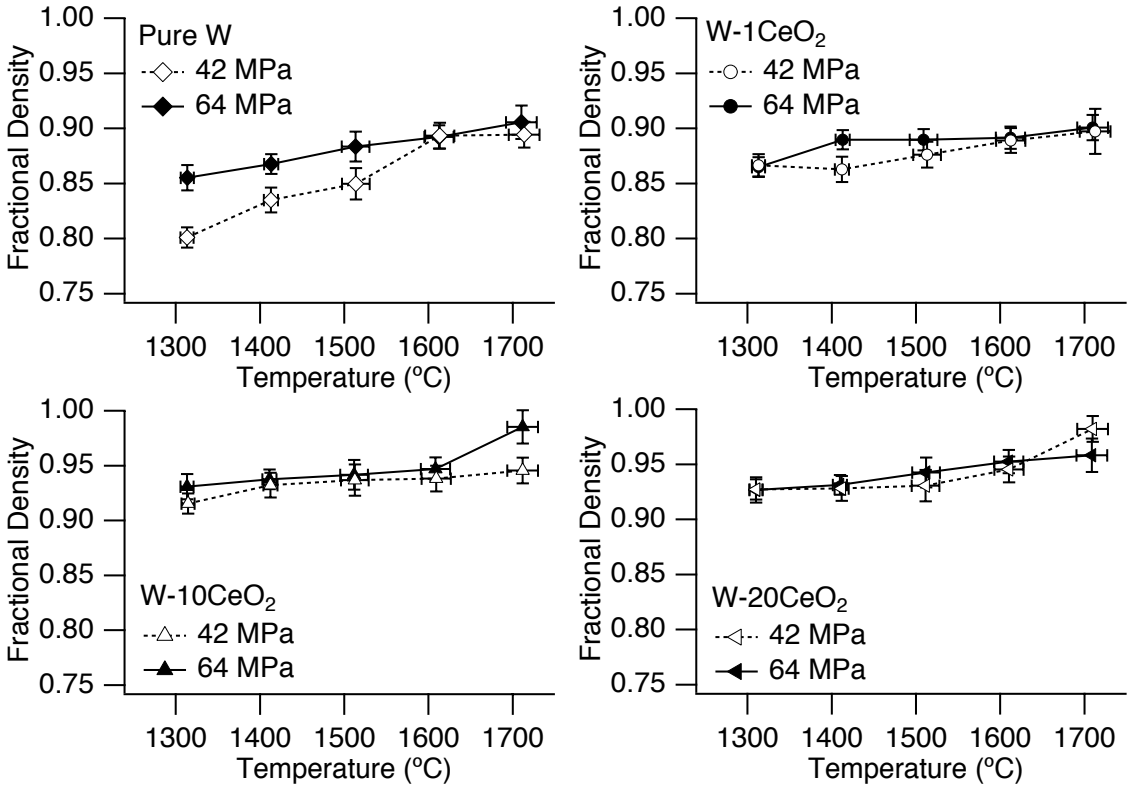

Figure 4.9. Comparison of the effects of applied pressure on the densities of SPS tungsten, W-1CeO_2, W-10CeO_2, and W-20CeO_2 between 1300 and 1700 ºC. All samples were produced with a 2 min soak time. The error bars on the fractional densities are based on the measurement error described in Section 4.3.1, and the error bars on the temperatures are based on the accuracy range of the infrared thermometer.

The addition of 1 wt% ceria to the tungsten did not appear to influence the final fractional density relative to pure tungsten sintered with 64 MPa applied pressure. Chen reported that in pressureless sintering, the shinkage curves produced for pure tungsten and W-1CeO_2 were similar,[102] and the results from Chen imply that the final sintered density of pure tungsten and W-1CeO_2 are similar, which is in agreement with the results in Figure 4.9.

The W-10CeO_2 and W-20CeO_2 parts had fractional densities exceeding 0.90 for both pressures in the temperature range 1300 to 1700 ºC. The reason for this higher density relative to the pure tungsten samples is unknown. It is possible that during spark plasma sintering the ceria began to volatilize out of the compact, and the weight percent of ceria in the sintered compact could be lower than the original 10 or 20 wt% added to the tungsten. This would increase the theoretical density of the parts, as tungsten has a density of 19.25 g/cm^3 and ceria has a density of 7.13 g/cm^3. Because the weight percent of ceria might be lower in these samples, the fractional density would be higher. This potential loss of ceria is discussed further in Section 4.6. It is also possible that the addition of ceria aids in densification at lower temperatures.

To determine if the ceria-bearing samples densified at a lower temperature than pure tungsten, pure tungsten and W-10CeO_2 were spark plasma sintered in 100 ºC increments between 800 and 1800 ºC for 2 min each at an applied pressure of 64 MPa (Figure 4.10). Based on the results in Figure 4.10, the densification curves of pure tungsten and W-10CeO_2 are similar and the hypothesis that ceria aids in densification is not supported. Further study is required to determine if ceria aids in the densification of tungsten.

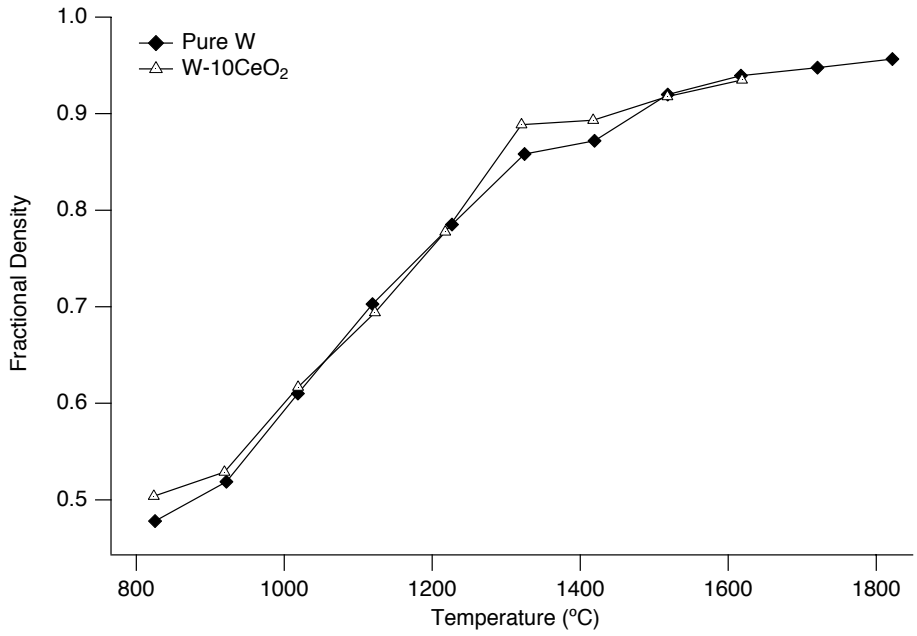

Figure 4.10. Fractional density of pure tungsten and W-10CeO_2 spark plasma sintered between 800 and 1800 ºC. All samples were sintered for 2 min at temperature and at an applied pressure of 64 MPa. For clarity, the error bars for the temperature are not shown. The error associated with the density measurements is contained within the plot markers and are not shown.

Spark plasma sintering has previously been reported to produce higher density compacts at lower temperatures than pressureless sintering or hot pressing.[16,56,66] The SPS pure tungsten data shown in Figure 4.10 was compared to pressureless sintering curves for pure tungsten measured by Chen (Figure 4.11).[102] A comparison of the data sets in Figure 4.11 shows that within the temperature range 800 to 1800 ºC, the spark plasma sintered tungsten, for a given temperature, has a higher density than that produced by pressureless sintering.

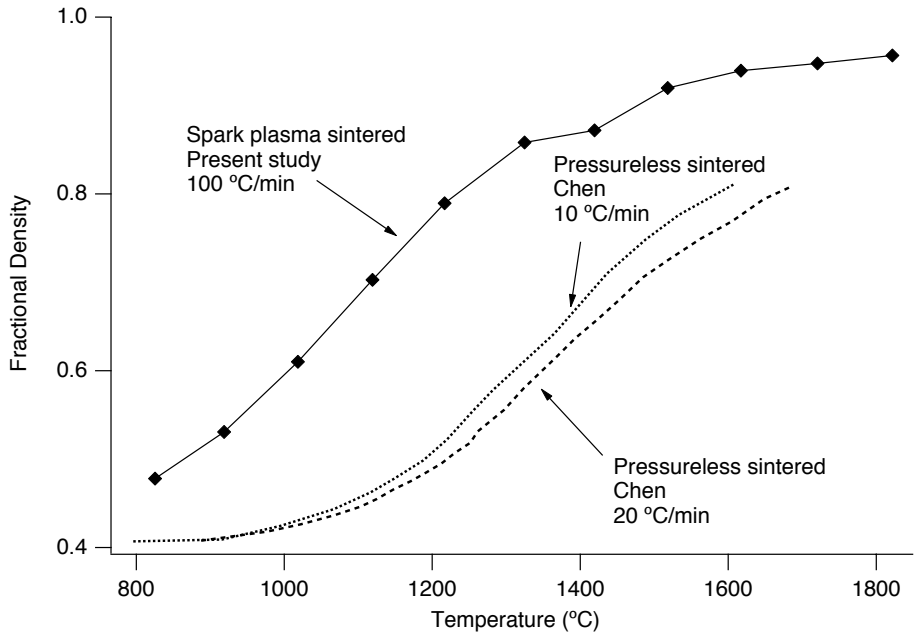

Figure 4.11. Comparison of the measured density of spark plasma sintered tungsten between 800 and 1800 ºC at 100 ºC/min and dilatometry curves of produced by Chen[102] for pressureless sintering of tungsten at 10 and 20 ºC/min. Spark plasma sintering appears to produce higher density tungsten parts at lower temperatures than conventional sintering. For clarity, the error bars for the temperature are not shown. The error associated with the density measurements is contained within the plot markers and is not shown.

The comparison between spark plasma sintering and pressureless sintering assumes the applied pressure in spark plasma sintering is negligible. Even at low applied pressures, the densification and grain growth of a compact are affected.[25] Arguably, a better analog to spark plasma sintering is uniaxial hot pressing (HP). In addition to producing pure tungsten parts by SPS, pure tungsten parts were also produced by uniaxial hot pressing. The spark plasma sintered compacts and the hot pressed compacts were

produced from the same powder lot with the same process history. In both consolidation methods, the applied pressure was a constant 42 MPa. The spark plasma sintered samples were heated at 40 ºC/min and held at a maximum temperature of 1300, 1400, 1500, 1600, or 1700 ºC for 2 min. The hot pressed samples were heated at 30 ºC/min and held at a maximum temperature of 1400, 1500, or 1600 ºC for 30 min. The sintered densities of the spark plasma sintered tungsten and hot pressed tungsten are shown in Figure 4.12.

Based on the results in Figure 4.12, at similar sintering temperatures, the parts produced by SPS have a higher density than the parts produced by hot pressing. Intuitively, greater sintering times should yield higher density parts; however, this is not the case when comparing spark plasma sintering and hot pressing. The SPS samples were held at maximum temperature for 2 min, whereas the HP parts were held at maximum temperature for 30 min; yet the SPS samples had greater sintered densities than the HP samples. Previous studies comparing SPS and HP have yielded similar results. For example, Angerer *et al.*[123] compared spark plasma sintering and hot pressing of tantalum, and found that to achieve the same density, a 1 min soak time in SPS was equivalent to a 60 min soak time in HP at 1500 and 1700 ºC.

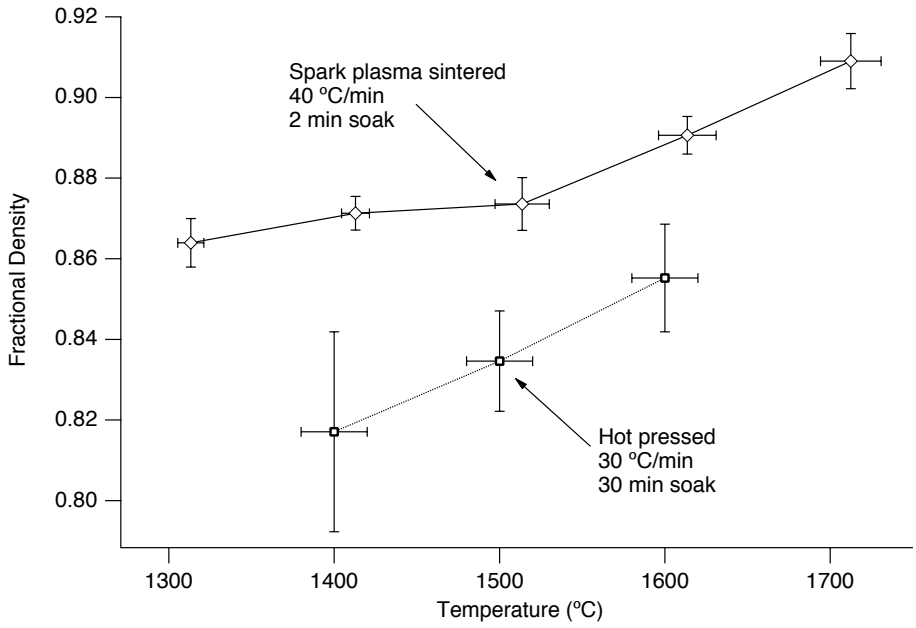

Figure 4.12. Comparison of the measured densities of spark plasma sintered tungsten and hot pressed tungsten. All samples were sintered with an applied pressure of 42 MPa. The error bars on the fractional densities are based on the measurement error described in Section 4.3.1. The error bars on the spark plasma sintering temperatures are based on the accuracy range of the infrared thermometer. The error bars on the hot pressing temperatures are based on the range of temperatures measured during the sample dwell.

The difference in densities between SPS tungsten and HP tungsten is easily identifiable in the micrographs of the samples (Figure 4.13). In the SPS samples, the pores are smaller than the HP samples, and the pores in the SPS samples are more discreet than the pores in the HP samples.

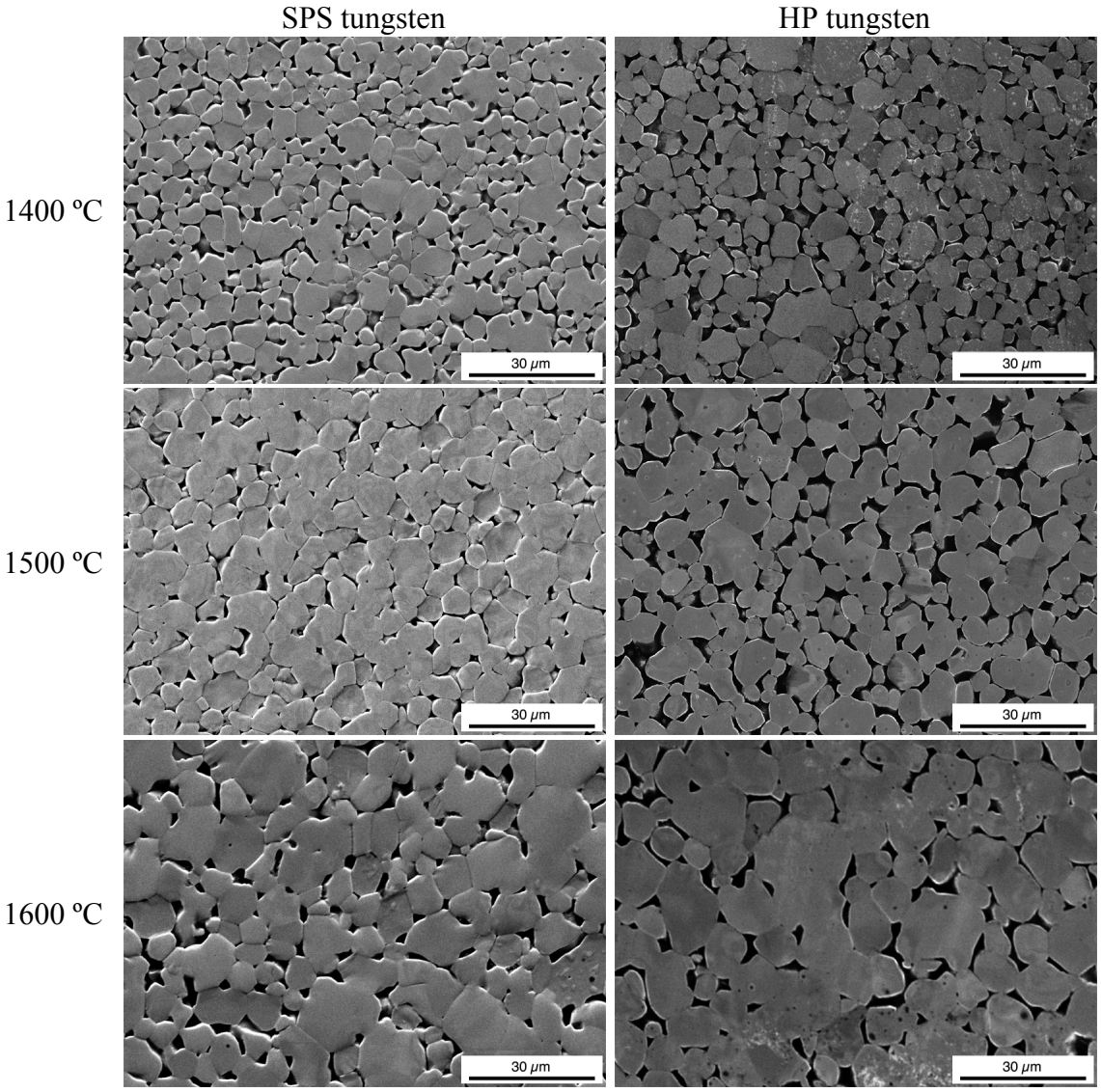

Figure 4.13. Microstructure comparison of tungsten consolidated by spark plasma sintering and by hot pressing. Both sets of samples were produced with an applied pressure of 42 MPa. The SPS samples were heated at 40 ºC/min and soaked at maximum temperature for 2 min. The HP samples were heated at 30 ºC/min and soaked at maximum temperature for 30 min. The light phase is tungsten, and the dark phase are pores.

The effect of isothermal soak time on the final density of pure tungsten and W-10CeO_2 was also investigated. The powders were spark plasma sintered at 900, 1200, and 1500 ºC, and the samples were sintered between 2 and 20 min. The densities of these samples is shown in Figure 4.14.

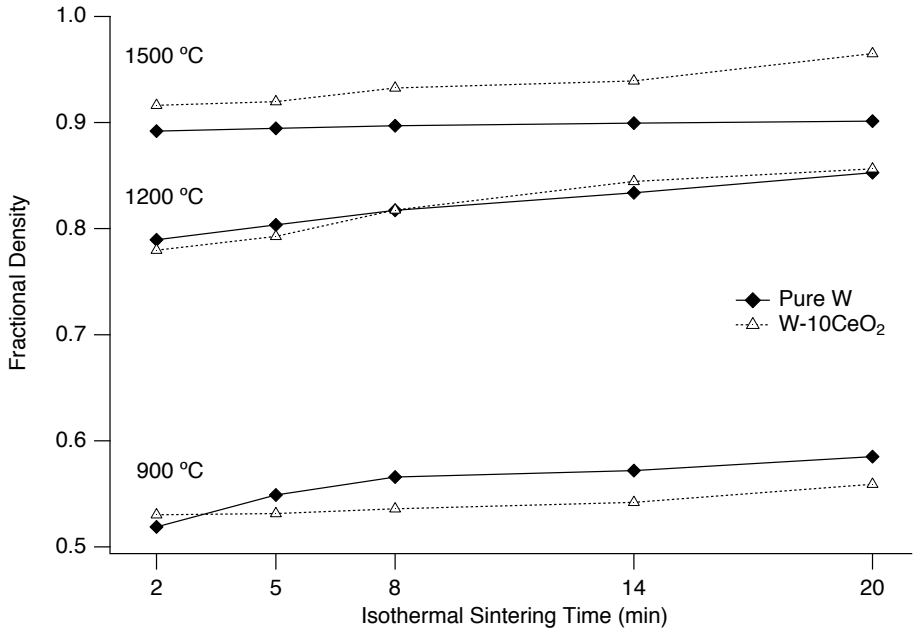

Figure 4.14. Fractional sintered density of pure tungsten and W-10CeO_2 for samples spark plasma sintered between 2 and 20 min at 900, 1200, and 1500 ºC and a constant 64 MPa applied pressure. The error associated with the density measurements are contained within the plot markers and are not shown.

The isothermal soaks did not produce as dramatic changes in density as did the different sintering temperatures shown in Figure 4.10. In pure tungsten, the fractional sintered density increased from 0.52 to 0.59 at 900 ºC and from 0.79 to 0.85 at 1200 ºC. Similarly, the W-10CeO_2 fractional sintered density increased from 0.53 to 0.56 at 900 ºC and from 0.78 to 0.86 at 1200 ºC. At 1500 ºC, the pure tungsten did not have a

statistically significant change in density, and all samples had fractional densities between 0.89 and 0.90. However, the W-10CeO_2 did have a significant change in density at 1500 ºC, and the fractional sintered density increased from 0.92 to 0.97. This increase in density at 1500 ºC may not be due to ceria enhancing the densification of tungsten, but it may be due to a loss of ceria during sintering. The fractional density calculations were based on the assumption that 10 wt% ceria was present in the sample after sintering. If, however, the ceria content were less than 10 wt% in the final samples, the reported densities would be artificially high. This is because the density of tungsten is 19.25 g/cm^3 and the density of ceria is 7.13 g/cm^3, and if a greater proportion of tungsten were present, the sample would appear to be denser. The potential loss of ceria is discussed further in Section 4.6.

In summation of these results, pressure, temperature, and time affect the final sintered densities of pure tungsten and tungsten-ceria parts. The final sintered density does not show a pressure correlation in ceria-bearing samples; however, higher pressures appear to increase the density of pure tungsten between 1300 and 1500 ºC. Spark plasma sintering produces higher density compacts at a given temperature and shorter soak times than pressureless sintering or hot pressing. At 900 and 1200 ºC in spark plasma sintering, as the soak time is increased, the final densities of tungsten and W-10CeO_2 are increased. However, this effect is not as pronounced as a change in sintering temperature. At 1500 ºC, the density of W-10CeO_2 appears to be time dependent, but this may be due to a loss of ceria during SPS.

4.4. Grain Growth of SPS Tungsten and Tungsten-Ceria

4.4.1. Confidence Intervals for Average Grain Size Measurements

To estimate the average grain sizes of spark plasma sintered tungsten and tungsten-ceria, confidence intervals were used rather than the normal standard deviations, because the grain size distributions fit a lognormal distribution, which skews the normal standard deviation to unreasonable values. For example, 3430 grain intercepts were measured by the lineal intercept method using EBSD for a tungsten sample that was spark plasma sintered for 2 min at 1500 ºC. The average grain size of the sample was 2.4 μm, and the normal standard deviation was 1.2 μm. Alternatively, the grain size data were fit to lognormal distributions, and 95% confidence intervals for the average grain size were found using the Cox method[119] (Figure 4.15). At a 95% confidence level, the average grain size of the SPS tungsten sample sintered for 2 min at 1500 ºC is between 2.4 and 2.5 μm. The Cox method[119] is used in the remainder of this thesis to estimate the average grain size.

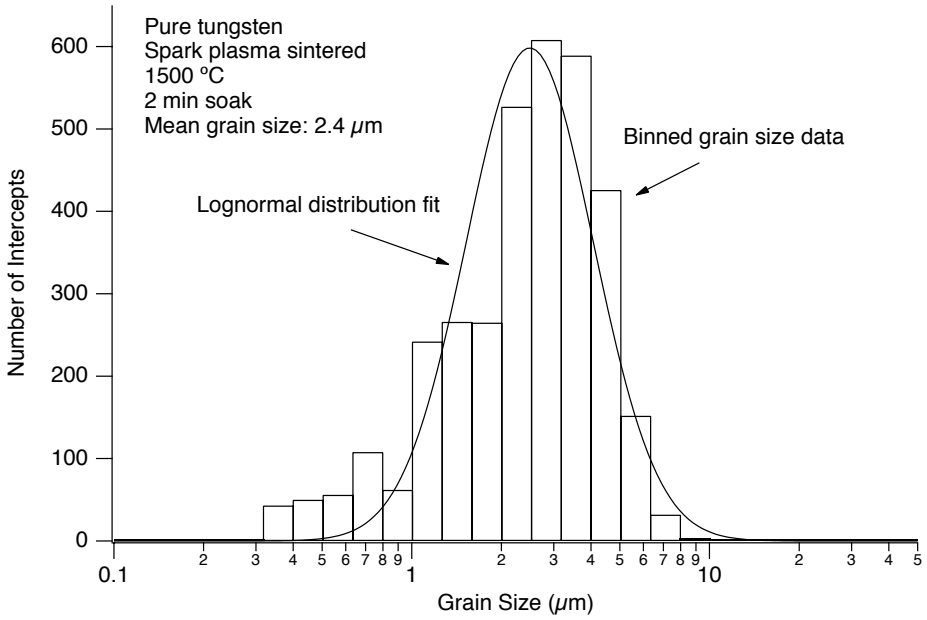

Figure 4.15. Example of tungsten grain size distribution measured by the lineal intercept method using EBSD and fit to a lognormal distribution. The distribution shown is for tungsten spark plasma sintered at 1500 ºC for 2 min. A total of 3430 grain intercepts were used to construct this distribution. The average grain size is between 2.4 and 2.5 μm at a 95% confidence level, based on the Cox method.[119]

4.4.2. Effects of Pressure, Temperature and Time on Grain Growth of Tungsten and Tungsten-Ceria

Two applied pressures, 42 and 64 MPa, were used in this study to determine whether pressure has a significant effect on the final average grain size of SPS tungsten and SPS tungsten-ceria. Samples of pure tungsten, W-1CeO_2, W-10CeO_2, and W-20CeO_2 were spark plasma sintered at 1300, 1400, 1500, 1600, and 1700 ºC for 2 min with an applied pressure of 42 or 64 MPa (Figure 4.16). In Figure 4.16, pressure appears to have a slight effect on the final average grain size of pure tungsten between 1300 and

1600 ºC. In these samples, the higher pressure (64 MPa) resulted in a larger average grain size than the lower pressure (42 MPa). This result is not unexpected, because the higher effective pressures at the particle contacts increase the driving force for diffusion between tungsten particles, enhancing both densification and grain growth.[25]

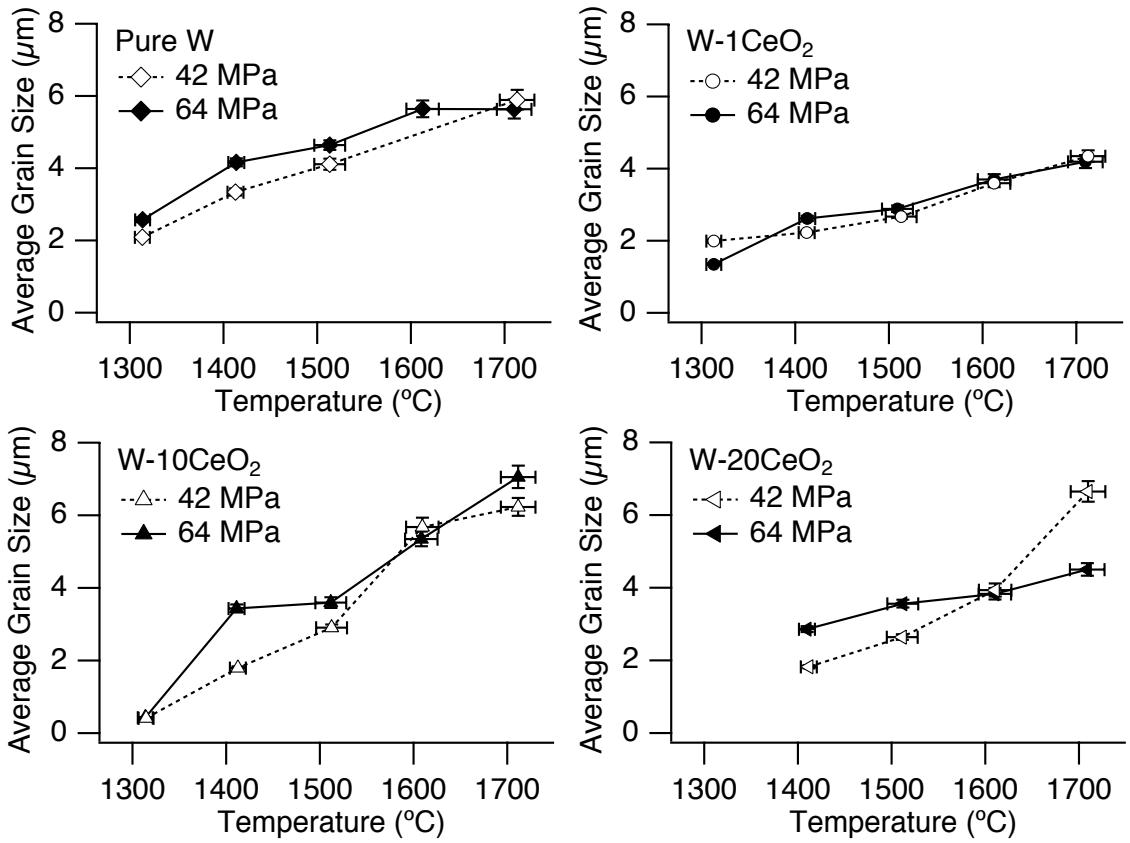

Figure 4.16. Comparison of the effects of applied pressure on the average tungsten grain sizes of SPS tungsten, W-1CeO_2, W-10CeO_2, and W-20CeO_2 between 1300 and 1700 ºC. All samples were produced with a 2 min soak time. The error bars on the average grain sizes are based on a 95% confidence interval found using the Cox method,[119] and the error bars on the temperatures are based on the accuracy range of the infrared thermometer.

Pressure does not appear to have a significant effect on the average grain size of the W-1CeO_2 samples (Figure 4.16). For the W-1CeO_2 samples sintered between 1400 and 1700 ºC, the average grain sizes are statistically the same at a given temperature for both 42 and 64 MPa. As stated previously, pressure increases the driving force for grain growth; however, the addition of 1 wt% ceria inhibits tungsten grain growth. This is due to the ceria segregating to grain triple junctions and pinning the tungsten grain boundaries, which limits grain growth.[18] This effect is present in oxide dispersion strengthened alloys, whereby an oxide powder is added to a metal to refine the grain size of the parent material.[102] The boundary pinning effect is likely more significant than the applied pressure, which is why pressure does not appear to affect the final grain size of W-1CeO_2 compacts. If the ceria does inhibit grain growth by pinning, the average grain size of the W-1CeO_2 samples should be smaller than the average grain size of pure tungsten at a given temperature and pressure. Based on the data shown in Figure 4.16, the average grain sizes of the W-1CeO_2 compacts are smaller than those of the pure tungsten compacts, which lends credence to the hypothesis that pinning may be occurring. Further experiments on W-1CeO_2 and pure tungsten are necessary to confirm this hypothesis.

There does not appear to be a direct correlation between the applied pressure and average grain size in the W-10CeO_2 samples and the W-20CeO_2 samples, based on the data in Figure 4.16. The average grain sizes for the samples sintered between 1300 and 1600 ºC are smaller than those of the pure tungsten. This may not be a result of a pinning effect, but may be due to isolation of the tungsten particles within the ceria phase. If tungsten particles were not in contact during sintering, this would mean the tungsten

would have to diffuse through the ceria phase for the tungsten particles to grow. Comparing the microstructures of pure tungsten, W-1CeO_2, W-10CeO_2, and W-20CeO_2 produced at 1500 ºC, visually the W-10CeO_2 and W-20CeO_2 samples have an easily distinguishable ceria phase that may have formed a barrier for tungsten particle growth (Figure 4.17).

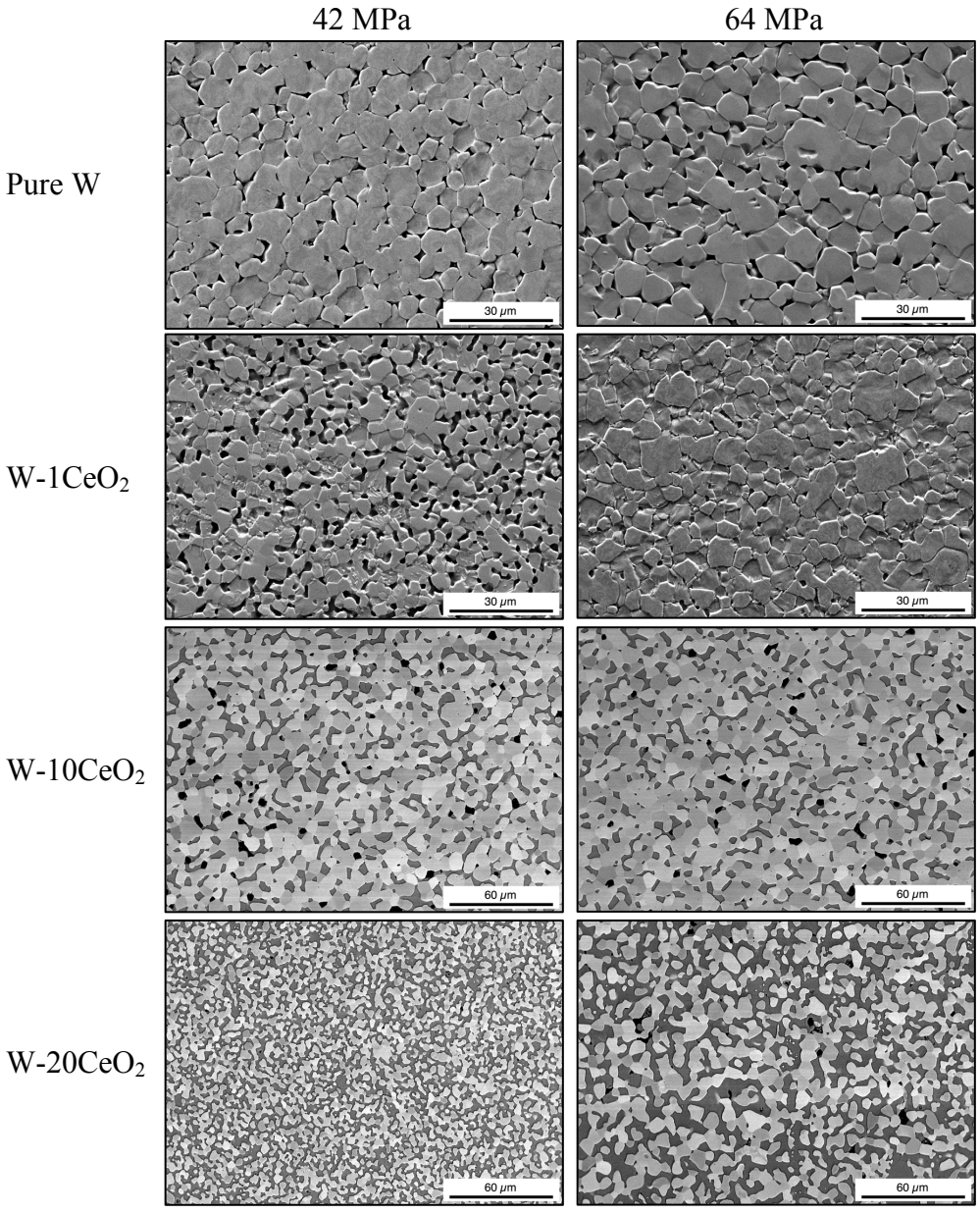

Figure 4.17. Microstructure comparison of the effect of pressure on pure tungsten, W-1CeO_2, W-10CeO_2, and W-20CeO_2. The pure tungsten and W-1CeO_2 images are secondary electron image, and the W-10CeO_2 and W-20CeO_2 images are backscatter electron images. In the backscatter images, the lightest phase is tungsten, the darker phase is ceria, and the darkest areas are pores.

Pure tungsten was also spark plasma sintered between 800 and 1800 ºC to determine the temperature at which grain growth begins, and to determine how grain growth progresses with increasing temperature. The samples were heated in 100 ºC increments with an applied pressure of 64 MPa, and the samples were soaked at maximum temperature for 2 min. The grain sizes were measured by electron backscatter diffraction (EBSD), and the results are shown in Figure 4.18. Due to particle pullout during polishing, the 800 and 900 ºC samples could not be polished well enough to collect grain size data by EBSD, and these grain sizes are not reported in Figure 4.18.

The grain sizes of the samples sintered between 1300 and 1700 ºC shown in Figure 4.18 are smaller than the pure tungsten grain sizes reported in Figure 4.16. This phenomenon likely occurred because the samples shown in Figure 4.16 were heated at 40 ºC/min, and the samples in Figure 4.18 were heated at 100 ºC/min. The lower heating rate increased the total sintering time to reach the maximum temperature; and because grain growth is highly dependent on sintering time,[25] the samples produced at 40 ºC/min had a larger average grain size than the samples produced at 100 ºC/min.

The average grain sizes of the 1000 and 1100 ºC samples were about 0.3 μm. These grain sizes are comparable to the 0.26 μm average crystallite size of the tungsten powder. Based on the close proximity of the grain sizes and the original particle sizes, grain growth likely did not occur in the 1000 and 1100 ºC samples. The absence of clearly-defined grain boundaries can be seen in the micrograph of the 1000 ºC sample (Figure 4.19). Grain growth did occur in the 1200 ºC sample, and the grain size increased from about 0.3 μm to 0.4 μm. The emergence of grain boundaries in the 1200 ºC sample

can be seen in Figure 4.19. Grain growth was observed at all temperatures greater than 1200 ºC, and examples of this continued growth can be seen in Figure 4.19.

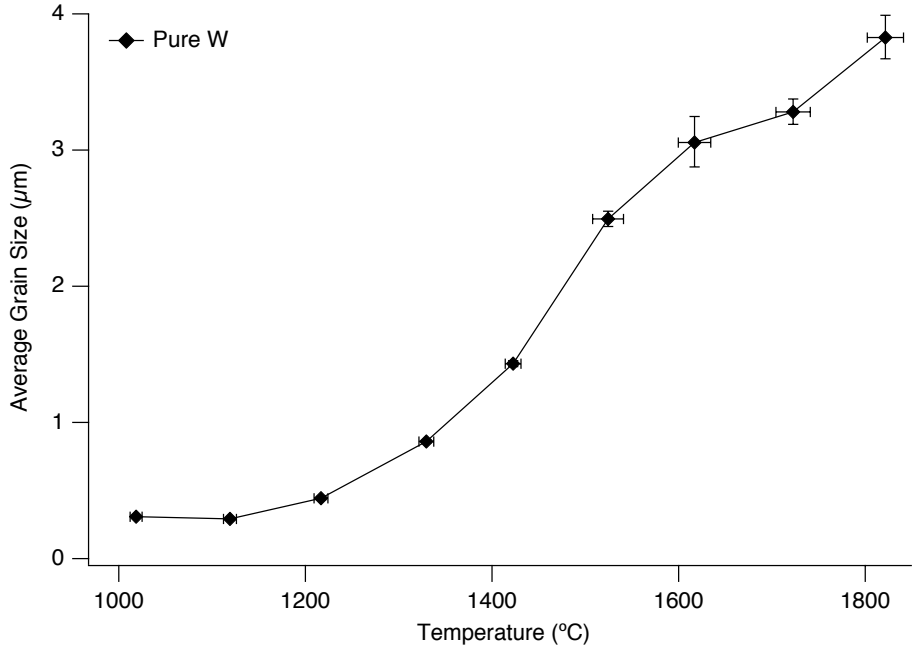

Figure 4.18. Average grain sizes of pure tungsten samples spark plasma sintered between 1000 and 1800 ºC. The error bars on the average grain sizes are based on a 95% confidence interval found using the Cox method,[119] and the error bars on the temperatures are based on the accuracy range of the infrared thermometer. For the samples produced between 1000 and 1400 ºC, the grain size distribution is small enough that the error bars are contained within the plot markers.

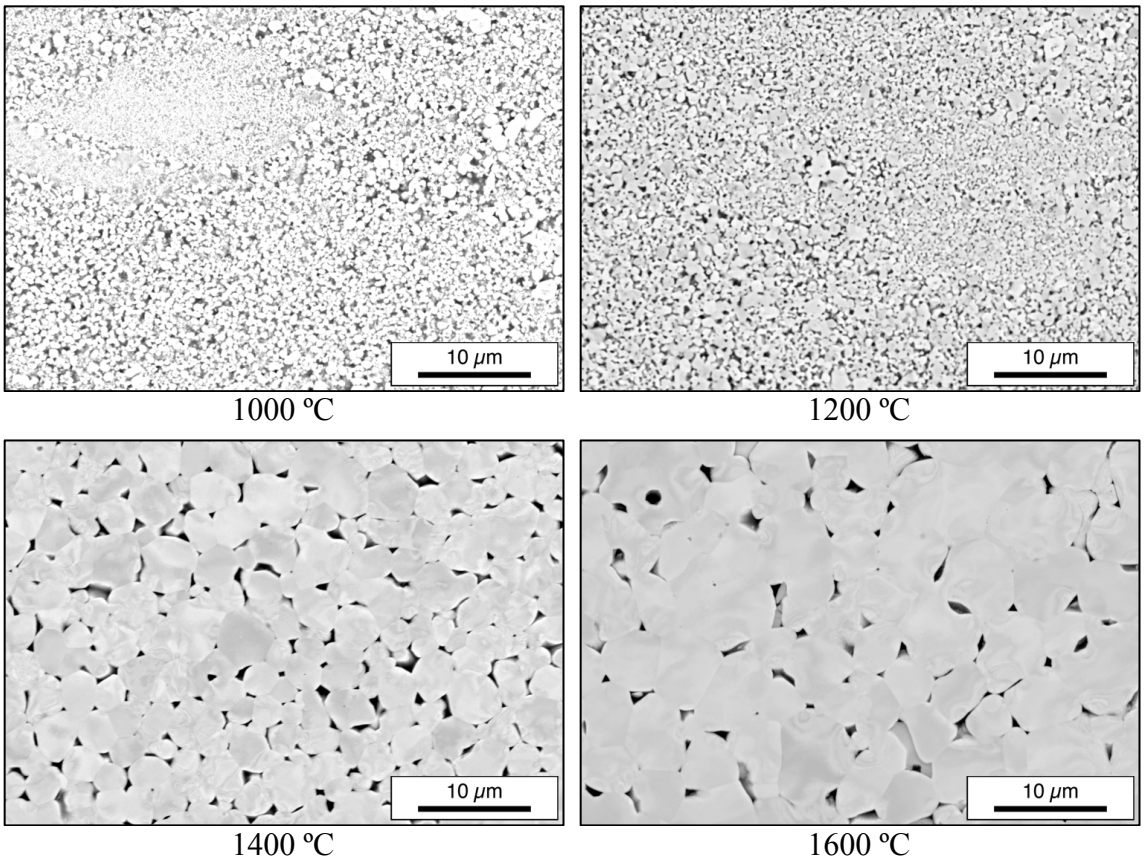

Figure 4.19. Microstructures of pure tungsten spark plasma sintered at 1000, 1200, 1400, and 1600 ºC. All samples were sintered with an applied pressure of 64 MPa and heated at 100 ºC/min. The samples were soaked at maximum temperature for 2 min. The light areas are tungsten, and the dark areas are pores.

The average grain sizes of spark plasma sintered tungsten were compared to the average grain sizes of hot pressed tungsten. The spark plasma sintered compacts and the hot pressed compacts were produced from the same powder lot with the same process history. In both consolidation methods, the applied pressure was a constant 42 MPa. The spark plasma sintered samples were heated at 40 ºC/min and held at a maximum temperature of 1300, 1400, 1500, or 1700 ºC for 2 min. The hot pressed samples were

heated at 30 ºC/min and held at a maximum temperature of 1300, 1400, 1500, or 1600 ºC for 30 min. The average grain sizes for the spark plasma sintered tungsten and hot pressed tungsten are shown in Figure 4.20.

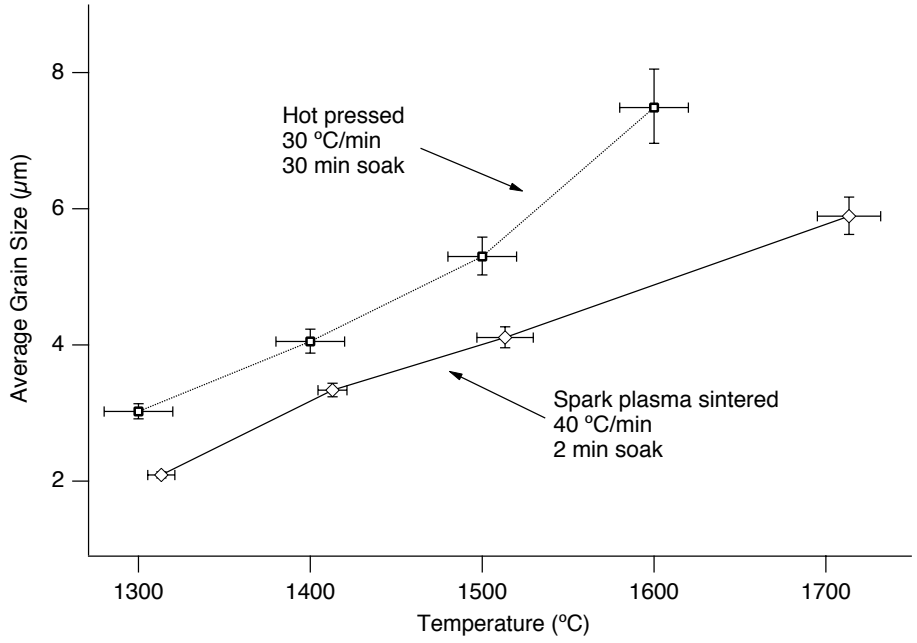

Figure 4.20. Comparison of the average grain sizes of spark plasma sintered tungsten and hot pressed tungsten. All samples were sintered with an applied pressure of 42 MPa. The error bars on the average grain sizes are based on a 95% confidence interval found using the Cox method.[119] The error bars on the spark plasma sintering temperatures are based on the accuracy range of the infrared thermometer. The error bars on the hot pressing temperatures are based on the range of temperatures measured during the sample dwell.

Based on the results shown in Figure 4.20, at similar sintering temperatures, the parts produced by SPS have smaller average grain sizes with tighter grain size distributions than the parts produced by HP. The difference in grain size can be easily seen in Figure 4.13. The larger grain sizes in the hot pressed samples may be attributed to the longer isothermal sintering time and the slower heating rate than the spark plasma sintered samples. Spark plasma sintering has been previously cited as limiting grain growth and creating tighter grain size distributions than other sintering techniques.[14,66,76]

In addition to comparing the grain sizes of pure tungsten compacts produced by SPS and HP, the average grain sizes of spark plasma sintered W-4CeO_2 samples were compared with the average grain sizes of hot pressed W-4CeO_2 samples. The spark plasma sintered compacts and the hot pressed compacts were produced from the same powder lot with the same process history. In both consolidation methods, the applied pressure was a constant 42 MPa. The spark plasma sintered samples were heated at 40 ºC/min and held at a maximum temperature of 1300, 1400, 1500, or 1600 ºC for 2 min. The hot pressed samples were heated at 30 ºC/min and held at a maximum temperature of 1300, 1400, 1500, or 1600 ºC for 30 min. The average grain sizes for the spark plasma sintered tungsten and hot pressed tungsten are shown in Figure 4.21.

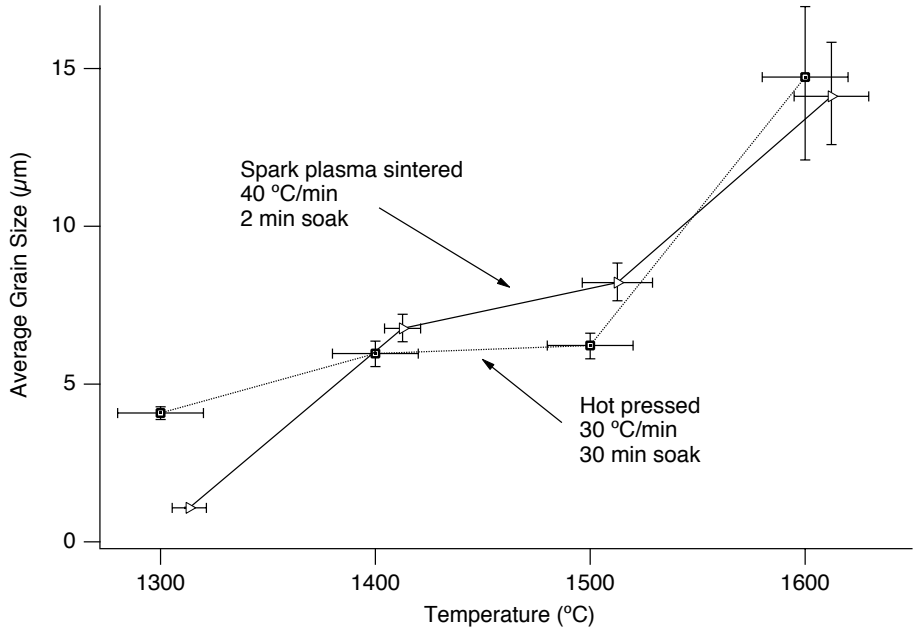

Figure 4.21. Comparison of the average tungsten grain sizes of spark plasma sintered W-4CeO_2 and hot pressed W-4CeO_2. All samples were sintered with an applied pressure of 42 MPa. The error bars on the average grain sizes are based on a 95% confidence interval found using the Cox method.[119] The error bars on the spark plasma sintering temperatures are based on the accuracy range of the infrared thermometer. The error bars on the hot pressing temperatures are based on the range of temperatures measured during the sample dwell.

Based on the results shown in Figure 4.21, at similar sintering temperatures, the samples produced by SPS and by HP have similar grain size distributions. For the samples produced at 1600 ºC, the grain sizes are statistically the same. This result is counterintuitive, because the samples with longer soak times (the HP samples) should have larger average grain size than samples soaked with shorter soak times (the SPS samples). The similarity in grain sizes between the SPS and HP samples produced at 1400, 1500, and 1600 ºC can be seen in the microstructures, and the largest difference can be seen in the samples produced at 1300 ºC (Figure 4.22). It is not clear why the grains are similar in size, and there are no similar results available in the open literature. Future work is required to understand this phenomenon.

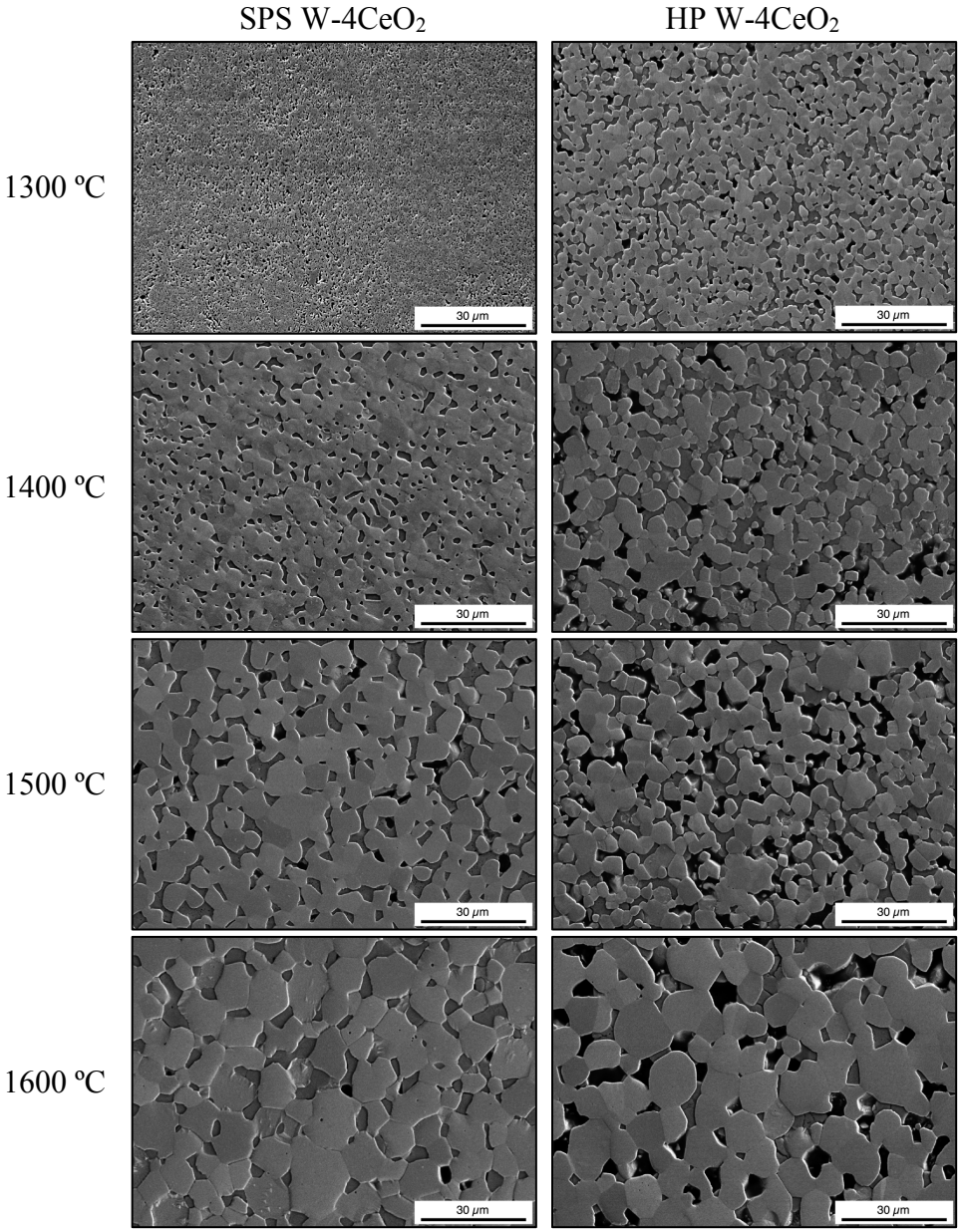

Figure 4.22. Microstructure comparison of W-4CeO_2 consolidated by spark plasma sintering and by hot pressing. Both sets of samples were produced with an applied pressure of 42 MPa. The SPS samples were heated at 40 ºC/min and soaked at maximum temperature for 2 min. The HP samples were heated at 30 ºC/min and soaked at maximum temperature for 30 min. The lightest phase is tungsten, the darker phase is ceria, and the darkest phase is pores.

To study the effect of time on grain growth, pure tungsten was spark plasma sintered at 1200, 1500, and 1800 ºC between 2 and 26 min, and W-10CeO_2 was spark plasma sintered at 1200 and 1500 ºC between 5 and 20 min, and the results are shown in Figure 4.23.

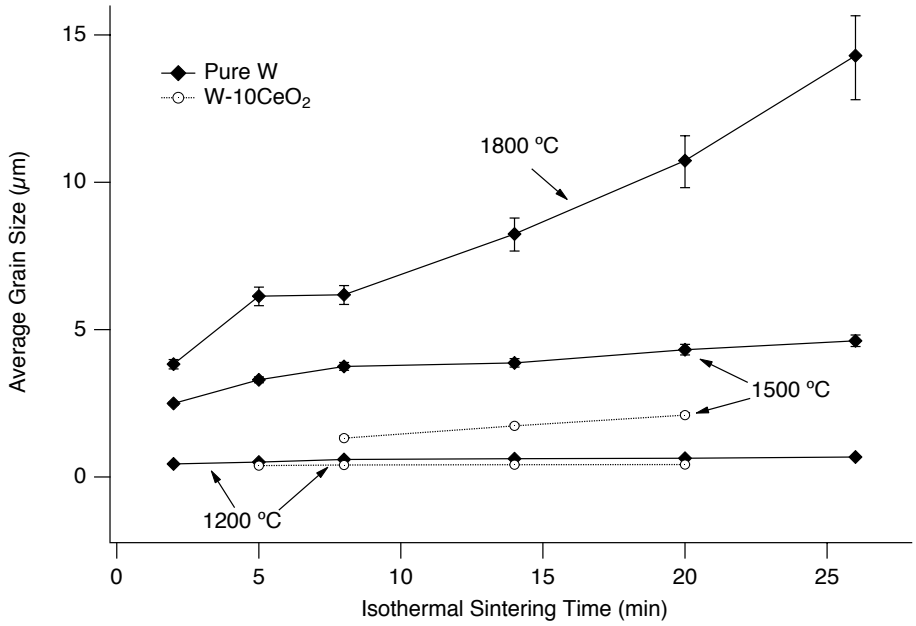

Figure 4.23. Average tungsten grain size of pure tungsten and W-10CeO_2 for samples spark plasma sintered between 2 and 26 min at 1200, 1500, and 1800 ºC and a constant 64 MPa applied pressure. The error bars on the average grain sizes are based on a 95% confidence interval found using the Cox method.[119] For some of the samples, the grain size distribution is small enough that the error bars are contained within the plot markers.

At 1200 ºC, the average grain size of the pure tungsten grew from about 0.4 μm to about 0.7 μm between 2 and 26 min, whereas the average grain size of W-10CeO_2 remained statistically the same between 5 and 20 min. At 1500 ºC, the average grain size

of the pure tungsten increased from 2.5 to 4.6 μm between 2 and 26 min. The addition of 10 wt% ceria appears to have limited the growth of tungsten grains at 1500 ºC relative to pure tungsten, and the tungsten grains grew from 1.3 to 2.1 μm between 8 and 20 minutes. The limited growth in the W-10CeO_2 samples may be due to the tungsten grains being separated by the ceria phase, and for the tungsten grains to grow, the tungsten would need to diffuse through the ceria phase. The results in this thesis cannot confirm this hypothesis, and further studies are needed to determine why the growth of tungsten grains is limited in W-10CeO_2.

The most significant grain growth in pure tungsten occurred at 1800 ºC. The average grain size was 3.8 μm after 2 min of isothermal sintering, and the average grain size was 14.3 μm after 26 min of isothermal sintering. In normal grain growth, the rate of growth is assumed to be proportional to the curvature of the grains at a given time.[124] Therefore, as the grains coarsen, the curvature is decreased, and the rate should diminish as well. However, in the samples spark plasma sintered between 8 and 26 min, the grain growth rate appears to increase as grain size is increased. As these tungsten grains grow, the 95% confidence intervals on the average grain sizes increases, which implies the variation in the grain sizes increases with time. Straumal *et al.* observed the same phenomenon in their study on the grain growth of polycrystalline tungsten at 2000 ºC.[125] The researchers found that when the grain size distribution broadened, it was due to abnormal grain growth in some of the tungsten grains.[125] Straumal *et al.* showed that samples exhibiting abnormal grain growth were textured, and that about 50% of the grains in the <110> and <112> directions were clustered and not randomly distributed.[125] Based on this texturing, the researchers concluded that the abnormal grain growth was

due to high-mobility misorientations between the smaller grains and the larger grains, and these smaller grains were consumed at a higher rate than in normal grain growth.[125] Abnormal grain growth may be occurring in SPS tungsten at 1800 ºC, and future work on grain orientation is necessary to determine the mechanism of grain growth.

The average grain sizes of pure tungsten that was spark plasma sintered at 1500 and 1800 ºC between 2 and 26 min was compared to the grain sizes of pressureless sintered tungsten[105] and hot pressed tungsten[82] (Figure 4.24). The SPS tungsten samples produced at 1500 ºC had similar grain sizes to the hot pressed tungsten produced by Karpinos *et al.*[82] at 1800 ºC. The similarity between the SPS grain sizes at 1500 ºC and the HP grain sizes at 1800 ºC may be due to the difference in applied pressures and consolidation techniques. In the SPS study, the applied pressure was 64 MPa, whereas in the HP study the applied pressure was 14.7 MPa. Higher sintering pressures increase the effective pressures at the particle contacts, which increases the driving force for diffusion between tungsten particles, enhancing grain growth.[25] It is possible that the higher applied pressure in the SPS samples helped to increase grain growth at 1500 ºC to a rate comparable to the grain growth rate of the HP samples at 1800 ºC. Alternatively, the spark plasma sintering process itself may enhance grain growth by an unknown mechanism. Future studies on grain growth in SPS are necessary to determine if such a mechanism exists.

The SPS tungsten samples produced at 1800 ºC do not appear to correlate well with the grain sizes reported by Pugh and Amra[105] or by Karpinos *et al*.[82] The SPS tungsten data at 1800 ºC appear to show that abnormal grain growth is occurring (as stated earlier in this section), whereas the pressureless sintered data and the hot pressed

data are nearly straight lines on the logarithmic time scale, which is expected in normal grain growth.[124]

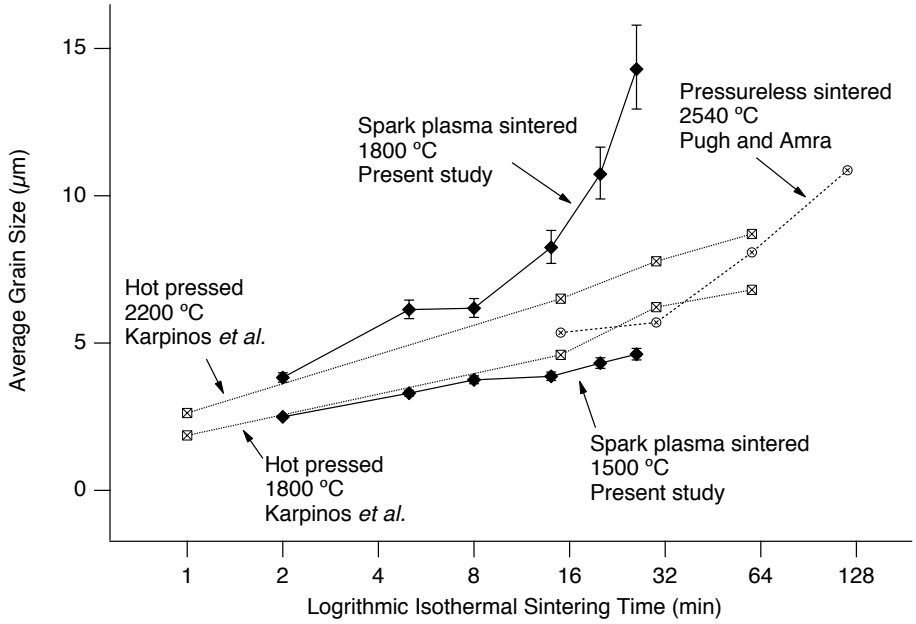

Figure 4.24. Comparison of the average grain sizes of pure tungsten spark plasma sintered at 1500 and 1800 ºC between 2 and 26 min to pressureless sintered tungsten and hot pressed tungsten. The SPS tungsten had an applied pressure of 64 MPa. The pressureless sintered data were taken from Pugh and Amra.[105] The hot pressed data were taken from Karpinos *et al.*,[82] and the samples were pressed with an applied pressure of 14.7 MPa. The error bars on the SPS tungsten grain sizes are based on a 95% confidence interval found using the Cox method.[119]

4.4.3. Relationship Between Grain Size and Density in Tungsten and Tungsten-Ceria

Gupta reported that in traditional sintering the density and grain size increase linearly with respect to one another during the initial and intermediate stages of sintering,

and in the final stage of sintering, grain growth becomes dominant.[126] To see if this relationship is true for spark plasma sintered tungsten and tungsten-ceria, the average tungsten grain sizes and final densities of SPS tungsten, W-1CeO_2, W-10CeO_2, or W-20CeO_2 were plotted, and the results are shown in Figure 4.25. At fractional densities above 0.85 (final stage sintering), the grain size-density trajectory of spark plasma sintered tungsten and W-1CeO_2 appears to remain nearly linear in character (Figure 4.25), in contrast to the study by Gupta.[126]

In the W-10CeO_2 and W-20CeO_2 samples, the tungsten grain size and density both increase; however, as shown in Figure 4.25, above about 0.94 fractional density, densification is dominant over grain growth. As discussed in Section 4.3.2, it is possible that the ceria begins to volatilize out of the compact, and the weight percent of ceria in the sintered compact could be lower than the original 10 or 20 wt% added to the tungsten. This would increase the theoretical density of the parts, as tungsten has a density of 19.25 g/cm^3 and ceria has a density of 7.13 g/cm^3. Because the weight percent of ceria might be lower in these samples, the fractional density would be higher. If the fractional density of the W-10CeO_2 and W-20CeO_2 compacts is actually lower than what is reported in this thesis, this may account for the perceived dominance in densification over grain growth above a fractional density of 0.94.

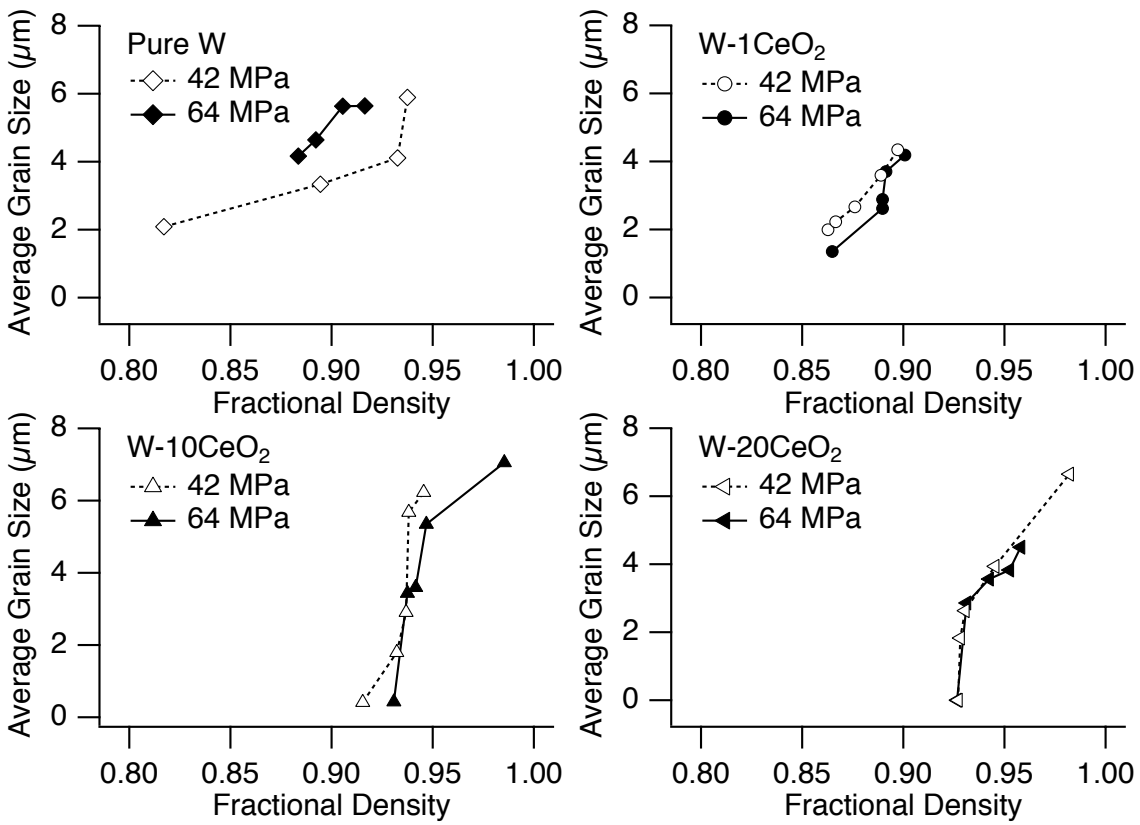

Figure 4.25. Comparison of the effects of applied pressure on the grain size-density trajectory of SPS tungsten, W-1CeO_2, W-10CeO_2, and W-20CeO_2 between 1300 and 1700 ºC. All samples were produced with a 2 min soak time. For clarity, the error bars on the grain sizes and fractional densities are not shown.

The average grain sizes and densities of pure tungsten spark plasma sintered between 1200 and 1800 ºC at an applied pressure of 64 MPa were compared with the average grain sizes and densities of pressureless sintered tungsten[99] and hot pressed tungsten.[82] These results are shown in Figure 4.26. The grain size-density trajectory of the SPS tungsten does not correlate at all with the pressureless sinted data from Vasilos and Smith[99]; however, the trajectory is similar between the SPS tungsten and the hot

pressed data from Karpinos *et al*.[82] (Figure 4.26). The primary difference between the SPS grain size-density trajectory and the HP grain-size trajectory is that for the same density, the average grain size of the SPS tungsten is smaller than the average grain size of the HP tungsten (Figure 4.26). This result is in agreement with published overviews of the spark plasma sintering, which claim that spark plasma sintering produces similar final densities as hot pressed parts, but with limited grain growth and at lower temperatures.[76]

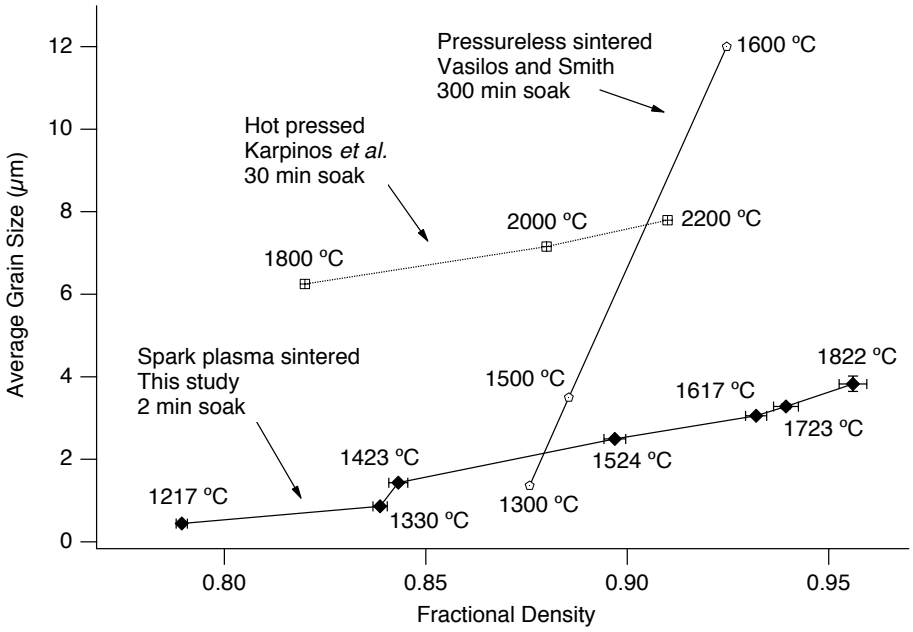

Figure 4.26. Comparison of the average grain sizes and densities of pure tungsten spark plasma sintered between 1200 and 1800 ºC to pressureless sintered tungsten and hot pressed tungsten. The SPS tungsten had an applied pressure of 64 MPa. The pressureless sintered data were taken from Vasilos and Smith.[99] The hot pressed data were taken from Karpinos *et al.*,[82] and the samples were pressed with an applied pressure of 14.7 MPa. The error bars on the SPS tungsten grain sizes are based on a 95% confidence interval found using the Cox method[119] and the error bars on the fractional densities are based on the measurement error described in Section 4.3.1. For the SPS samples produced between 1200 and 1700 ºC, the grain size distribution is small enough that the error bars are contained within the plot markers.

4.5. Hardness of SPS Tungsten and Tungsten-Ceria

The mechanical properties of sintered materials are important to understand in order to optimize the sintering process.[25] These properties, such as hardness, are dependent on the density, grain size, impurity content, and flaws in the microstructure.[25] In this thesis, the hardness of spark plasma sintered tungsten and tungsten-ceria samples was measured and compared to the density and the average grain size of the samples.

4.5.1. Estimated Error of Hardness Measurements

The machine error had previously been measured to be ±5 VHN, but repeated indents on the same material produced a larger spread that was about ±20 VHN. The error bars reported on the figures in this section are based on the high and low Vickers hardness measurements for each sample, and the plot markers are the average of six indents on each sample. The indents, such as the one in Figure 4.27, were measured optically across both diagonals.

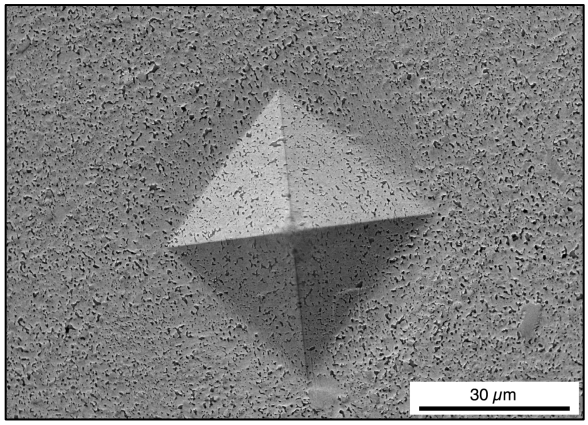

Figure 4.27. Example of pyramid-shaped indent. The indent was made with 1 kgf for 15 sec on a W-4CeO_2 sample that was spark plasma sintered at 1300 ºC with 64 MPa applied pressure and a 2 min soak time.

4.5.2. Effects of Pressure, Temperature and Time on Hardness of Tungsten and Tungsten-Ceria

Two applied pressures, 42 and 64 MPa, were used in this study to determine whether pressure has a significant effect on the final average hardness of SPS tungsten and SPS tungsten-ceria. Samples of pure tungsten, W-1CeO_2, W-10CeO_2, and W-20CeO_2 were spark plasma sintered at 1300, 1400, 1500, 1600, and 1700 ºC for 2 min with an applied pressure of 42 or 64 MPa (Figure 4.28). Pressure did not appear to affect the final hardness of pure tungsten, W-10CeO_2, or W-20CeO_2; however, there may have been a slight correlation between applied pressure and hardness in the W-1CeO_2 samples (Figure 4.28).

The higher applied pressure (64 MPa) on the W-1CeO_2 compacts appeared to produce harder samples than the lower applied pressure (42 MPa), as shown in Figure 4.28. Hardness is an indirect measure of the density and grain size in sintered compacts,[25] and compacts with high densities and small grain sizes should be harder than compacts with low densities and large grain sizes. Based on the similar densities of W-1CeO_2 (Figure 4.9) and the similar average grain sizes of W-1CeO_2 (Figure 4.16) spark plasma sintered with applied pressures of 42 MPa and 64 MPa, the hardness of the W-1CeO_2 samples should likewise be similar. The seemingly significant difference in the hardness between the 42 MPa samples and the 64 MPa samples may be due to an error in the measurement of hardness that has not been taken into account. This error could possibly include variation in the distance between microindenter and each sample, or the variation in optical hardness measurement made by the researcher.

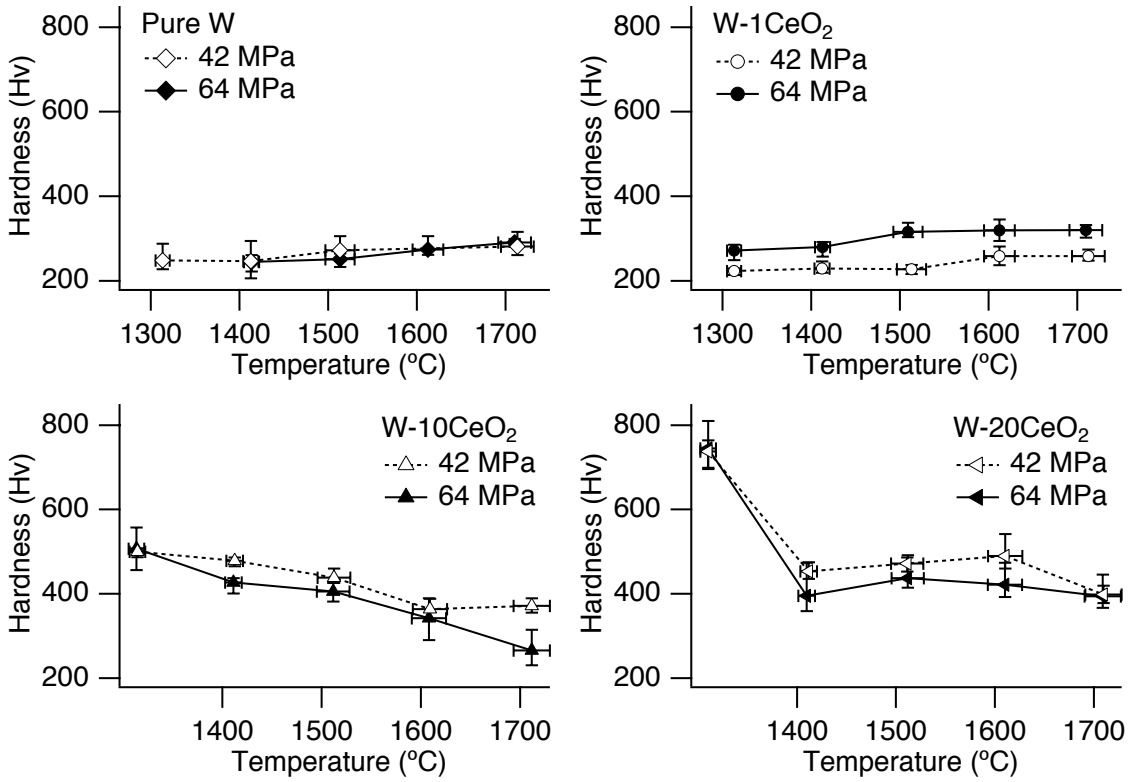

Figure 4.28. Comparison of the effects of applied pressure on the Vickers hardness of SPS tungsten, W-1CeO_2, W-10CeO_2, and W-20CeO_2 between 1300 and 1700 ºC. All samples were produced with a 2 min soak time. The error bars on the hardness are based on the high and low values of the measurements, and the error bars on the temperatures are based on the accuracy range of the infrared thermometer.

Whereas the hardness of the pure tungsten samples and the W-1CeO_2 samples increased with increasing temperature, the hardness of the W-10CeO_2 samples and the W-20CeO_2 samples decreased with increasing temperature (Figure 4.28). This decrease in hardness with increasing temperature may be due to a reduction in density, an increase in tungsten grain size, or the formation of flaws during spark plasma sintering. Direct

comparisons between the hardness and the density, and the hardness and the grain size, are necessary to determine why the hardness decreases in the W-10CeO_2 and W-20CeO_2 samples. These comparisons are made in Section 4.5.3.

To determine if the trend toward increasing hardness of the pure tungsten and decreasing hardness of W-10CeO_2 held true for all spark plasma sintering temperatures studied, the hardness of pure tungsten and the hardness of W-10CeO_2 were plotted as functions of temperature between 900 and 1800 ºC (Figure 4.29). In Figure 4.29, the overall trend in hardness of pure tungsten is shown to increase across the entire temperature range. The apparent discontinuity in this trend at 1400 ºC may be a real effect during sintering; however, due to the wide range of hardnesses measured in each sample, no statistically relevant trends are present. The W-10CeO_2 hardnesses shown in Figure 4.29 increase between 900 and 1300 ºC, but there is a steep decline in the hardness as the temperature is raised above 1300 ºC. The drop in hardness is the same as seen in Figure 4.28, and the cause of this drop cannot be determined from the hardness relationship with sintering temperature, and the hardnesses of these samples must be compared with the densities and grain sizes of the samples. These comparisons are made in Section 4.5.3.

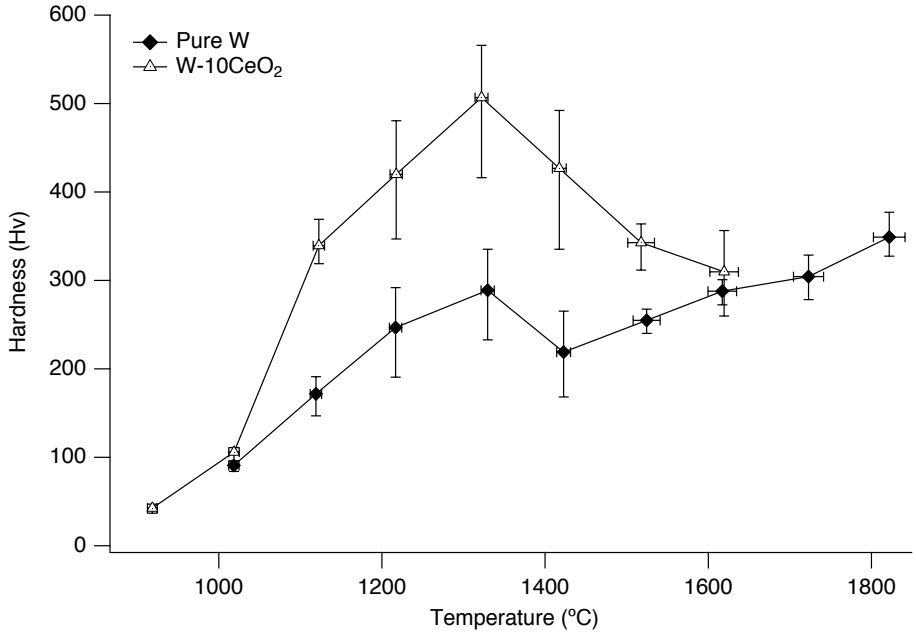

Figure 4.29. Vickers hardness of pure tungsten and W-10CeO_2 spark plasma sintered between 900 and 1800 ºC. All samples were sintered at an applied pressure of 64 MPa and soaked for 2 min at maximum temperature. The error bars on the hardness are based on the high and low hardness measurements for each sample, and the error bars on the temperatures are based on the accuracy range of the infrared thermometer.

Hardness data in the open literature for sintering tungsten are limited. Pugh and Amra[105] studied the hardness of tungsten in compacts isothermally sintered at 2540 and 3100 ºC between 15 and 120 min. The results of Pugh and Amra[105] were compared to the hardness measured in pure tungsten spark plasma sintered at 1500 and 1800 ºC between 2 and 26 min (Figure 4.30). Based on the comparison in Figure 4.30, all of the samples spark plasma sintered at 1500 and 1800 ºC have higher hardness values than the samples produced by Pugh and Amra[105] at 2450 ºC. This difference may be explained by a higher density of the parts in SPS tungsten, a smaller grain size in SPS tungsten, or a

combination of these factors. In the samples sintered by Pugh and Amra,[105] the fractional densities are between 0.780 and 0.910, and the average grain sizes between 5.1 and 10.6 μm. In contrast to the pressureless sintered samples, the SPS tungsten samples sintered at 1500 ºC had fractional densities between 0.892 and 0.902 and the average grain sizes were between 2.5 and 4.6 μm. Because the SPS samples have higher densities and smaller average grain sizes than the samples sintered by Pugh and Amra,[105] it is not possible to discern which of these properties, density or grain size, resulted in the higher hardness values of the spark plasma sintered samples. When compared with the samples sintered at 3100 ºC by Pugh and Amra,[105] the samples spark plasma sintered at 1500 ºC had similar hardness values, and the samples spark plasma sintered at 1800 ºC had higher hardness values. In the samples sintered by Pugh and Amra[105] at 3100 ºC, the fractional densities are between 0.945 and 0.970, which is similar to the fractional densities of the tungsten spark plasma sintered at 1800 ºC (between 0.957 and 0.977). At these similar densities, it would be expected that the hardness values would also be similar. The higher hardness values in the SPS tungsten samples relative to the pressureless sintered tungsten samples are likely due to the smaller grain sizes in the SPS tungsten than in the pressureless sintered tungsten. The average grain sizes for the SPS tungsten samples were between 3.8 and 14.3 μm and the average grain sizes in the pressureless sintered tungsten samples were between 43.0 and 80.1 μm.

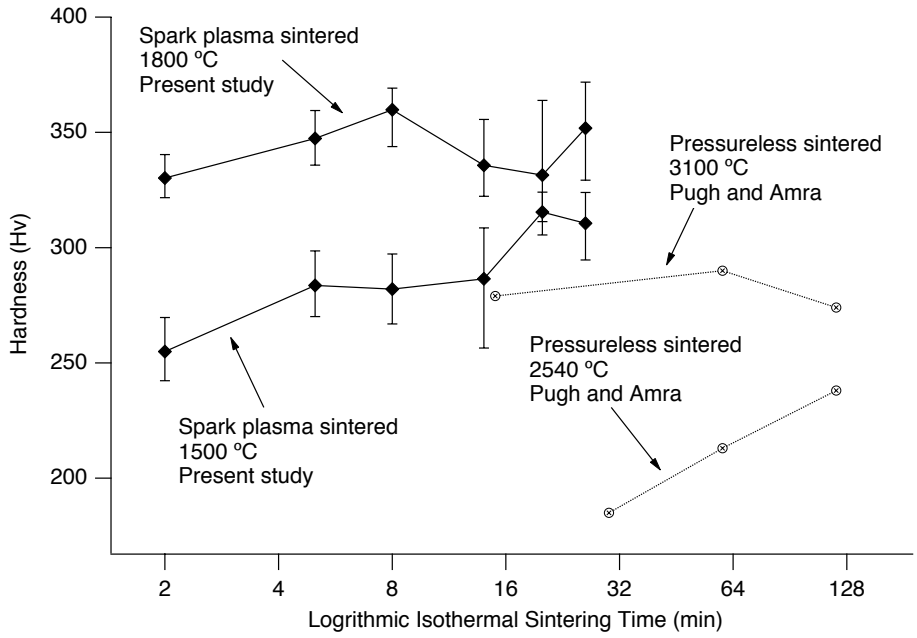

Figure 4.30. Comparison of the Vickers hardness of pure tungsten spark plasma sintered at 1500 and 1800 ºC between 2 and 26 min to pressureless sintered tungsten at 2540 and 3100 ºC between 15 and 120 min. The SPS tungsten had an applied pressure of 64 MPa. The pressureless sintered data were taken from Pugh and Amra.[105]

4.5.3. Relationship Between Hardness and Density and Relationship Between Hardness and Grain Size in Tungsten and Tungsten-Ceria

Hardness is a function of density, grain size, and flaws in the microstructure. In sintering, as the density increases, the pore area is decreased, which leads to higher hardness values.[25] In addition to densification, the grains in the sintering compact are growing, and as the grains coarsen, the hardness is decreased.[124] Comparing the relationships between hardness and density, and hardness and grain size, an attempt has been made to determine whether density or grain size has the greater influence on the hardness.

The hardness was plotted as a function of density (Figure 4.31) and as a function of grain size (Figure 4.32) for samples of pure tungsten, W-1CeO_2, W-10CeO_2, and W-20CeO_2. As shown in Figure 4.31, the hardness increased as the density increased in the pure tungsten and the W-1CeO_2 samples. However, there does not appear to be a strong correlation between the hardness and grain size in the pure tungsten or W-1CeO_2 samples, as shown in Figure 4.32. Based on these relationships for the pure tungsten samples and the W-1CeO_2 samples, density appears to have the greater influence on hardness than does grain size.

The hardness decreased as the density increased in the W-10CeO_2 and W-20CeO_2 samples (Figure 4.31), which is initially counterintuitive. This decrease in hardness with increasing density may be the result of the grain size having a larger influence on the hardness than the density on these samples. This hypothesis is supported by the results shown in Figure 4.32, where the hardness decreases as the grain size increases in the W-10CeO_2 and W-20CeO_2 samples.

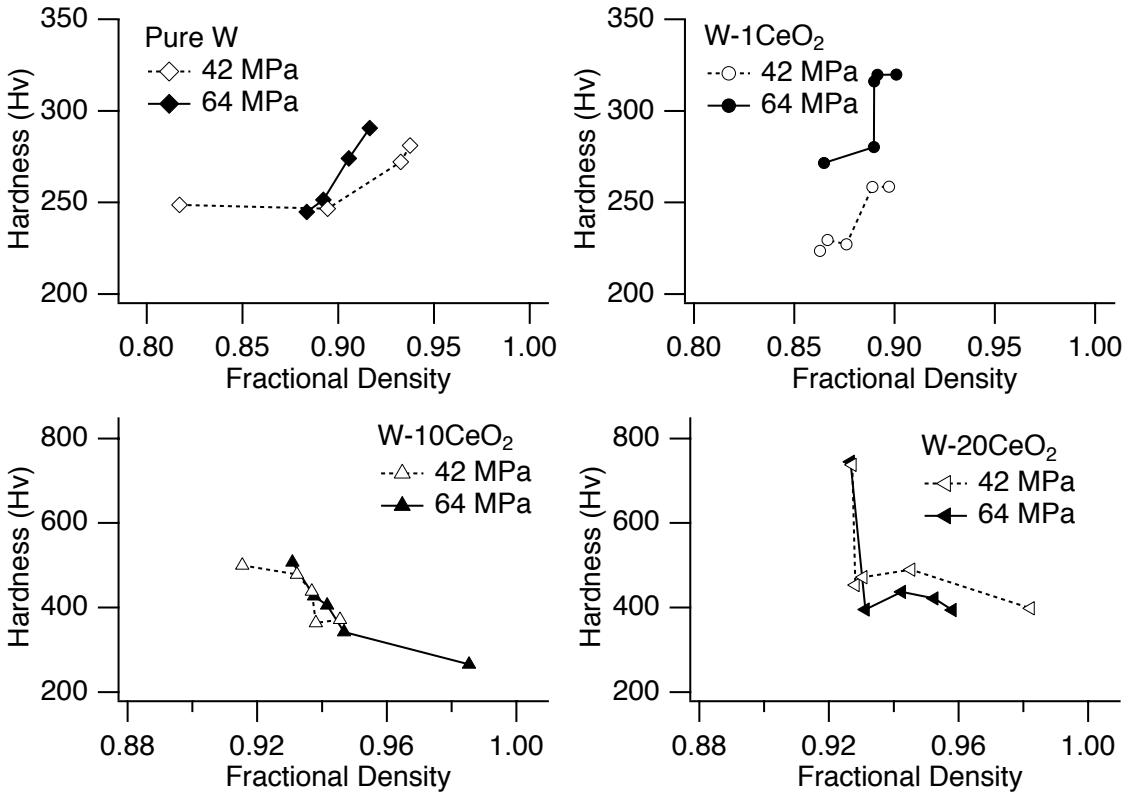

Figure 4.31. Comparison of the effects of the density on the hardness of SPS tungsten, W-1CeO_2, W-10CeO_2, and W-20CeO_2 between 1300 and 1700 ºC. All samples were produced with a 2 min soak time. For clarity, the error bars on the densities and hardnesses are not shown.

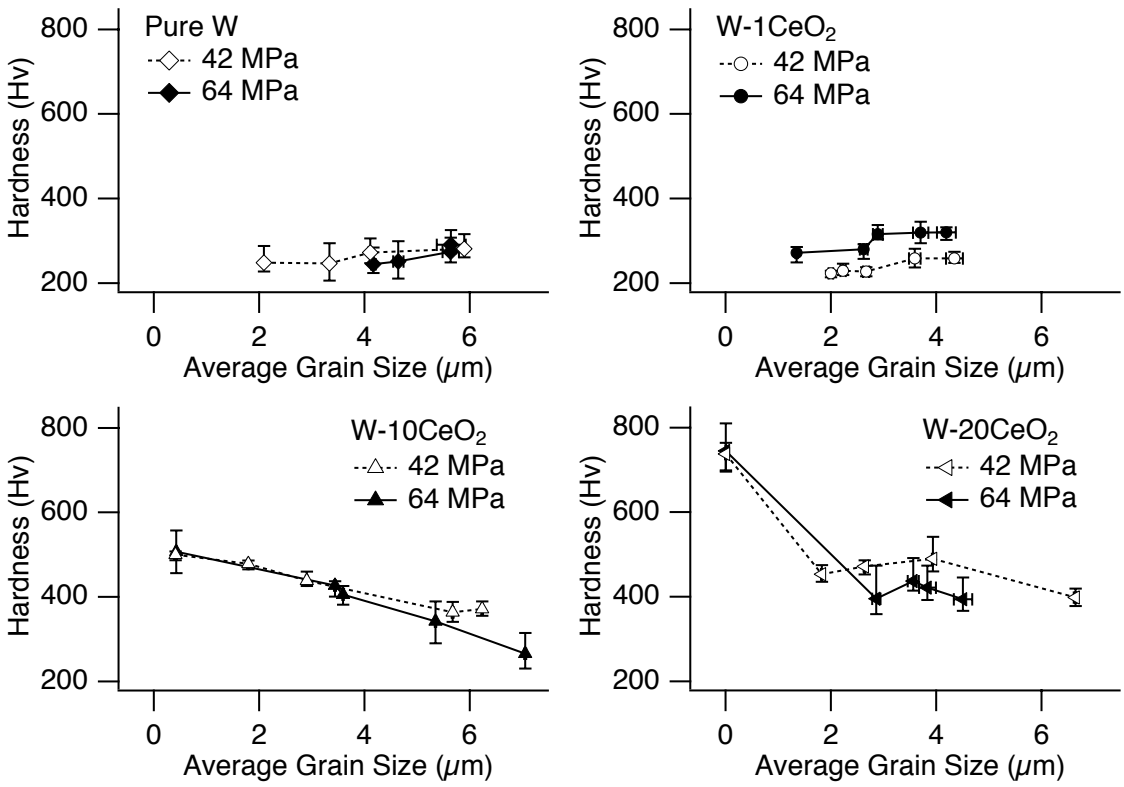

Figure 4.32. Comparison of the effects of tungsten grain size on the hardness of SPS tungsten, W-1CeO_2, W-10CeO_2, and W-20CeO_2 between 1300 and 1700 ºC. All samples were produced with a 2 min soak time. The error bars on the hardness are based on the high and low values of the measurements, and the error bars on the average grain sizes are based on a 95% confidence interval found using the Cox method.[119]

The reduction in hardness in the W-10CeO_2 and W-10CeO_2 samples may also be the result of flaws in the microstructure. Discontinuities in the microstructure, such as fractures, cause an uneven distribution of stress, and these stresses will be concentrated near the discontinuities.[127] When an external stress is applied near these stress concentrations, the material will fail at a lower stress than a material that does not contain discontinuities in the microstructure.[127] Cracks in the ceria phase were observed in the microstructures of the W-10CeO_2 and W-20CeO_2 samples, and examples of these fractures are shown in Figure 4.33. These cracks may have concentrated the stress applied during microhardness testing, which may have resulted in the W-10CeO_2 and W-20CeO_2 samples yielding at a lower stress than they would have if they were fracture free.

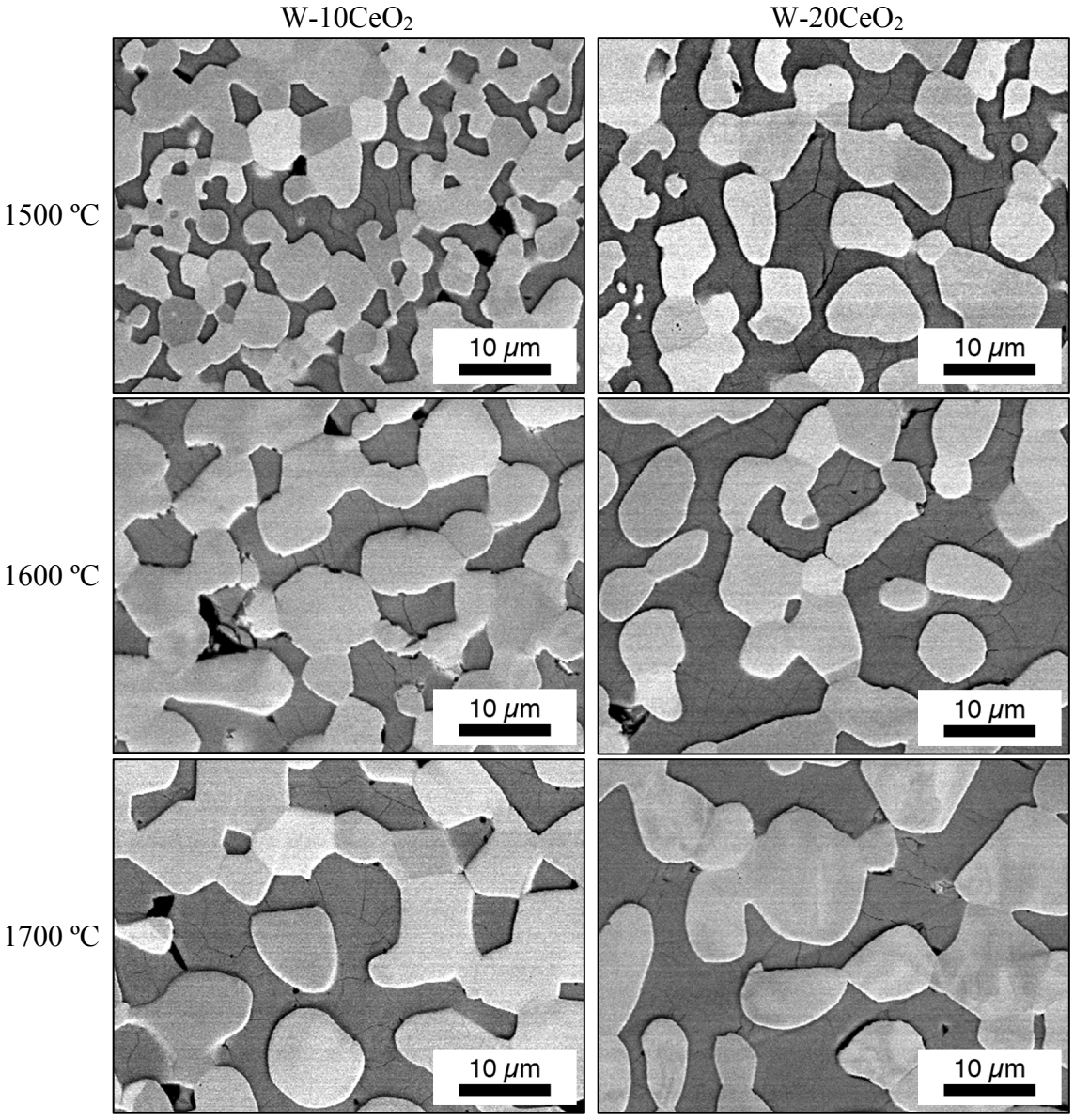

Figure 4.33. Examples of fractures in the microstructures of SPS W-$10CeO_2$ and W-$20CeO_2$ spark plasma sintered at 1500, 1600, and 1700 ºC. All samples had an applied pressure of 64 MPa and were soaked at maximum temperature for 2 min. The lighter phase is tungsten and the darker phase is ceria.

In Figure 4.33, the fractures are only present in the ceria phase. Two possible causes for the fractures in the ceria phase are due to the mismatch in the coefficient of thermal expansion between the ceria and tungsten[128] or thermal shock during heating and/or cooling of the samples.[129] The thermal expansion data on ceria in the open literature is limited; however, the linear coefficient of thermal expansion has been measured by Sata and Yoshimura at 1100 ºC.[130] At 1100 ºC, the linear coefficient of thermal expansion in ceria is about 13.5×10^{-6} K^{-1},[130] and the linear coefficient of thermal expansion in tungsten is about 5.13×10^{-6} K^{-1}.[18] This difference in the linear coefficient of thermal expansion may have caused stresses to build up at the tungsten-ceria interfaces during heating and/or cooling of the samples in SPS.[128] Because ceria is a ceramic, these stresses cannot be distributed through the phase by plastic deformation, and the stresses will be relieved by the formation of fractures.[128]

Due to the brittle nature of ceramics, during rapid heating or rapid cooling, thermal stresses that build up in the ceramic can cause the parts to fracture. In spark plasma sintering of tungsten-ceria, the samples were heated between 40 and 100 ºC/min, which might have caused a build up of thermal stresses in the ceria phase, leading to the fractures seen in Figure 4.33. At the end of the spark plasma sintering soaks, the current was immediately shut off, and the samples were allowed to cool *in situ.* The water-cooled hydraulic rams on the SPS unit acted as heat sinks, and the samples were cooled to room temperature rapidly. For example, the tungsten-ceria samples were cooled from 1600 ºC to room temperature in 8 min, which may have caused the thermal stresses to fracture the ceria phase. In addition to the rapid cooling, Coble and Kingery showed that the resistance to thermal shock decreases with increasing porosity in a ceramic phase,[131]

and the presence of pores in the ceria phase at higher spark plasma sintering temperatures (discussed in Section 4.6) may have aided in the fracturing of the ceria. More experiments are necessary to determine the cause of these fractures in the ceria phase.

4.6. Possible Reduction of Ceria During Spark Plasma Sintering

During spark plasma sintering of tungsten-ceria powders above 1600 ºC, sparks were visually observed coming from between the die and punch. Upon cooling and removal from the SPS unit, the top and bottom of the die body had become discolored and were covered with an ochre-colored powder (Figure 4.34).

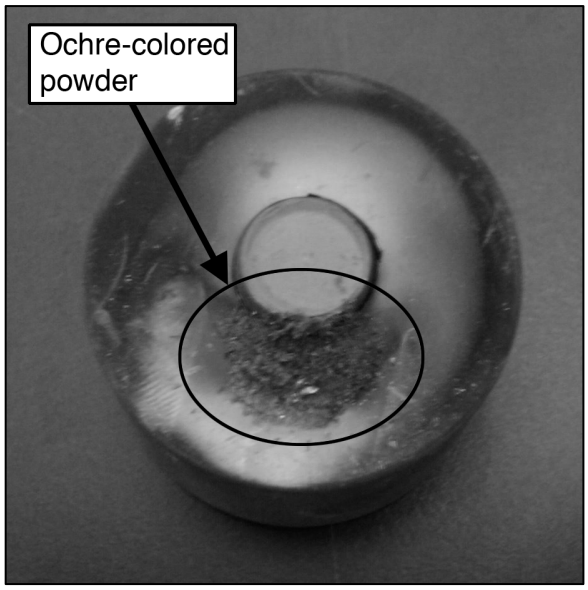

Figure 4.34. Example of ochre-colored powder found on a die after spark plasma sintering above 1600 ºC. During processing of ceria-bearing powders, a yellow-brownish powder was deposited on the die at the die-punch interface. The sample shown is W-20CeO_2 processed with 42 MPa at 1700 ºC for 2 min.

When ceria is reduced from CeO_2 to Ce_2O_3, the color changes from white to yellow,[130] which matches with the powder observed on the die. Reactions of Ce_2O_3 and WO_3 powders form a brown powder,[132] which may also have been present in the powder at the die-punch interface. This leads to two possible reactions occurring during spark plasma sintering of tungsten-ceria powders: (1) decomposition of CeO_2 to Ce_2O_3 and oxygen gas or (2) a reduction-oxidation reaction of CeO_2 and tungsten to Ce_2O_3 and WO_x. It is also possible that both reactions are occurring during SPS.

To confirm the plausibility of either of these reactions in the tungsten-ceria system, the reduction of CeO_2 to Ce_2O_3 had to occur. To determine the oxidation state of the cerium ion (4+ for CeO_2 and 3+ for Ce_2O_3), X-ray photoelectron spectroscopy was performed on W-15CeO_2 samples produced between 1300 and 1700 ºC with an applied pressure of 42 MPa. The 3d peak energies for Ce^{3+} and Ce^{4+} were compared to the XPS energy spectra obtained from the W-15CeO_2 samples, and the results are shown in Figure 4.35. Qualitatively, the energy peaks in all of the samples were closer to the Ce^{3+} energies than the Ce^{4+} energies, which would indicate that the ceria phase in the SPS tungsten-ceria parts is at least partially Ce_2O_3. Based on this analysis, it is possible that CeO_2 is decomposing or that CeO_2 is reacting with the tungsten phase.

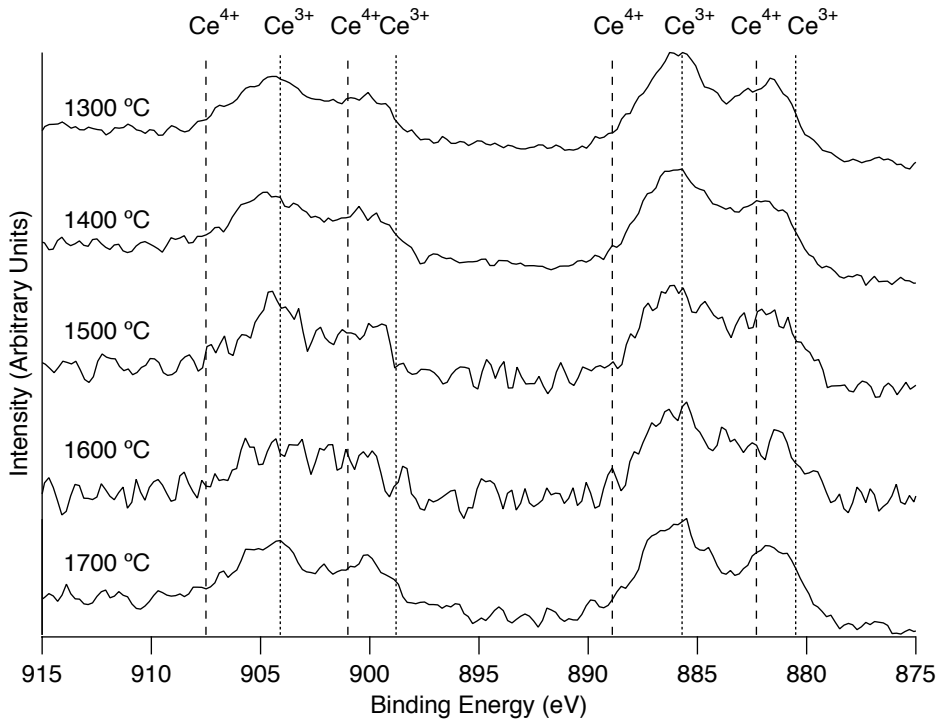

Figure 4.35. X-ray photoelectron energy spectra for W-15CeO_2 samples spark plasma sintered between 1300 and 1700 ºC with an applied pressure of 42 MPa. The binding energies for Ce^{3+} and Ce^{4+} are shown by the dotted lines.

If either of the possible ceria reactions occurred during SPS, the phase fraction of ceria in the samples would be decreased at higher sintering temperatures. To determine if the phase fraction of ceria was reduced during SPS, the area fraction of ceria was measured from backscatter electron images of W-10CeO_2, W-15CeO_2, and W-20CeO_2 produced between 1400 and 1700 ºC at 42 MPa applied pressure (Figure 4.36). Based on the results shown in Figure 4.36, between 1400 and 1600 ºC, the ceria area fraction in the W-10CeO_2 does not change, nor does it change in the W-15CeO_2 samples. Although it is difficult to ascertain from Figure 4.36, there is a statistically significant drop in the ceria area fraction in the W-10CeO_2 and W-15CeO_2 samples between 1600 and 1700 ºC. In

the W-10CeO_2 samples, the ceria area fraction drops from 0.22±0.02 at 1600 ºC to 0.18±0.02 at 1700 ºC, and in the W-15CeO_2 samples, the ceria area fraction drops from 0.27±0.01 at 1600 ºC to 0.24±0.01 at 1700 ºC. The change in ceria area fraction is more pronounced in the W-20CeO_2 samples, and the ceria area fraction drops from 0.42±0.01 at 1600 ºC to 0.30±0.02 at 1700 ºC. Based on the results shown in Figure 4.36, the decomposition of CeO_2 or the reaction of tungsten with CeO_2 is accelerated between 1600 and 1700 ºC.

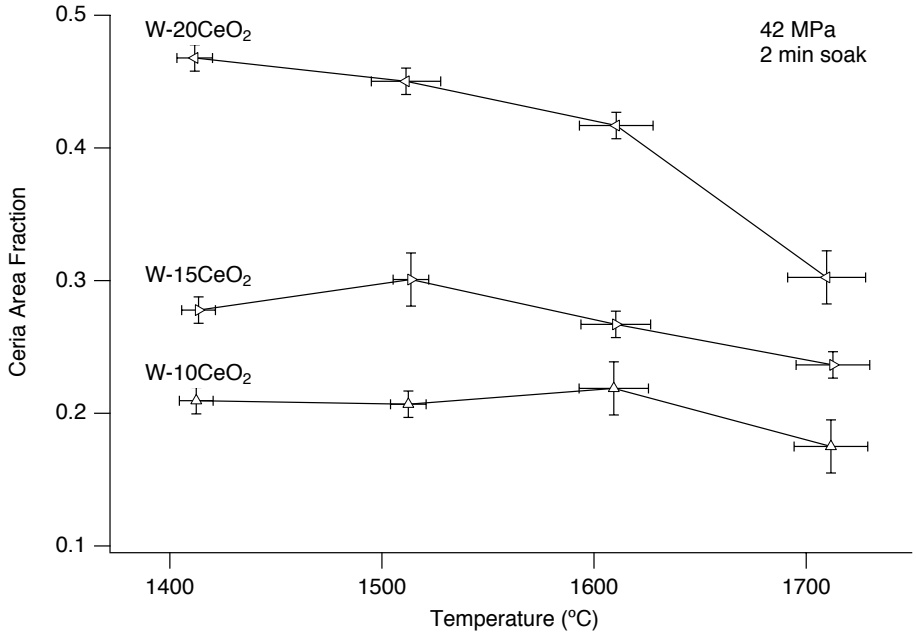

Figure 4.36. Ceria area fraction in W-10CeO_2, W-15CeO_2, and W-20CeO_2 spark plasma sintered between 1400 and 1700 ºC with 42 MPa applied pressure. The error bars on the ceria area fraction are based on the spread of area fractions measured 3 times on each image, and the error bars on the temperatures are based on the accuracy range of the infrared thermometer.

The reduction of ceria area fraction between 1600 and 1700 ºC in the W-10CeO_2, W-15CeO_2, and W-20CeO_2 samples does not indicate if the ceria is decomposing to Ce_2O_3 and oxygen gas, or if the ceria is reacting with the tungsten. The backscatter electron images of the W-4CeO_2, W-10CeO_2, W-15CeO_2, and W-20CeO_2 samples produced at 1700 ºC with an applied pressure of 42 MPa show that the pores are predominantly contained within the ceria phase (Figure 4.37). This lends credence to the hypothesis that the ceria is decomposing to Ce_2O_3 and oxygen gas. If the ceria were reacting with the tungsten, the pores would be expected to extend into the tungsten phase as well. In the backscatter electron images shown in Figure 4.37, there is no indication that another phase, composed of WO_x, is present. If WO_x were forming at the tungsten-ceria interface, a phase slightly darker than the tungsten phase would be present on the perimeter of the tungsten grains.

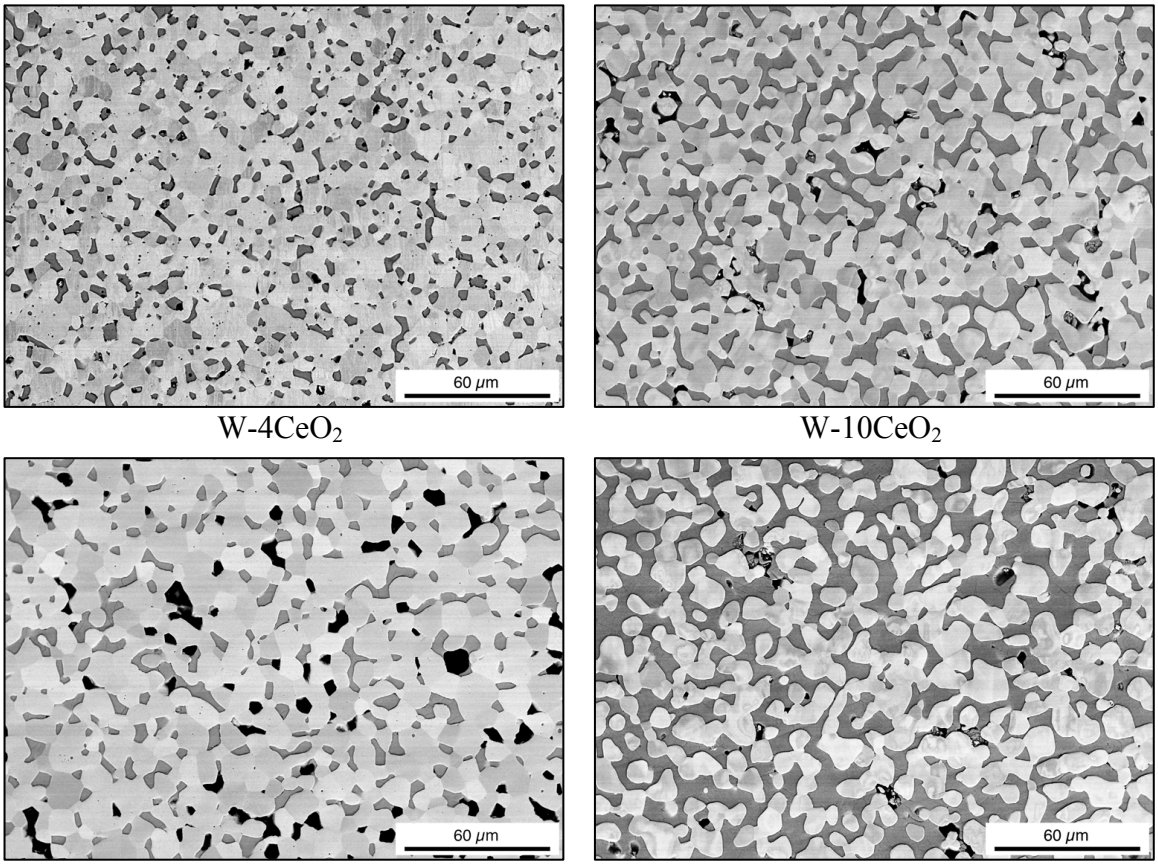

W-4CeO_2 W-10CeO_2

W-15CeO_2 W-20CeO_2

Figure 4.37. Backscatter electron images of W-4CeO_2, W-10CeO_2, W-15CeO_2, and W-20CeO_2 spark plasma sintered at 1700 ºC with an applied pressure of 42 MPa. The lightest phase is tungsten, the darker phase is ceria, and the darkest phase is pores.

The formation of pores during sintering of CeO_2 is not unprecedented. Zhou[133] reported that during sintering of 14.2 nm CeO_2, the maximum density was reached at about 1200 ºC, and above this temperature, the density decreased due to pores forming from the evolution of oxygen gas. The initial particle size of the ceria powders used in the present study was 25 nm, so it is likely that the pores formed in the ceria phase during SPS were also formed by the evolution of oxygen gas.

Based on the decrease in the ceria phase fraction, shown in Figure 4.36, and the presence of pores in the ceria phase, shown in Figure 4.37, the most likely reaction occurring during spark plasma sintering of tungsten-ceria is a decomposition of CeO_2 to Ce_2O_3 and oxygen gas. From a thermodynamic perspective, the decomposition of CeO_2 to Ce_2O_3 and oxygen gas is more energetically favorable than the reduction-oxidation reaction between CeO_2 and tungsten. This is based on a comparison of the Gibbs free energy of formation of CeO_2 and the Gibbs free energy of formation of WO_2 and WO_3 shown in the Ellingham-Richardson diagram in Figure 4.38. If oxygen were to react with Ce_2O_3 or tungsten, it is thermodynamically favorable to form CeO_2 rather than WO_2 or WO_3. Based on the Ellingham-Richardson diagram in Figure 4.38, if tungsten oxides did form during spark plasma sintering, it would be energetically favorable for the Ce_2O_3 phase to react with these tungsten oxides to form CeO_2 and pure tungsten.

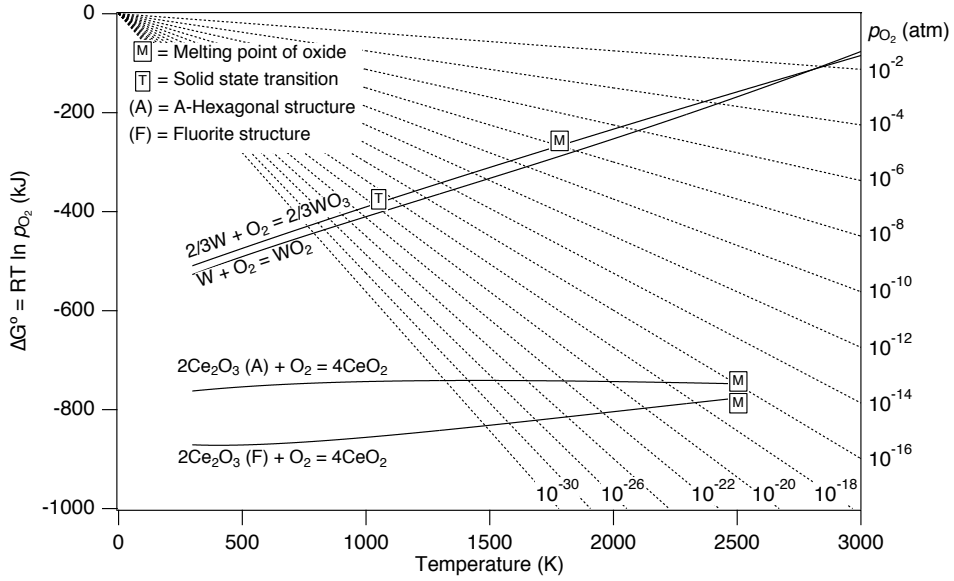

Figure 4.38. Ellingham-Richardson diagram for CeO_2, Ce_2O_3, WO_2, and WO_3. All reactions are standardized to one mole of O_2. (Thermodynamic data from Chase *et al.*[134] and Zinkevich *et al.*[23])

The ochre-colored powder observed at the die-punch interface after spark plasma sintering at 1700 ºC (Figure 4.34) is most likely Ce_2O_3 that formed during SPS. Some Ce_2O_3 probably adsorbed to the oxygen gas that formed during SPS, and this is how the Ce_2O_3 was transported out of the die during sintering. Further study is required to confirm this hypothesis. Future studies should include an analysis of the gas composition in the chamber during SPS, and an analysis of the chemical composition of the powders present on the die after SPS.

4.7. Densification Kinetics of SPS Tungsten

4.7.1. Plastic Flow as a Densification Mechanism in SPS Tungsten

For plastic flow to occur, the pressure at the particle contacts (the effective pressure) must exceed the yield strength of the material.[37] As the temperature of the material is increased, the yield strength decreases, and less pressure is required to densify a material by plastic flow.[37] To determine if plastic flow is the dominant densification mechanism for SPS tungsten, the effective pressures of SPS tungsten sintered between 800 and 1800 ºC for 2 min at an applied pressure of 64 MPa were compared with the temperature-dependent yield strength for tungsten. The effective pressures for SPS tungsten were found using Equation 2.7, and these data were compared to the temperature-dependent yield strength of 95% dense tungsten reported by Barth and McIntire (Figure 4.39).[104]

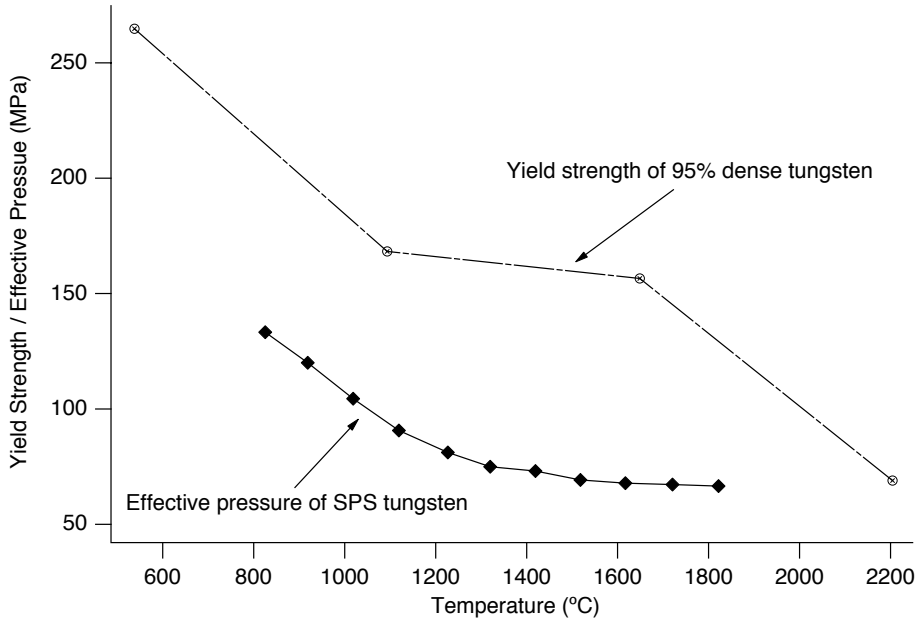

Figure 4.39. Comparison of the effective pressures of pure tungsten spark plasma sintered between 800 and 1800 ºC and the yield strength of 95% dense tungsten. The yield strength data were taken from Barth and McIntire.[104] The effective pressures do not exceed the yield strength, which indicates densification of SPS tungsten did not occur by plastic flow.

Based on the comparison of the yield strength of tungsten to the effective pressures of SPS tungsten in Figure 4.39, the effective pressures never exceeded the temperature-dependent yield strength. Because the yield strength was not exceeded during SPS, the SPS tungsten parts produced between 800 and 1800 ºC were likely not densified by plastic flow.

4.7.2. Hot Press Models for Densification Kinetics Applied to SPS Tungsten

With regard to sintering methods, hot pressing is arguably the closest analog to spark plasma sintering. As such, it was assumed that the densification models for hot pressing are also valid for spark plasma sintering. In this section, the SPS data for pure tungsten were applied to the models for lattice diffusion-controlled densification (Equation 2.14), boundary diffusion-controlled densification (Equation 2.15), and power-law creep controlled densification (Equation 2.16). The diffusivities, rate constants, and apparent activation energies found using these models were compared to values in the literature. Based on this comparison, the possible rate-limiting mechanism in densification of SPS tungsten is proposed.

In order to calculate the diffusion coefficients at a given temperature, density, and grain size, the models given in Equations 2.14, 2.15, and 2.16 were solved for the diffusion coefficients:

$$D_v = \frac{3}{40}\frac{G^2 kT}{a_o{}^3 \rho}\frac{d\rho}{dt}\left(\frac{P_A}{\rho} + c\frac{\gamma}{r}\right)^{-1} \qquad 4.3$$

$$D_b = \frac{1}{X}\frac{G^3 kT}{a_o{}^3 \rho}\frac{d\rho}{dt}\left(\frac{P_A}{\rho} + c\frac{\gamma}{r}\right)^{-1} \qquad 4.4$$

$$D_v = \frac{1}{A^*}\frac{kT}{\mu(T)\rho b}\frac{d\rho}{dt}\left(\frac{P_A}{\mu(T)\rho}\right)^{-n} \qquad 4.5$$

where Equation 4.3 is the model for lattice diffusion in hot pressing, Equation 4.4 is the model for boundary diffusion in hot pressing, and Equation 4.5 is the model for densification by power-law creep. The temperature-dependent shear modulus, $\mu(T)$, is defined in Equation 2.17, and is restated here[44]:

$$\mu(T) = \mu_o\left(1 + \frac{(T - 300)}{T_m}\frac{T_m}{\mu_o}\frac{d\mu}{dT}\right) \qquad 4.6$$

A summary of the symbol definitions in Equations 4.3-4.6 is given in Table 4.1.

Table 4.1. Definitions of variables in Equations 4.3-4.6.

Symbol	Definition	Symbol	Definition
D_v	Lattice diffusion coefficient	b	Burgers vector
D_b	Boundary diffusion coefficient	$d\rho/dt$	Densification rate
X	Geometric term	P_A	Applied pressure
A^*	Dorn parameter for shear stress	c	Geometric term
n	Power-law creep exponent	γ	Surface energy
G	Average grain size	r	Average pore radius
k	Boltzmann constant	μ_o	Shear modulus at 300 K
T	Absolute temperature	T_m	Melting temperature
a_o^3	Atomic volume	$(T_m/\mu_o)(d\mu/dt)$	Temperature dependence of shear modulus
ρ	Density		

The Dorn parameter for shear stress, A^*, in Table 4.1 is converted from the Dorn parameter measured for tensile stress, A, by multiplying A by $3^{(1-n)/2}$. The geometric term X is equal to 95/2 in intermediate stage sintering and 15/2 in final stage sintering.[40] The geometric term c is equal to 1 in intermediate stage sintering and 2 in final stage sintering.[40]

To apply the SPS tungsten data to the models in Equations 4.3, 4.4, and 4.5, the densification rate and the average pore radius had to be known for each sample. To find the densification rate, it was first necessary to construct a plot of the fractional densities of SPS tungsten as a function of sintering time. To do this, the fractional densities of tungsten spark plasma sintered between 800 and 1800 ºC and soaked for 2 min at maximum temperature were converted from functions of sintering temperature to functions of sintering time. The sample produced at 800 ºC was used as the baseline, and the sintering time was set to zero. Because the samples were heated at a constant rate of

100 ºC/min, the sintering time between 800 and 900 ºC is 1 min (60 s), the sintering time between 800 and 1000 ºC is 2 min (120 s), and so on. The fractional densities as a function of sintering time are plotted in Figure 4.40.

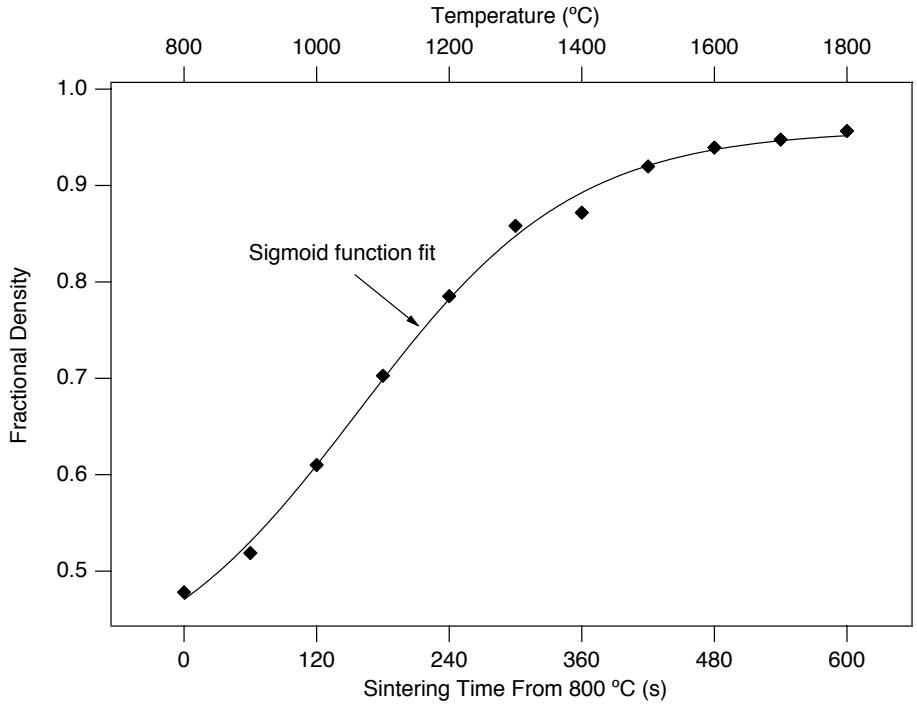

Figure 4.40. Fractional density as a function of sintering time for samples produced between 800 and 1800 ºC.

The density as a function of sintering time was estimated by fitting a sigmoid function to the data in Figure 4.40. Although this is an empirical approach to finding the density as a function of sintering time, sigmoid curves are commonly used to estimate the instantaneous density in master sintering curve calculations.[135-137] The sigmoid function fitted to the data was:

$$\rho(t) = a + \frac{b}{1 + \exp\left(\frac{c - t}{d}\right)} \qquad 4.7$$

where $\rho(t)$ is the instantaneous density at time t, and a, b, c, and d are fitting parameters.[137] The values of the fitting parameters for the densities shown in Figure 4.40 were solved using Mathematica,[116] and the best-fits were found to be $a = 0.3738$, $b = 0.5841$, $c = 157.8$, and $d = 97.60$. To estimate the densification rate, $d\rho/dt$, of the samples shown in Figure 4.40, Equation 4.7 was differentiated with respect to time:

$$\frac{d\rho}{dt} = \frac{b}{d}\frac{\exp\left(\frac{c-t}{d}\right)}{\left(1+\exp\left(\frac{c-t}{d}\right)\right)^2} \qquad 4.8$$

and the values of b, c, and d listed above were substituted into Equation 4.8.

In addition to the densification rate, the average pore radius of each sample had to be known in order to use Equations 4.3 and 4.4. The average pore radius for each sample sintered between 1000 and 1800 ºC was estimated using backscatter electron images. A routine was written in Mathematica[116] to estimate the average pore sizes in each backscatter electron image. The pores were assumed to be roughly spherical and uniform in size, and the average pore radius for each sample was estimated from the average pore size. The pore structure of the samples sintered at 800 and 900 ºC were completely interconnected, and individual pores could not be distinguished from one another. Because these pores were interconnected, the average pore radii could not be estimated for the samples sintered at 800 and 900 ºC.

The diffusivities for the lattice diffusion model (Equation 4.3), the boundary diffusion model (Equation 4.4), and the power-law creep model (Equation 4.5) were calculated using the measured values shown in Table 4.2 and the physical properties of tungsten shown in Table 4.3. The pressure term, P_A, was a constant 64 MPa for all

experiments. The calculated diffusivities were then plotted as functions of reciprocal temperature, and the results are shown in Figures 4.41, 4.42, and 4.44.

Table 4.2. Experimentally measured values for pure tungsten spark plasma sintered between 800 and 1800 ºC. The samples were produced with an applied pressure of 64 MPa, and the samples were soaked at maximum temperature for 2 min.

Temperature (ºC)	Average grain size (μm)	Fractional density	Densification rate (s^{-1})	Average pore radius (μm)
825	-	0.478	8.27×10^{-4}	-
922	-	0.519	1.18×10^{-3}	-
1018	0.29	0.611	1.44×10^{-3}	0.3
1119	0.31	0.703	1.48×10^{-3}	0.3
1227	0.41	0.785	1.26×10^{-3}	0.3
1325	0.86	0.858	9.17×10^{-4}	0.3
1419	1.43	0.872	5.95×10^{-4}	0.3
1518	2.49	0.910	3.57×10^{-4}	0.4
1617	3.06	0.939	2.05×10^{-4}	0.6
1721	3.28	0.948	1.15×10^{-4}	0.4
1822	3.83	0.957	6.31×10^{-5}	0.4

Table 4.3. Physical properties of tungsten used in the hot press models defined in Equations 4.3-4.5.

Property	Symbol	Value	Source
Atomic volume	a_o^3	1.59×10^{-29} m^3	Ashby[45]
Burgers vector	b	2.74×10^{-10} m	Ashby[45]
Surface energy	γ	2.8 J/m^2	German[25]
Melting temperature	T_m	3683 K	German[25]
Shear modulus at 300K	μ_o	1.60×10^5 MPa	Frost and Ashby[44]
Temperature dependence of modulus	$(T_m/\mu_o)(d\mu/dT)$	-0.38	Frost and Ashby[44]
Power-law creep exponent	n	4.7	Frost and Ashby[44]
Dorn constant	A	1.1×10^8	Frost and Ashby[44]

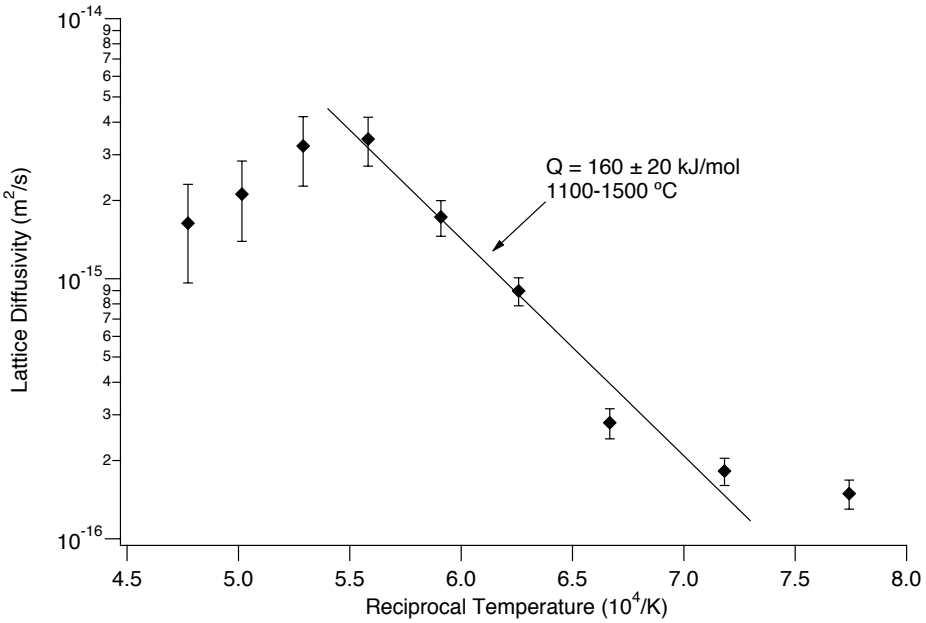

Figure 4.41. Arrhenius plot for the lattice diffusion model given by Equation 4.3 and applied to SPS pure tungsten data for samples sintered between 1000 and 1800 ºC. The apparent activation energy was found to be 160±20 kJ/mol between 1100 and 1500 ºC. The error bars on the diffusivities are based on the multivariate propagation of error formula given by Navidi.[122] The error bars on the reciprocal temperature are contained within the plot markers.

The diffusivities for the SPS tungsten samples produced between 1000 and 1800 ºC calculated using the lattice diffusion model are shown in Figure 4.41. Grain size data and pore size data were not collected for the 800 and 900 ºC samples, and the lattice diffusion model could not be used with these samples. In Figure 4.41, the diffusivities that appear to follow a linear relationship and have a negative slope are the samples produced between 1100 and 1500 ºC. Although the samples spark plasma sintered between 1600 and 1800 ºC can be fit with a linear function, the slope of the function

would be positive, which would result in a negative apparent activation energy. Because a negative activation energy does not make physical sense, a rate-limiting mechanism other than lattice diffusion is responsible for densification at these temperatures.

An apparent activation energy was calculated from the slope of a best-fit line for the samples produced between 1100 and 1500 ºC. The slope is equal to $-Q/R$, where Q is the apparent activation energy, and R is the ideal gas constant. The apparent activation energy was found to be about 160±20 kJ/mol, using the lattice diffusion model. The uncertainty in the apparent activation energy is based on the multivariate propagation of error formula given by Navidi,[122] and contributions to the uncertainty include the temperature, the average grain size, the density, the densification rate, and the pore size radius.

The lattice diffusion constant, D_{ov}, was calculated using the apparent activation energy of 160±20 kJ/mol and the calculated diffusivities between 1100 and 1500 ºC. The lattice diffusion constant was calculated to be $(1.4\pm0.3)\times10^{-10}$ m^2/s. The error in the calculated lattice diffusion constant is based on the propagation of error formula given by Navidi,[122] and the uncertainties in the diffusivities and activation energies were used. From these calculations, the Arrhenius relationship for lattice diffusion during spark plasma sintering of tungsten is:

$$D_v = (1.4 \pm 0.3)\exp\left(\frac{-160 \pm 20}{RT}\right) \times 10^{-10} \ (\mathrm{m^2/s}) \qquad 4.9$$

where D_v is the lattice diffusion coefficient and the activation energy has units of kJ/mol.

Comparing the diffusion constant and the apparent activation energy calculated using the lattice diffusion model to values in the literature, the rate-limiting mechanism in the spark plasma sintering of tungsten is likely not lattice diffusion. Two fundamental

studies on the diffusivities and activation energies for lattice diffusion in tungsten have been reported. In the first study, Andelin *et al.* reported the diffusion constant is $(4.28\pm0.48)\times10^{-3}$ m^2/s and the activation energy is 641±3 kJ/mol for lattice diffusion in the temperature range 2660 to 3230 ºC.[89] In the second study, Pawel and Lundy reported the diffusion constant is 1.88×10^{-4} m^2/s and the activation energy is 587 kJ/mol for lattice diffusion in the temperature range 1300 to 2400 ºC.[90] For lattice diffusion to be the rate-limiting mechanism of densification in SPS tungsten, the diffusion constant would have to be close to or greater than the values reported by Andelin *et al.*[89] and by Pawel and Lundy.[90] The difference in the diffusion constant calculated in this thesis and the diffusion constants in the literature are different by orders of magnitude, and the calculated diffusion constant is less than the values in the literature. Therefore, the rate-limiting mechanism in SPS tungsten is likely not lattice diffusion. In addition to the diffusion constants, the large discrepancy between the calculated activation energy (160±20 kJ/mol) and the activation energies for lattice diffusion (587 to 641 kJ/mol) implies that the rate-limiting mechanism is probably not lattice diffusion.

It is possible that the hot press model used to calculate the diffusivities and activation energy are not applicable to spark plasma sintering of tungsten. If the hot press model for lattice diffusion is not applicable to spark plasma sintering, it is possible that the diffusivities and activation energy for lattice diffusion are greater and may be close to or greater than the values reported in the literature. Future research on spark plasma sintering of tungsten using alternative sintering models is necessary to confirm or negate the results obtained in this thesis.

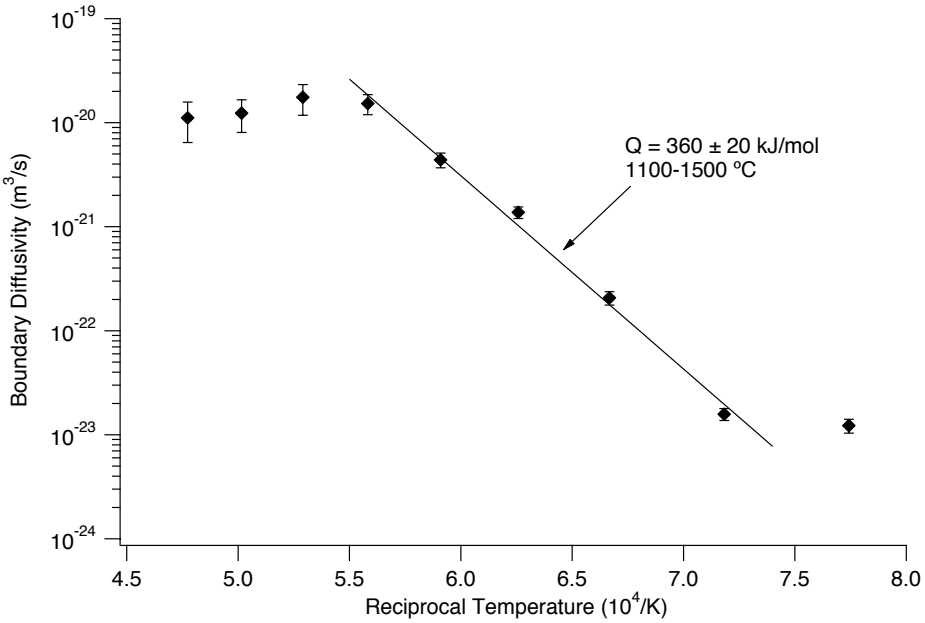

Figure 4.42. Arrhenius plot for the boundary diffusion model given by Equation 4.4 and applied to SPS pure tungsten data for samples sintered between 1000 and 1800 ºC. The apparent activation energy was found to be 360±20 kJ/mol between 1100 and 1500 ºC. The error bars on the diffusivities are based on the multivariate propagation of error formula given by Navidi.[122] The error bars on the reciprocal temperature are contained within the plot markers.

The diffusivities for the SPS tungsten samples produced between 1000 and 1800 ºC calculated using the boundary diffusion model are shown in Figure 4.42. Grain size data and pore size data were not collected for the 800 and 900 ºC samples, and the boundary diffusion model could not be used with these samples. In Figure 4.42, the only diffusivities that appear to follow a linear relationship are for the samples produced between 1100 and 1500 ºC. Although the samples spark plasma sintered between 1600 and 1800 ºC can be fit with a linear function, the slope of the function would be positive,

which would result in a negative apparent activation energy. Because a negative activation energy does not make physical sense, a rate-limiting mechanism other than boundary diffusion is responsible for densification at these temperatures.

An apparent activation energy was calculated from the slope of a best-fit line for the samples produced between 1100 and 1500 ºC. The slope is equal to $-Q/R$, where Q is the apparent activation energy, and R is the ideal gas constant. The apparent activation energy was found to be about 360±20 kJ/mol, using the boundary diffusion model. The uncertainty in the apparent activation energy is based on the multivariate propagation of error formula given by Navidi,[122] and contributions to the uncertainty include the temperature, the average grain size, the density, the densification rate, and the pore size radius.

The boundary diffusion constant, D_{ob}, was calculated using the apparent activation energy of 360±20 kJ/mol and the calculated diffusivities between 1100 and 1500 ºC. The boundary diffusion constant was calculated to be $(4.3\pm0.1)\times10^{-10}$ m^3/s. The diffusion constant contains the grain boundary width, which is why the boundary diffusion constant has units of m^3/s. Kreider and Bruggeman assumed the grain boundary width in tungsten is about 3 atomic diameters (about 10 Å),[88] and this assumption was used to convert the boundary diffusion constant found in this thesis from m^3/s to m^2/s. Assuming the boundary width is 10 Å, the boundary diffusion constant becomes 4.3±0.1 m^2/s. The error in the calculated boundary diffusion constant is based on the propagation of error formula given by Navidi,[122] and the uncertainties in the diffusivities and activation energies were used. From these calculations, the Arrhenius relationship for boundary diffusion during spark plasma sintering of tungsten is:

$$D_b = (4.3 \pm 0.1)\exp\left(\frac{-360 \pm 20}{RT}\right) (\mathrm{m^2/s}) \qquad 4.10$$

where D_b is the boundary diffusion coefficient, and the activation energy has units of kJ/mol.

Comparing the diffusion constant and the apparent activation energy calculated using the boundary diffusion model to values in the literature, it is plausible that the rate-limiting mechanism in the spark plasma sintering of tungsten is boundary diffusion. Kreider and Bruggeman measured the boundary diffusion of tungsten between 1400 and 2200 ºC, and they reported that the diffusion constant is $(3.33\pm0.15)\times10^{-4}$ m^2/s and the activation energy is 385±8 kJ/mol.[88] For boundary diffusion to be the rate-limiting mechanism of densification in SPS tungsten, the diffusion constant would have to be close to or greater than the values reported by Kreider and Bruggeman.[88] The diffusion constant calculated in this thesis is about four orders of magnitude greater than the values measured by Kreider and Bruggeman, so it is possible that boundary diffusion is the rate-limiting mechanism of densification in SPS tungsten between 1100 and 1500 ºC. A comparison between the activation energy reported by Kreider and Bruggeman (385±8 kJ/mol) and the activation energy calculated in this thesis (360±20 kJ/mol) are similar, which may imply that boundary diffusion is the rate-limiting mechanism for densification in SPS tungsten between 1100 and 1500 ºC.

The diffusivities and activation energy calculated using the boundary diffusion hot press model were also compared to densification studies of tungsten sintering. No hot pressing diffusivities are available in the open literature, and only diffusivities for pressureless sintering of tungsten have been published. The diffusivities calculated using the hot press model for boundary diffusion were compared to pressureless sintering

studies by Kothari[95] and Vasilos and Smith,[99] and these diffusivities are plotted in Figure 4.43. In addition to the diffusivities from Kothari[95] and Vasilos and Smith,[99] the diffusivities for boundary diffusion found by Kreider and Bruggeman[88] and for lattice diffusion found by Pawel and Lundy[90] are plotted in Figure 4.43 for comparison.

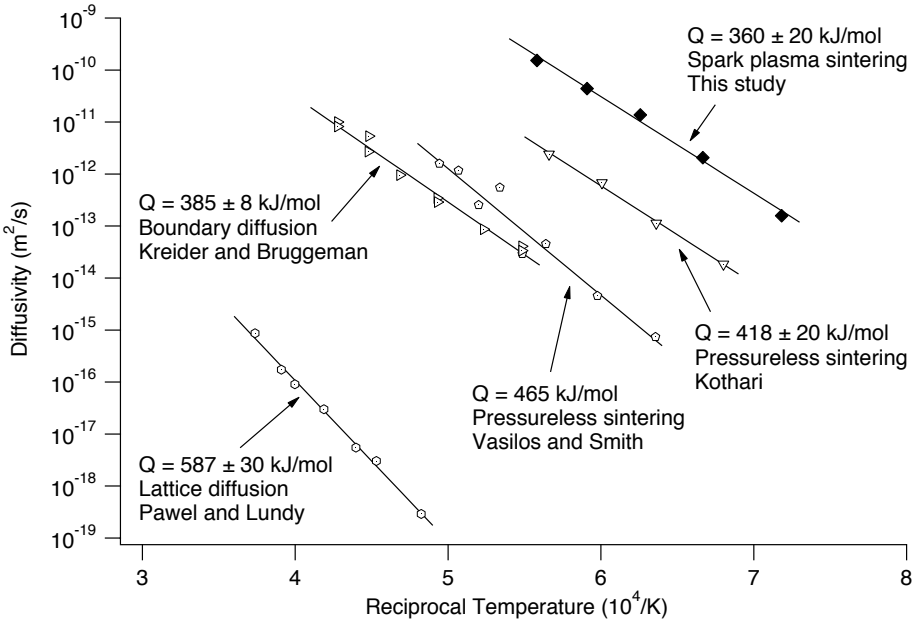

Figure 4.43. Arrhenius plot comparing the diffusivities calculated for the boundary diffusion model given by Equation 4.4 and diffusivities for pressureless sintering,[95,99] boundary diffusion,[88] and lattice diffusion.[90]

In the studies by Kothari[95] and Vasilos and Smith,[99] the apparent activation energies were attributed to boundary diffusion being the rate-limiting mechanism for tungsten densification for the temperature ranges studied. As shown in Figure 4.43, the apparent activation energy for spark plasma sintered tungsten is lower than the apparent activation energies found by both Kothari[95] and Vasilos and Smith.[99] In other tungsten sintering studies, the apparent activation energy has been measured to be between 290 and 440 kJ/mol.[83,105,106] The lowest activation energy was measured by Chen, and the

apparent activation energy for tungsten densification between 1000 and 1750 ºC was 318 kJ/mol for tungsten with an initial particle size of 1.2 μm. The apparent activation energies were attributed to boundary diffusion being the rate-limiting mechanism,[102] even though the activation energy is less than the activation energy for boundary diffusion reported by Kreider and Bruggeman.[88] It is possible that in nonisothermal sintering, the activation energy for boundary diffusion is lower than the activation energy for boundary diffusion in isothermal sintering; however, this is a hypothesis and it is beyond the scope of this thesis. A summary of the apparent activation energies for tungsten sintering from the literature and the apparent activation energy for SPS tungsten is given in Table 4.4.

Table 4.4. Apparent activation energies for tungsten sintering and the proposed rate-limiting mechanisms.

Temperature range (ºC)	Activation energy (kJ/mol)	Proposed rate-limiting mechanism	Source	Comments
1100-1500	360±20	Boundary diffusion	This study	Calculated from boundary hot press model
1000-1750	318±21	Boundary diffusion	Chen[102]	Dilatometry study using 1.2 μm tungsten
1050-1200	380	Boundary diffusion	Hayden and Brophy[106]	Activation energy found by linear shrinkage
1100-1500	418±20	Boundary diffusion	Kothari[95]	Activation energy found by volume shrinkage and degree of sintering
1300-1750	465	Boundary diffusion	Vasilos and Smith[99]	Activation energy found using model by Coble[39]
1800-3100	440	None given	Pugh and Amra[105]	Activation energy for 95% dense tungsten
1800-2300	50±4	Particle rearrangement	Karpinos *et al.*[82]	Activation energy for 45-58% dense tungsten
1800-2300	140±4	Plastic flow	Karpinos *et al.*[82]	Activation energy for 58-75% dense tungsten
1800-2300	414±13	Boundary diffusion	Karpinos *et al.*[82]	Activation energy for >80% dense tungsten

Another possibility for the lower apparent activation energy is that the hot press model for boundary diffusion is not applicable to SPS tungsten, but it may serendipitously find activation energies close to the activation energy for boundary diffusion. It is also possible that the limited data used to find the apparent activation energy of 360±20 kJ/mol might have a bias that is not evident in this analysis. Further spark plasma sintering experiments in the temperature range 1100 to 1500 ºC are necessary to determine if the boundary diffusion model can be applied to the SPS data.

The lower apparent activation energy may also be attributed to an unknown mechanism in SPS; however, this is not likely. Anselmi-Tamburini *et al.* measured the activation energy for the rate of growth of a $MoSi_2$ layer formed at a molybdenum-silicon interface in SPS, and they found the activation energy is the same as the activation energy for the rate of growth a $MoSi_2$ layer in pressureless sintering.[67] In a similar study, Kondo *et al.* spark plasma sintered niobium and carbon, and found the activation energy for the formation of Nb_2C and NbC layers in spark plasma sintering is the same as the activation energy for formation of these layers in the absence of current.[79] Assuming that these studies on the activation energy of growth in $MoSi_2$[67] and Nb_2C and NbC[79] are analogous to spark plasma sintering of tungsten, then it is unlikely that the lower apparent activation energy calculated for tungsten is due to current effects in SPS.

Another method to compare the densification kinetics of SPS tungsten with pressureless sintered tungsten and diffusion mechanisms is to compare the diffusion constants in the literature with the diffusion constant calculated for SPS tungsten. The diffusion constant for SPS tungsten was calculated to be 4.3±0.1 m^2/s using the hot press boundary diffusion model. Kothari reported apparent diffusivities for tungsten sintering;

however, Kothari did not report the diffusion constant.[95] The diffusion constant in Kothari's study was determined from the reported diffusivities and the reported activation energy, and was found to be 17.3 m^2/s.[95] Using the diffusion data from the study by Vasilos and Smith,[99] Kreider and Bruggeman calculated the diffusion constant for tungsten sintering to be 1.36 m^2/s.[88] The diffusion constant for boundary diffusion, as determined by Kreider and Bruggeman, is 3.33 m^2/s,[88] which is on the same order of magnitude as the diffusion constant calculated in this thesis and the diffusion constant from the Vasilos and Smith data.[99]

The diffusion constant calculated from Kothari's data[95] is a bit dubious due to how large it is when compared with the diffusion constants from Kreider and Bruggeman[88] and Vasilos and Smith.[99] A reevaluation in this thesis of the diffusivities reported by Kothari resulted in an apparent activation energy of 360 kJ/mol, and this decrease in activation energy from the reported activation energy revised the diffusion constant to 0.18 m^2/s. It is unclear how Kothari determined the apparent activation energy from the diffusivity data,[95] and the wide range of possible diffusion constants makes it near impossible to compare Kothari's results to the results in this thesis.

Based on the activation energy and the diffusion constant calculated for SPS tungsten using the hot press model for boundary diffusion, it is possible that the rate-limiting mechanism for densification in SPS tungsten between 1100 and 1500 ºC is boundary diffusion. While more experiments are necessary on SPS tungsten to confirm these results, it appears that the boundary diffusion model for hot pressing is also applicable to spark plasma sintering of tungsten.

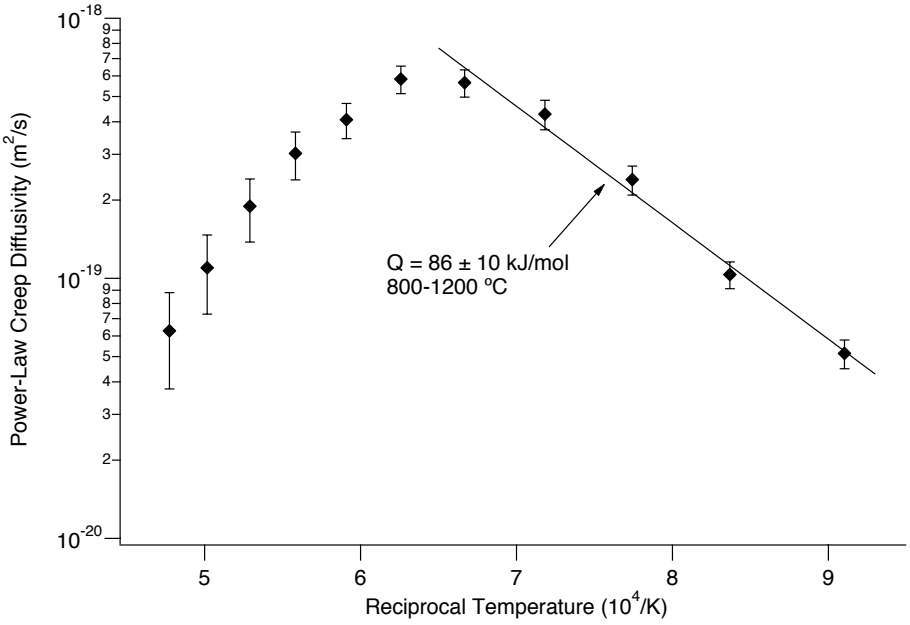

Figure 4.44. Arrhenius plot for the power-law creep model given by Equation 4.5 and applied to SPS pure tungsten data for samples sintered between 800 and 1800 ºC. The apparent activation energy was found to be 86±10 kJ/mol between 800 and 1200 ºC. The error bars on the diffusivities are based on the multivariate propagation of error formula given by Navidi.[122] The error bars on the reciprocal temperature are contained within the plot markers.

The diffusivities for the SPS tungsten samples produced between 800 and 1800 ºC calculated using the power-law creep model are shown in Figure 4.44. In Figure 4.44, the diffusivities that appear to follow a linear relationship and have a negative slope are the samples produced between 800 and 1200 ºC. Although the samples spark plasma sintered between 1300 and 1800 ºC can be fit with a linear function, the slope of the function would be positive, which would result in a negative apparent activation energy.

Because a negative activation energy does not make physical sense, a rate-limiting mechanism other than power-law creep is responsible for densification at these temperatures.

An apparent activation energy was calculated from the slope of a best-fit line for the samples produced between 800 and 1200 ºC. The slope is equal to -Q/R, where Q is the apparent activation energy, and R is the ideal gas constant. The apparent activation energy was found to be about 86±10 kJ/mol, using the power-law creep model. The uncertainty in the apparent activation energy is based on the multivariate propagation of error formula given by Navidi,[122] and contributions to the uncertainty include the temperature, the density, and the densification rate.

The diffusion constant for power-law creep is the same as the lattice diffusion constant, D_{ov}, and was calculated using the apparent activation energy of 86±10 kJ/mol and the calculated diffusivities between 1100 and 1500 ºC. The lattice diffusion constant was calculated to be $(8.4\pm6.4)\times10^{-13}$ m^2/s. The error in the calculated lattice diffusion constant is based on the propagation of error formula given by Navidi,[122] and the uncertainties in the diffusivities and activation energies were used. From these calculations, the Arrhenius relationship for lattice diffusion during spark plasma sintering of tungsten is:

$$D_v = (8.4 \pm 6.4)\exp\left(\frac{-86 \pm 10}{RT}\right) \times 10^{-13} \ (\mathrm{m^2/s}) \qquad 4.11$$

where D_v is the lattice diffusion coefficient and the activation energy has units of kJ/mol.

Comparing the diffusion constant and the apparent activation energy calculated using the power-law creep model to values in the literature, the rate-limiting mechanism in the spark plasma sintering of tungsten is likely not power-law creep. Two fundamental

studies on the diffusivities and activation energies for lattice diffusion in tungsten have been reported. In the first study, Andelin *et al.* reported the diffusion constant is $(4.28\pm0.48)\times10^{-3}$ m^2/s and the activation energy is 641±3 kJ/mol for lattice diffusion in the temperature range 2660 to 3230 ºC.[89] In the second study, Pawel and Lundy reported the diffusion constant is 1.88×10^{-4} m^2/s and the activation energy is 587 kJ/mol for lattice diffusion in the temperature range 1300 to 2400 ºC.[90] For power-law creep to be the rate-limiting mechanism of densification in SPS tungsten, the diffusion constant would have to be close to or greater than the values reported by Andelin *et al.*[89] and by Pawel and Lundy.[90] The difference in the diffusion constant calculated in this thesis and the diffusion constants in the literature are different by orders of magnitude, and the calculated diffusion constant is less than the values in the literature. Therefore, the rate-limiting mechanism in SPS tungsten is likely not power-law creep. In addition to the diffusion constants, the large discrepancy between the calculated activation energy (86±10 kJ/mol) and the activation energies for lattice diffusion (587 to 641 kJ/mol) implies that the rate-limiting mechanism is probably not power-law creep.

It is possible that the hot press model for power-law creep used to calculate the diffusivities and activation energy are not applicable to spark plasma sintering of tungsten. If the hot press model for power-law creep is not applicable to spark plasma sintering, it is possible that the diffusivities and activation energy for power-law creep are greater and may be close to or greater than the values reported in the literature. Future research on spark plasma sintering of tungsten using alternative sintering models is necessary to confirm or negate the results obtained in this thesis.

In all three of the hot pressed models used in this section, the calculated diffusivities at higher temperatures showed a positive slope correlation, which implies that none of these models effectively describes the kinetics of densification at higher temperatures. One reason a positive slope at higher temperatures may exist is because the models all rely on the densification rate, $d\rho/dt$, to be a known value at all temperatures. The sigmoid function fit to the densification data, given by Equation 4.7, may not be the correct fitting function, and the densification rates may be greater at higher temperatures than those reported in this section. It is also possible that mechanisms other than lattice diffusion, boundary diffusion, or power-law creep are rate-limiting at higher temperatures. Olevsky and Froyen produced models of SPS that include the effects of localized temperature gradients, the Soret-Chipman effect, and electromigration, and they have suggested that some of these mechanisms may be active in the intermediate and final stages of sintering.[1,68] These mechanisms may explain the shortcomings of the hot press models to fully describe the spark plasma sintering kinetics at higher temperatures. Future work is necessary to determine if the hot press models can be modified to include these proposed mechanisms.

4.7.3. Interpretation of Densification Kinetics by Pressure Sintering Maps

In the previous section, hot press models for lattice diffusion, boundary diffusion, and power-law creep were used to try and elucidate the mechanism of SPS tungsten densification. An alternative to evaluating each model for the sintering data is to compare the possible sintering mechanisms by constructing pressure sintering maps. Pressure sintering maps are visual tools to help aid in determining the rate-limiting mechanism of pressure-assisted sintering at a given temperature, applied pressure,

density, and grain size.[47] There are no pressure sintering maps for hot pressing or spark plasma sintering of tungsten in the open literature, so pressure sintering maps for tungsten were created for this thesis. The pressure sintering maps presented in this section are based on the assumption that spark plasma sintering does not affect the activation energies or the diffusivities of the mechanisms responsible for densification. The validity of this assumption is discussed later in this section.

To construct pressure sintering maps of tungsten, the mechanisms of densification considered were volume diffusion, boundary diffusion, and power-law creep. The models for volume diffusion, boundary diffusion, and power-law creep are given in Equation 2.14, Equation 2.15, and Equation 2.16, respectively. These equations were set equal to one another and solved for the grain size as a function of temperature, pressure, and density, and are shown here:

$$G(T) = X\frac{3}{40}\frac{D_{ob}}{D_{ov}}\exp\left(\frac{Q_v - Q_b}{RT}\right) \qquad 4.12$$

$$G(T,P_A,\rho) = \left(\frac{40}{3}\frac{a_o^{\,3}}{A^* b}\left(\frac{P_A}{\mu(T)\rho}\right)^{n-1}\right)^{1/2} \qquad 4.13$$

$$G(T,P_A,\rho) = \left(X\frac{a_o^{\,3}}{A^* b}\frac{D_{ob}}{D_{ov}}\exp\left(\frac{Q_v - Q_b}{RT}\right)\left(\frac{P_A}{\mu(T)\rho}\right)^{n-1}\right)^{1/3} \qquad 4.14$$

where Equation 4.12 is the boundary between lattice diffusion and boundary diffusion, Equation 4.13 is the boundary between lattice diffusion and power-law creep, and Equation 4.14 is the boundary between boundary diffusion and power-law creep. It should be noted that the boundary between volume diffusion and boundary diffusion is independent of applied pressure and density. The temperature-dependent shear modulus, $\mu(T)$, is defined in Equation 2.17, and is restated here[44]:

$$\mu(T) = \mu_o\left(1 + \frac{(T-300)}{T}\frac{T_m}{\mu_o}\frac{d\mu}{dT}\right) \qquad 4.15$$

A summary of the symbol definitions for Equations 4.12-4.15 is given in Table 4.5.

Table 4.5. Definitions of variables in Equations 4.12-4.15.

Symbol	Definition	Symbol	Definition
G	Average grain size	Q_b	Activation energy for boundary diffusion
T	Absolute temperature	A^*	Dorn parameter for shear stress
P_A	Applied pressure	n	Power-law creep exponent
ρ	Density	a_o^3	Atomic volume
X	Geometric term	b	Burgers vector
R	Ideal gas constant	μ_o	Shear modulus at 300 K
D_{ov}	Lattice diffusion constant	T_m	Melting temperature
D_{ob}	Boundary diffusion constant	$(T_m/\mu_o)(d\mu/dt)$	Temperature dependence of shear modulus
Q_v	Activation energy for lattice diffusion		

The geometric term X in Table 4.5 is equal to 95/2 in intermediate stage sintering and 15/2 in final stage sintering.[40] The Dorn parameter for shear stress, A^*, is converted from the Dorn parameter measured for tensile stress, A, by multiplying A by $3^{(1-n)/2}$.

To construct the pressure sintering maps, two of the variables (T, P_A or ρ) had to be set to fixed values, with the third variable being the independent variable. To construct the maps, the physical and kinetics properties of tungsten, shown in Table 4.6, were used. For each of the maps, the temperature was fixed at 1200, 1300, 1400, or 1500 ºC, and the pressure was fixed at 64 MPa (Figure 4.45). The average grain size and density of tungsten spark plasma sintered at 1200, 1300, 1400, and 1500 ºC are overlaid into the diagrams (Figure 4.45). Both the boundary lines for lattice diffusion/boundary diffusion (Equation 4.12) and lattice diffusion/power-law creep (Equation 4.13) are only

valid for much larger grain sizes than shown on the maps. The jog in the boundary lines between fractional densities of 0.85 and 0.86 are due to the value of X, which was set to 95/2 for densities less than or equal to 0.85 (intermediate stage sintering) and 15/2 for densities greater than 0.85 (final stage sintering).

Table 4.6. Physical and kinetics properties of tungsten used to construct pressure sintering maps.

Property	Symbol	Value	Source
Atomic volume	a_o^3	1.59×10^{-29} m^3	Ashby[45]
Burgers vector	b	2.74×10^{-10} m	Ashby[45]
Melting temperature	T_m	3683 K	German[25]
Shear modulus at 300K	μ_o	1.60×10^{5} MPa	Frost and Ashby[44]
Temperature dependence of modulus	$(T_m/\mu_o)(d\mu/dT)$	-0.38	Frost and Ashby[44]
Volume diffusion pre-exponential	D_{ov}	1.88×10^{-4} m^2/s	Pawel and Lundy[90]
Volume diffusion activation energy	Q_v	587 kJ/mol	Pawel and Lundy[90]
Boundary diffusion pre-exponential	D_{bo}	3.33×10^{-13} m^3/s	Kreider and Bruggeman[88]
Boundary diffusion activation energy	Q_b	385 kJ/mol	Kreider and Bruggeman[88]
Power-law creep exponent	n	4.7	Frost and Ashby[44]
Dorn constant	A	1.1×10^{8}	Frost and Ashby[44]

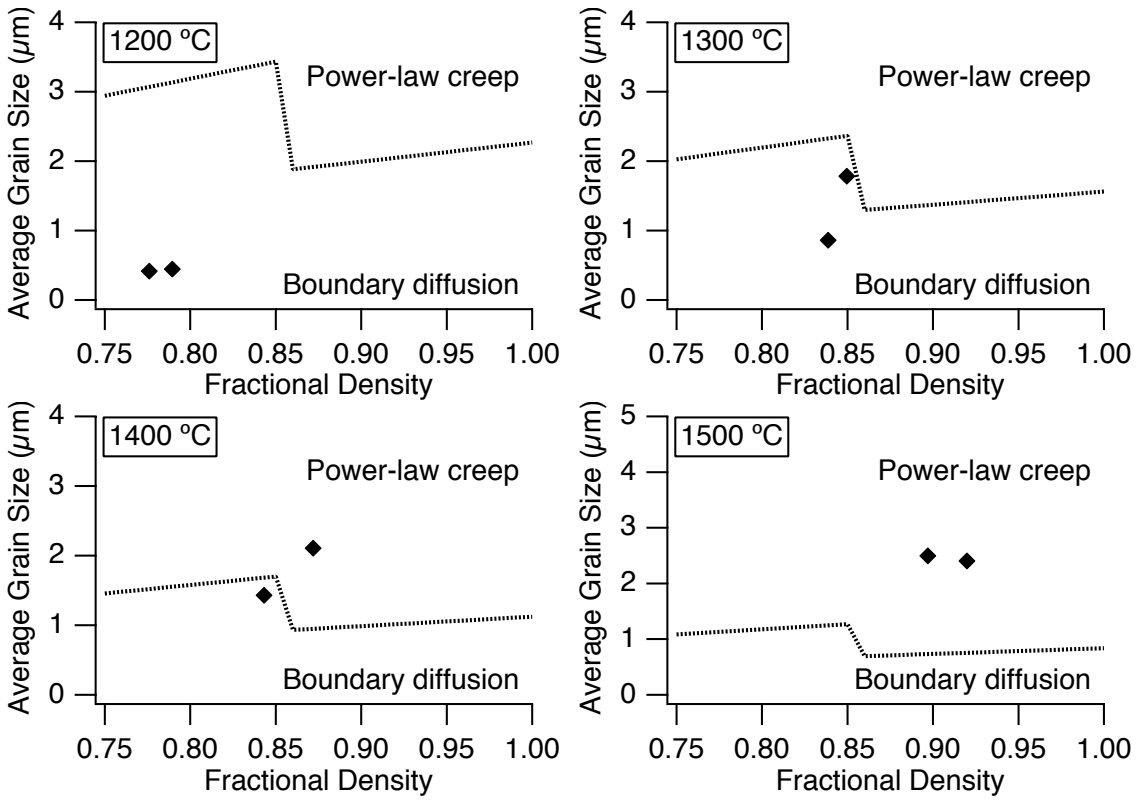

Figure 4.45. Pressure sintering maps for pure tungsten sintered at 1200, 1300, 1400, and 1500 ºC with 64 MPa applied pressure. The dotted line is the boundary line between rate-limiting mechanisms, and the rate-limiting mechanisms are shown. The error bars on the average grain sizes and fractional densities are contained within the plot markers.

The pressure sintering maps in Figure 4.45 show that for samples sintered at 1200 ºC, boundary diffusion is the rate-limiting mechanism for densification, and for samples sintered at 1500 ºC, power-law creep is the rate-limiting mechanism for densification. The samples sintered at 1300 and 1400 ºC show that the rate-limiting mechanism changes from boundary diffusion to power-law creep.

The results shown in Figure 4.45 should not be used as conclusive evidence of a mechanism change between 1300 and 1400 ºC because the maps were constructed based

on the assumption that the parameters in Table 4.6 are still valid in spark plasma sintering; instead, the maps should be used as a first approximation. While the physical properties, such as the Burgers vector, will not change in spark plasma sintering, the diffusion constants and activation energies for boundary diffusion and volume diffusion may be different in SPS. In Section 4.7.2, the model that appeared to fit the SPS data best was the boundary diffusion model, and the model appeared to be applicable for samples sintered between 1100 and 1500 ºC. The pressure sintering diagrams in Figure 4.45 indicate the mechanism of densification changes between 1300 and 1400 ºC, and it is unclear what the rate-limiting mechanism of sintering is between 1300 and 1500 ºC.

Because pressure sintering diagrams are based on kinetics values for traditional sintering, the model is applicable to traditional pressure-assisted sintering, but it may not be directly applicable to spark plasma sintering.[1,15,68] Chaim[28] and Chaim and Margulis[29] have attempted to construct spark plasma sintering diagrams based on hot isostatic pressing (HIP) models, and they concluded the HIP models do fit the data well. However, Chaim[28] and Chaim and Margulis[29] do express reservations their results, because the models do not account for the initial stage of sintering, and possible mechanisms unique to spark plasma sintering are ignored. Olevsky and Froyen produced models of SPS that include the effects of localized temperature gradients, the Soret-Chipman effect, and electromigration, and they have suggested that some of these mechanisms may be active in the intermediate and final stages of sintering.[1,68] If this is true, the current pressure-assisted sintering models used to construct pressure sintering diagrams may not be a fully-inclusive way of describing the mechanisms of sintering in SPS.

4.8. Grain Growth Kinetics of SPS Tungsten

The kinetics of grain growth in sintering materials is typically determined for materials sintered isothermally; however, models do exist to analyze the grain growth kinetics in nonisothermal sintering. Boutz *et al.*[138] derived a grain growth equation for materials sintered at a constant heating rate, and this model was used to analyze the kinetics of grain growth in tungsten spark plasma sintered between 800 and 1800 ºC. The model was found to be too sensitive to variations in the average grain sizes and sintering temperatures of the SPS tungsten data, and no meaningful grain growth exponent or activation energy could be determined using this model.

Because the nonisothermal model by Boutz *et al.* could not be reliably used, the isothermal grain growth kinetics of SPS tungsten were analyzed using the traditional grain growth law.[124] The average grain sizes of pure tungsten spark plasma sintered at 1200, 1500, and 1800 ºC and soaked between 2 and 26 min were used to analyze the isothermal grain growth kinetics. The isothermal grain growth law is given by Equation 2.5, and it is restated here:

$$G^n - G_o^{\ n} = Kt \qquad 4.16$$

where G is the grain size at time t, G_o is the initial grain size, K is the isothermal grain growth rate, and n is the grain growth exponent.[124] In Equation 4.16, the isothermal grain growth rate, K, is equal to:

$$K = K_o \exp\left(\frac{-Q}{RT}\right) \qquad 4.17$$

where K_o is a rate constant, Q is the activation energy for grain growth, and T is the absolute temperature.[124] Substituting Equation 4.17 into Equation 4.16, the grain growth law is given as a function of time and temperature[124]:

$$G^n - G_o^{\,n} = K_o t \exp\left(\frac{-Q}{RT}\right) \qquad 4.18$$

and taking the natural log of both sides and rearranging the equation gives[124]:

$$\ln\left(\frac{G^n - G_o^{\,n}}{t}\right) = -\frac{Q}{RT} + \ln\left(K_o\right) \qquad 4.19$$

From the relationship between grain size, sintering time, and sintering temperature in Equation 4.19, the left-hand side can be plotted as a function of $1/T$, and the slope of the line is equal to $-Q/R$. The quantity $(G^n\text{-}G_o^{\,n})/t$ is the rate of grain growth at a given temperature.

In order to use Equation 4.19 to find the activation energy of grain growth, the grain growth exponent, n, must be known. To find the grain growth exponent, a log-log plot of G^n vs. t was constructed, and n was varied until the slope of G^n vs. t was equal to one.[139] A log-log plot was constructed using the isothermal sintering data for pure tungsten spark plasma sintered at 1200, 1500, and 1800 ºC, and the grain growth exponents resulting in a slope of one were 6.4, 6.2, and 1.9, respectively. The large values for the grain growth exponent at 1200 and 1500 ºC are not typical. For comparison, Mistler found the grain growth exponent was 2 at 1450 and 1600 ºC and 3 at 1650 ºC in pressureless sintering of tungsten.[139]

Because the calculated values for n were not realistic, the grain growth exponent for spark plasma sintered tungsten was assumed to be 2 or 3, based on the grain growth exponents found by Mistler.[139] This assumption may not be valid, because the grain

growth exponent may change with differing temperatures.[124] In this analysis, it is assumed that the grain growth exponent is constant at all temperatures. The average grain growth rate at a given temperature was found by plotting the quantity (G^n-G_o^n) as a function of time, and the resulting slope of the line was the average grain growth rate. The grain growth rates of pure tungsten sparked plasma sintered at 1200, 1500, and 1800 ºC were calculated using n = 2 and n = 3, and a summary of these results is given in Table 4.7.

Table 4.7. Average grain growth rates for tungsten spark plasma sintered at 1200, 1500, and 1800 ºC assuming a grain growth exponent of 2 or 3.

Isothermal sintering temperature (ºC)	Assumed grain growth exponent, n	Average grain growth rate (μm^n/min)	Normal standard deviation of grain growth rate (μm^n/min)
1200 ºC	2	8.37×10^{-3}	1.87×10^{-3}
1500 ºC	2	4.66×10^{-1}	5.01×10^{-2}
1800 ºC	2	7.79×10^{0}	1.39×10^{0}
1200 ºC	3	7.54×10^{-3}	1.50×10^{-3}
1500 ºC	3	2.81×10^{0}	2.91×10^{-1}
1800 ºC	3	1.22×10^{2}	2.91×10^{1}

To solve for the activation energy of grain growth using Equation 4.19 and assuming the grain growth exponent is 2 or 3, the logarithm of the grain growth rates in Table 4.7 were plotted as a function of reciprocal isothermal sintering temperature. These results are shown in Figure 4.46. The slope of the resulting line is equal to $-Q/R$, where Q is the activation energy for grain growth and R is the ideal gas constant. Based on the results shown in Figure 4.46, if the grain growth exponent is 2 at 1200, 1500, and 1800 ºC, then the activation energy for grain growth of SPS tungsten is 289±10 kJ/mol. If the grain growth exponent is 3 at these given temperatures, then the activation energy

for grain growth of SPS tungsten is 411±12 kJ/mol. The standard deviations of the grain growth rates, shown in Table 4.7, were used to calculate the error in the activation energies using a statistical bootstrapping method.[122]

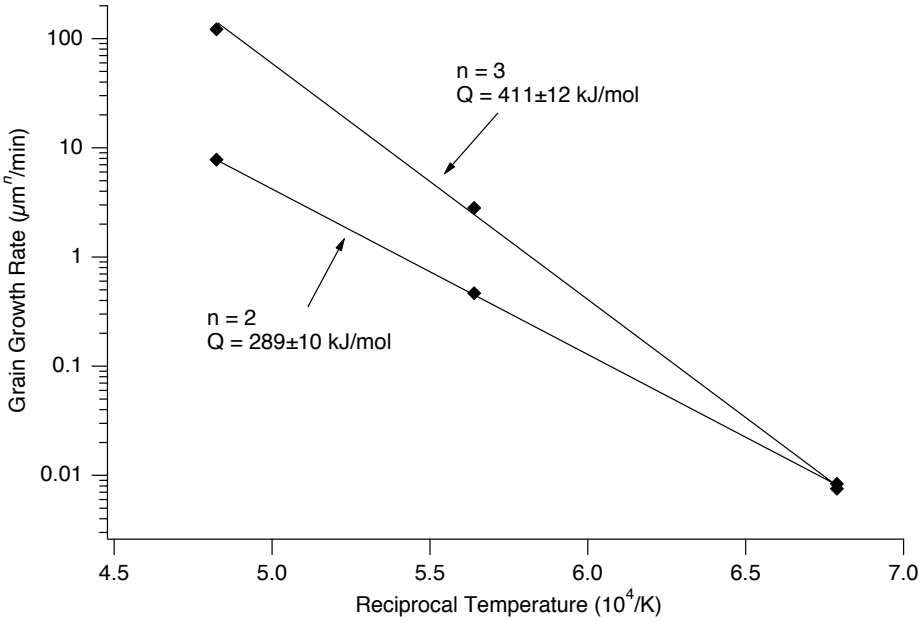

Figure 4.46. Arrhenius-type plot of isothermal grain growth rates for pure tungsten spark plasma sintered at 1200, 1500, and 1800 ºC. The grain growth exponent, *n*, was assumed to be 2 or 3. The apparent activation energies for grain growth were 289±10 kJ/mol for $n = 2$, and 411±12 kJ/mol for $n = 3$. The error in the activation energies was calculated by a bootstrapping method using the standard deviations in Table 4.7.

The activation energy of 289±10 kJ/mol, calculated for $n = 2$, is within the reported range of activation energies for surface diffusion in tungsten. Bettler and Charbonnier measured an activation energy of 269 kJ/mol for surface diffusion of tungsten in a high electric field,[85] and Barbour *et al*. measured an activation energy of

301 kJ/mol for surface diffusion of tungsten.[86] This comparison implies that the rate-limiting mechanism for grain growth in SPS tungsten is surface diffusion.

The activation energy of 411±12 kJ/mol, calculated for $n = 3$, is close to the 385 kJ/mol activation energy for boundary diffusion measured by Kreider and Bruggeman.[88] This comparison implies that the rate-limiting mechanism for grain growth in SPS tungsten is boundary diffusion.

The rate-limiting mechanism for grain growth in SPS tungsten cannot be determined based on the work presented in this thesis. First, more isothermal sintering experiments are necessary to determine the grain growth exponent. The grain growth exponents calculated in this study were based on a single sample produced at each sintering time and temperature, and a total of only 6 samples were produced at each temperature. Future work on grain growth kinetics should be undertaken with a greater number of samples produced at each time and temperature, and the interval between the soak times should be shortened from the 3 to 6 min used in this study to about 1 to 2 min. In addition to a greater number of samples produced at each temperature, the intervals between sintering temperatures should be reduced from 300 ºC to about 50 ºC. Increasing the number of samples and reducing the temperature intervals should lead to better estimations of the grain growth exponents, and may also determine the temperature ranges for which those grain growth exponents are valid. Once the grain growth exponents in SPS tungsten are better understood, more accurate estimations of the activation energy for grain growth can be made, and the rate-limiting mechanism for grain growth can be determined.

CHAPTER 5: CONCLUSIONS AND FUTURE WORK

5.1. Starting Powders

Comparing the properties of the reduced-and-milled powders to the as-received powders, there does not appear to be any advantage in performing a hydrogen reduction on the precursor tungsten powder. This process may introduce more variations in the starting powder than the as-received powder because of the change in structure of the powder during the reduction process (Figure 4.4). Dry ball milling is not an optimal method to mix the ceria and tungsten powders, and mixing the powders in cyclohexane produces a homogeneous powder mixture. Ball milling may contaminate the powders with iron or nickel from the ball milling vessel. If iron or nickel are present in the tungsten powder, it is possible a liquid phase forms during sintering,[25] which would change the mechanism of densification.

Electron backscatter diffraction was shown to be a viable method to determine the crystallite size distribution in submicron tungsten powders. The crystallite size distribution was shown to fit a lognormal distribution, and confidence intervals for the average crystallite size were determined using the Cox method.[119]

In future spark plasma sintering studies of tungsten-ceria, the powders should not be mechanically milled. Mixing in cyclohexane was effective in mixing the tungsten and ceria powders, and this method for powder mixing is recommended for future experiments on SPS tungsten-ceria.

5.2. Temperature Measurement in SPS

The emissivity of the blackbody cavity in the die was determined to be 0.97. This value was obtained by comparing the temperature recorded by the infrared thermometer and the temperature recorded by a type-K thermocouple in 3 spark plasma sintering runs.

Adjustments to the spark plasma sintering experiments can be made to ensure the accuracy of the recorded temperatures. To determine the emissivity of the die, the infrared thermometer and a thermocouple should be used in tandem to record the die temperature in a spark plasma sintering experiment with a maximum temperature not exceeding the working limit of the thermocouple (1250 ºC for a type-K thermocouple[121]). After the spark plasma sintering run, the average emissivity of the die should be determined using Equation 4.1. This emissivity value should then be programmed into the infrared thermometer in order to record a more accurate die temperature during subsequent SPS experiments. This emissivity determination and infrared thermometer adjustment should be performed at least once per day.

If greater accuracy in temperature measurement during SPS is desired, the infrared thermometer should be coupled with a high-temperature thermocouple during spark plasma sintering. Coupling of two different measurement techniques should help to ensure the correct temperature is recorded during spark plasma sintering. For these experiments, a type-C thermocouple is recommended, because it is capable of measuring temperature up to 2320 ºC with an accuracy of ±1%.[121] Using type-C thermocouples for every spark plasma sintering cycle may be cost prohibitive due to degradation from chemical reactions between the thermocouple and the die. To extend the lifetime of the

thermocouples, a protective alumina sheath (or other inert material) should be placed on the outside of the thermocouples prior to inserting them into the dies.

5.3. Densification of SPS Tungsten and Tungsten-Ceria

Spark plasma sintering was used to successfully consolidate tungsten and tungsten-ceria powders. The final densities of the pure tungsten and tungsten-ceria samples were found to be independent of the applied pressures used (42 and 64 MPa). Densification of the tungsten powders began between 800 and 900 ºC, and high-density (>0.90 fractional density) tungsten samples were produced at temperatures above 1500 ºC. The W-10CeO_2 powders began to densify between 800 and 900 ºC, and high-density W-10CeO_2 samples were produced at temperatures above 1300 ºC (Figure 4.10). The spark plasma sintered tungsten samples had higher densities and were sintered for shorter times than the hot pressed pure tungsten samples (Figure 4.12). Sintering temperature was found to have a greater effect on the final densities of SPS tungsten and tungsten-ceria than isothermal sintering time (Figure 4.14).

To increase the density of SPS tungsten in future experiments, the applied pressure should be increased and a harder vacuum should be used. The application of higher pressures should aid in final stage densification of the compacts. The dies used in this thesis are not capable of withstanding pressures much greater than the 64 MPa used, and new dies would need to be designed if the applied pressure is to be increased. In this thesis, a mechanical pump maintained the vacuum in the SPS chamber, and the vacuum was only about 1 Pa. In future experiments, creating a harder vacuum using the diffusion pump supplied with the SPS should force a greater amount of gas out of the sintering compacts, thus helping to increase the final density of the samples.

5.4. Grain Growth of SPS Tungsten and Tungsten-Ceria

The average tungsten grain sizes and tungsten grain size distributions were measured using electron backscatter diffraction. The tungsten grain sizes in all samples were fit to the lognormal distribution, and confidence intervals for the average grain sizes were determined.

The applied pressures of 42 and 64 MPa did not have a significant effect on the average tungsten grain size in pure tungsten, W-1CeO_2, W-10CeO_2, or W-20CeO_2 (Figure 4.16). The addition of ceria to the tungsten limited the growth of the tungsten grains. It was speculated that the ceria in the W-1CeO_2 samples pinned the tungsten grain boundaries, limiting grain growth of the tungsten. In the W-10CeO_2 and W-20CeO_2 samples, the limited growth of the tungsten grains was hypothesized to be due to an increase in diffusion distance between tungsten grains.

Grain growth of tungsten was only observed in samples spark plasma sintered above 1100 ºC (Figure 4.18). Samples of tungsten spark plasma sintered at 1500 ºC had similar grain growth rates to tungsten hot pressed at 1800 ºC (Figure 4.24). In future SPS studies, the grain growth of pure tungsten can be limited by increased heating rates and shorter sintering times.

For temperatures between 1300 and 1700 ºC, the average grain sizes of pure tungsten spark plasma sintered for 2 min were smaller than those in pure tungsten hot pressed for 30 min (Figure 4.20). The SPS tungsten samples were shown to have tighter grain size distributions than the hot pressed samples. In W-4CeO_2 samples spark plasma sintered or hot pressed between 1300 and 1700 ºC, the average tungsten grain sizes are

similar (Figure 4.21). It is unclear why the grain sizes are similar, and future work is required to understand this phenomenon.

Future experiments on the grain growth of tungsten-ceria should include measurements of the ceria grains as well as the tungsten grains. To easily measure the ceria grains in addition to the tungsten grains, electron backscatter diffraction can be used; however, this technique can only be used if the crystal structure of the ceria phase is known. It is possible that the ceria is in a fluorite structure or a hexagonal structure, depending on the oxidation state of the ceria.

5.5. Hardness of SPS Tungsten and Tungsten-Ceria

The hardness of tungsten and W-1CeO_2 samples was found to increase with increasing density for samples spark plasma sintered between 1300 and 1700 ºC. This increase in hardness was attributed to densification of the samples.

The hardness of the W-10CeO_2 and W-20CeO_2 samples was found to decrease with increasing density for samples spark plasma sintered between 1300 and 1700 ºC. This decrease in hardness may be due to grain growth in the tungsten phase or structural flaws in the samples. Fractures and pores in the ceria phase were observed in the W-10CeO_2 and W-20CeO_2 samples (Figure 4.33). These fractures may be due to stresses between the tungsten and ceria interfaces caused by the mismatch in the coefficients of thermal expansion, or due to thermal shock in the ceria phase.

To determine the cause of the fractures in SPS W-10CeO_2 and W-20CeO_2, future experiments should focus on the effect of heating and cooling rates on the final microstructure of the compacts. The resulting compacts should be analyzed by doing both hardness testing and microscopy. It is possible that at slower heating and cooling

rates, the amount of fracturing in the ceria phase can be reduced, and the hardness of these parts will be increased.

5.6. Loss of Ceria During Spark Plasma Sintering

In this study, ceria loss was observed in the microstructures of W-10CeO_2, W-15CeO_2, and W-20CeO_2 in samples spark plasma sintered above 1600 ºC. In the W-15CeO_2 samples, Ce^{3+} and Ce^{4+} ions were present in the ceria phase, based on results using XPS. The presence of the Ce^{3+} ion indicates that the ceria phase is likely reduced from CeO_2 to Ce_2O_3, which releases oxygen gas. The formation of oxygen gas may lead to the formation of pores in the microstructure and the loss of ceria in tungsten-ceria compacts.

In future spark plasma sintering studies of tungsten-ceria, methods should be made to minimize and better understand the loss of ceria. To minimize the loss of ceria during spark plasma sintering, the initial particle size of the ceria should be increased from nanometer-sized powders to micron-sized powders. This suggestion is based on the ceria sintering results by Zhou.[133] To better understand the loss of ceria during spark plasma sintering, a residual gas analyzer should be coupled with the SPS vacuum system to measure the composition and concentration of gasses *in situ*.

5.7. Densification Kinetics of SPS Tungsten

The densification kinetics for SPS tungsten were analyzed using traditional hot pressing models for plastic flow, lattice diffusion, boundary diffusion, and power-law creep. Plastic flow is likely not the rate-limiting mechanism for densification in SPS

tungsten. This is because the effective stress between particles in the tungsten compact did not exceed the yield strength of the particles.

Hot press models for lattice diffusion, boundary diffusion, and power-law creep were solved for the diffusion coefficients. The diffusion coefficients were solved for SPS tungsten samples produced between 1000 and 1800 ºC.

The diffusion coefficients for lattice diffusion were plotted logarithmically as functions of reciprocal sintering temperature. The diffusivities that produced a near-linear fit were between 1100 and 1500 ºC. The Arrhenius equation for lattice diffusion, assuming that it is the rate-limiting mechanism of densification is SPS tungsten, is:

$$D_v = (1.4 \pm 0.3)\exp\left(\frac{-160 \pm 20}{RT}\right) \times 10^{-10} \text{ (m}^2\text{/s)} \qquad 5.1$$

where the activation energy, 160±20, is in units of kJ/mol. This activation energy is low when compared with the measured activation energy of lattice diffusion in tungsten, and the diffusion constant is orders of magnitude smaller than what is published in the open literature. Because these kinetics constants do not appear to fit with any of the open literature, it is unlikely that lattice diffusion is the rate-limiting mechanism of densification in SPS tungsten.

The diffusion coefficients for boundary diffusion were plotted logarithmically as functions of reciprocal sintering temperature. The diffusivities that produced a near-linear fit were between 1100 and 1500 ºC. The Arrhenius equation for boundary diffusion, assuming that it is the rate-limiting mechanism of densification is SPS tungsten, is:

$$D_b = (4.3 \pm 0.1)\exp\left(\frac{-360 \pm 20}{RT}\right) \text{ (m}^2\text{/s)} \qquad 5.2$$

where the activation energy, 360±20, is in units of kJ/mol. The activation energy and diffusion constant are similar to the activation energies and diffusion constants for boundary diffusion published in the literature. Based on these comparisons, it is likely that boundary diffusion is the rate-limiting mechanism of densification in SPS tungsten.

The diffusion coefficients for power-law creep were plotted logarithmically as functions of reciprocal sintering temperature. The diffusivities that produced a near-linear fit were between 800 and 1200 ºC. The Arrhenius equation for power-law creep, assuming that it is the rate-limiting mechanism of densification is SPS tungsten, is:

$$D_v = (8.4 \pm 6.4)\exp\left(\frac{-86 \pm 10}{RT}\right) \times 10^{-13} \text{ (m}^2\text{/s)} \qquad 5.3$$

where the activation energy, 86±10, is in units of kJ/mol. This activation energy is low when compared with the measured activation energy for power-law creep in tungsten, and the diffusion constant is orders of magnitude smaller than what is published in the open literature. Because these kinetics constants do not appear to fit with any of the open literature, it is unlikely that power-law creep is the rate-limiting mechanism of densification in SPS tungsten.

The hot press models were not effective in describing the kinetics of densification at higher temperatures. This may be due to an error in calculating the densification rate of SPS tungsten; or, a mechanism other than lattice diffusion, boundary diffusion, or power-law creep is responsible for densification at higher temperatures. Future work should include sintering more samples at each temperature and at smaller temperature intervals to establish a more accurate densification rate and to refine the temperature range for which the hot press model is valid. Future work should also incorporate

potential mechanisms of SPS into the hot press models to more accurately understand the sintering kinetics.

Traditional pressure sintering diagrams may not be effective in predicting the rate-limiting mechanism of densification in SPS tungsten. The maps do show that if the diffusion constants and activation energies are the same in SPS tungsten as they are in the absence of current, then the rate-limiting mechanism of densification is boundary diffusion for samples sintered below 1300 ºC and power-law creep for samples sintered above 1400 ºC. Future work is needed to measure the diffusion constants and activation energies for densifying mechanisms in SPS tungsten in order for accurate pressure sintering diagrams to be constructed.

5.8. Grain Growth Kinetics of SPS Tungsten

The mechanism of grain growth in SPS tungsten could not be determined in this study. Meaningful grain growth exponents could not be determined for the SPS tungsten samples isothermally sintered at 1200, 1500, and 1800 ºC. Assuming the grain growth exponent is 2, the activation energy for grain growth is 289±10 kJ/mol. Assuming the grain growth exponent is 3, the activation energy for grain growth is 411±12 kJ/mol. The large difference in these activation energies makes it difficult to determine the rate-limiting mechanism for grain growth in SPS tungsten.

To better understand the grain growth kinetics in SPS tungsten, future experiments should include isothermal sintering experiments in 50 ºC increments, rather than the 300 ºC increments used in this thesis. In addition, the time intervals between isothermally sintered samples should be reduced to determine a more accurate grain growth rate at each temperature.

WORKS CITED

[1]E. A. Olevsky and L. Froyen, "Impact of Thermal Diffusion on Densification During SPS," *Journal of the American Ceramic Society,* **92** [1] 122-32 (2009).

[2]D. W. Brite and K. R. Sump, "Cermet Materials and Process of Making," Patent No. 3,276,867 United States (1966).

[3]R. T. Carpenter, "Space Nuclear Power Systems," pp. 13-25 in National Symposium on Natural and Manmade Radiation in Space. Edited by E. A. Warman. (1971).

[4]R. A. Neff, M. E. Anderson, A. R. Campbell, and F. X. Haas, "Some Neutron and Gamma Radiation Characteristics of Plutonium Cermet Fuel for Isotopic Power Sources," pp. 853-58 in National Symposium on Natural and Manmade Radiation in Space. Edited by E. A. Warman. (1971).

[5]T. K. Keenan, R. E. Vallee, and J. A. Powers, "Radiation from Plutonium-238 Used in Space Applications," pp. 859-61 in National Symposium on Natural and Manmade Radiation in Space. Edited by E. A. Warman. (1971).

[6]H. S. Davis and E. F. Koprowski, "Nuclear Radiation Environment Analysis for Thermoelectric Outer Planet Spacecraft," pp. 862-65 in National Symposium on Natural and Manmade Radiation in Space. Edited by E. A. Warman. (1971).

[7]D. E. Burkes, D. M. Wachs, J. E. Werner, and S. D. Howe, "An Overview of Current and Past W-UO_2 Cermet Fuel Fabrication Technology," pp. 207-16 in Proceedings of Space Nuclear Conference 2007. (2007).

[8]Argonne National Laboratory, "Nuclear Rocket Program Terminal Report," AEC Research and Development report ANL-7236 (1966).

[9]C. Haertling and R. J. Hanrahan Jr, "Literature Review of Thermal and Radiation Performance Parameters for High-Temperature, Uranium Dioxide Fueled Cermet Materials," *Journal of Nuclear Materials,* **366** [3] 317-35 (2007).

[10]Nuclear Technology Department, "710 High-Temperature Gas Reactor Program Summary Report, Volume III, Fuel Element Development," General Electric report GEMP-600-V3 (1967).

[11]Jet Propulsion Laboratory, "Cassini Program Environmental Impact Statement Supporting Study," Cassini Document report 699-070-2 (1994).

[12]G. L. Bennett, "Mission Interplanetary: Using Radioisotope Power to Explore the Solar System," *Energy Conversion and Management,* **49** [3] 382-92 (2008).

[13]Energy Systems Division, "SNAP 19 Pioneer F & G Final Report," Teledyne Isotopes report IESD-2873-172 (1973).

[14]Z. Munir, U. Anselmi-Tamburini, and M. Ohyanagi, "The Effect of Electric Field and Pressure on the Synthesis and Consolidation of Materials: A Review of the Spark Plasma Sintering Method," *Journal of Materials Science,* **41** [3] 763-77 (2006).

[15]E. A. Olevsky, S. Kandukuri, and L. Froyen, "Consolidation Enhancement in Spark-Plasma Sintering: Impact of High Heating Rates," *Journal of Applied Physics,* **102** [11] 114913:1-12 (2007).

[16]M. Omori, "Sintering, Consolidation, Reaction and Crystal Growth by the Spark Plasma System (SPS)," *Materials Science and Engineering A,* **287** [2] 183-88 (2000).

[17]D. R. Koenig, "Experience Gained from the Space Nuclear Rocket Program (Rover)," Los Alamos National Laboratory report LA-10062-H (1986).

[18]E. Lassner and W. D. Schubert, "Tungsten: Properties, Chemistry, Technology of the Element, Alloys and Chemical Compounds." Kluwer Academic/Plenum Publishers: New York, 1999.

[19]D. G. Kolman, Y. Park, M. Stan, R. J. Hanrahan Jr., and D. P. Butt, "An Assessment of the Validity of Cerium Oxide as a Surrogate for Plutonium Oxide Gallium Removal Studies," Los Alamos National Laboratory report LA-UR-99-491 (1999).

[20]Y. S. Park, D. G. Kolman, H. Ziraffe, C. Haertling, and D. P. Butt, "Gallium Removal from Weapons-Grade Plutonium and Cerium Oxide Surrogate by a Thermal Technique," pp. 129-33 in Scientific Basis for Nuclear Waste Management XXII. **Vol. 556**, *Materials Research Society Symposium Proceedings* Edited by D. J. Wronkiewicz and J. H. Lee. Warrendale, PA, (1998).

[21]Y. S. Park, H. Y. Sohn, and D. P. Butt, "Thermal Removal of Gallium from Gallia-Doped Ceria," *Journal of Nuclear Materials,* **280** [3] 285-94 (2000).

[22]A. Nakamura, "A Defect-Thermodynamic Approach to PuO_{2-x} and CeO_{2-x}," *Journal of Nuclear Materials,* **201** 17-26 (1993).

[23]M. Zinkevich, D. Djurovic, and F. Aldinger, "Thermodynamic Modelling of the Cerium-Oxygen System," *Solid State Ionics,* **177** [11-12] 989-1001 (2006).

[24]C. Guéneau, C. Chatillon, and B. Sundman, "Thermodynamic Modelling of the Plutonium-Oxygen System," *Journal of Nuclear Materials,* **378** [3] 257-72 (2008).

[25]R. M. German, "Sintering Theory and Practice." John Wiley & Sons, Inc.: New York, 1996.

[26]R. Raj, "Analysis of the Sintering Pressure," *Journal of the American Ceramic Society,* **70** [9] C-210-11 (1987).

[27]M. N. Rahaman, "Sintering of Ceramics." CRC Press/Taylor & Francis Group: New York, 2008.

[28]R. Chaim, "Densification Mechanisms in Spark Plasma Sintering of Nanocrystalline Ceramics," *Materials Science and Engineering A,* **443** [1-2] 25-32 (2007).

[29]R. Chaim and M. Margulis, "Densification Maps for Spark Plasma Sintering of Nanocrystalline MgO Ceramics," *Materials Science and Engineering A,* **407** [1-2] 180-87 (2005).

[30]M. J. Readey and D. W. Readey, "Sintering of ZrO_2 in HCl Atmospheres," *Journal of the American Ceramic Society,* **69** [7] 580-82 (1986).

[31]G. C. Kuczynski, "Self-Diffusion in Sintering of Metallic Particles," *Transactions of the American Institute of Mining and Metallurgical Engineers,* **185** [2] 169-78 (1949).

[32]R. L. Coble and J. S. Ellis, "Hot-Pressing Alumina - Mechanisms of Material Transport," *Journal of the American Ceramic Society,* **46** [9] 438-41 (1963).

[33]E. J. Felten, "Hot-Pressing of Alumina Powders at Low Temperatures," *Journal of the American Ceramic Society,* **44** [8] 381-85 (1961).

[34]J. D. Mcclelland, "A Plastic Flow Model of Hot Pressing," *Journal of the American Ceramic Society,* **44** [10] 526-26 (1961).

[35]R. E. Mistler and R. L. Coble, "Grain-Boundary Diffusion and Boundary Widths in Metals and Ceramics," *Journal of Applied Physics,* **45** [4] 1507-09 (1974).

[36]K. R. Venkatachari and R. Raj, "Shear Deformation and Densification of Powder Compacts," *Journal of the American Ceramic Society,* **69** [6] 499-506 (1986).

[37]R. M. German, "Powder Metallurgy and Particulate Materials Processing." Metal Powder Industries Federation: Princeton, 2005.

[38]E. A. Olevsky, "Theory of Sintering: From Discrete to Continuum," *Materials Science and Engineering R,* **23** [2] 41-100 (1998).

[39]R. L. Coble, "Sintering Crystalline Solids. I. Intermediate and Final State Diffusion Models," *Journal of Applied Physics,* **32** [5] 787-92 (1961).

[40]R. L. Coble, "Diffusion Models for Hot Pressing with Surface Energy and Pressure Effects as Driving Forces," *Journal of Applied Physics,* **41** [12] 4798-807 (1970).

[41]D. S. Wilkinson and M. F. Ashby, "Pressure Sintering by Power Law Creep," *Acta Metallurgica,* **23** [11] 1277-85 (1975).

[42]R. C. Gifkins, "Diffusional Creep Mechanisms," *Journal of the American Ceramic Society,* **51** [2] 69-72 (1968).

[43]M. R. Notis, R. H. Smoak, and V. Krishnamachari, "Interpretation of Hot Pressing Kinetics by Densification Mapping Techniques," pp. 493-507 in Sintering and Catalysis**.** Edited by G. C. Kuczynski. Plenum Press, New York, 1975.

[44]H. J. Frost and M. F. Ashby, "Deformation-Mechanism Maps, the Plasticity and Creep of Metals and Ceramics," http://engineering.dartmouth.edu/defmech/. (Accessed: 5 Nov 2009)

[45]M. F. Ashby, "A First Report on Sintering Diagrams," *Acta Metallurgica,* **22** [3] 275-89 (1974).

[46]F. B. Swinkels and M. F. Ashby, "A Second Report on Sintering Diagrams," *Acta Metallurgica,* **29** [2] 259-81 (1981).

[47]D. S. Wilkinson and M. F. Ashby, "The Development of Pressure Sintering Maps," pp. 473-92 in 4th International Conference on Sintering and Related Phenomena. Edited by G. C. Kuczynski. New York, (1975).

[48]F. Sauerwald, "Über Einen Apparat Zur Direkten Widerstanderhitzung Auf Sehr Hohe Temperaturen Mit Vorrichtung Zur Gleichzeitigen Ausübung Eines Mechanischen," *Zeitschrift für Electrochemie Und angewandte Physikalische chemie,* **28** 181-83 (1922).

[49]G. F. Taylor, "Apparatus for Making Hard Metal Compositions," Patent No. 1,896,854 United States (1933).

[50]G. D. Cremer, "Powder Metallurgy," Patent No. 2,355,954 United States (1944).

[51]W. F. Ross, "Method and Apparatus for Making Solid Objects from Metal Powders," Patent No. 2,372,605 United States (1945).

[52]F. V. Lenel, "Resistance Sintering under Pressure," *Transactions of the American Institute of Mining and Metallurgical Engineers,* **203** [1] 158-67 (1955).

[53]K. Inoue, "Apparatus for Electrically Sintering Discrete Bodies," Patent No. 3,250,892 United States (1966).

[54]K. Inoue, "Electric-Discharge Sintering," Patent No. 3,241,956 United States (1966).

[55]K. R. Anderson, J. R. Groza, M. Fendorf, and C. J. Echer, "Surface Oxide Debonding in Field Assisted Powder Sintering," *Materials Science and Engineering A,* **270** [2] 278-82 (1999).

[56]J. R. Groza, "Field Activation Provides Improved Sintering," *Metal Powder Report,* **55** 16-18 (2000).

[57]J. R. Groza and A. Zavaliangos, "Sintering Activation by External Electrical Field," *Materials Science and Engineering: A,* **287** [2] 171-77 (2000).

[58]J. R. Groza, M. Garcia, and J. A. Schneider, "Surface Effects in Field-Assisted Sintering," *Journal of Materials Research,* **16** [1] 286-92 (2001).

[59]V. Y. Kodash, J. R. Groza, K. C. Cho, B. R. Klotz, and R. J. Dowding, "Field-Assisted Sintering of Ni Nanopowders," *Materials Science and Engineering A,* **385** [1-2] 367-71 (2004).

[60]D. M. Hulbert, A. Anders, J. Andersson, E. J. Lavernia, and A. K. Mukherjee, "A Discussion on the Absence of Plasma in Spark Plasma Sintering," *Scripta Materialia,* **60** [10] 835-38 (2009).

[61]K. C. Cho, R. H. Woodman, B. R. Klotz, and R. J. Dowding, "Plasma Pressure Compaction of Tungsten Powders," *Materials and Manufacturing Processes,* **19** [4] 619-30 (2004).

[62]G. Jones, J. R. Groza, K. Yamazaki, and K. Shoda, "Plasma Activated Sintering (PAS) of Tungsten Powders," *Materials and Manufacturing Processes,* **9** [6] 1105-14 (1994).

[63]D. Zhang, L. Zhang, J. Guo, and W. H. Tuan, "Direct Evidence of Temperature Variation within Ceramic Powder Compact During Pulse Electric Current Sintering," *Journal of the American Ceramic Society,* **89** [2] 680-83 (2006).

[64]K. Vanmeensel, A. Laptev, O. Van Der Biest, and J. Vleugels, "The Influence of Percolation During Pulsed Electric Current Sintering of ZrO_2-Tin Powder Compacts with Varying Tin Content," *Acta Materialia,* **55** [5] 1801-11 (2007).

[65]K. Vanmeensel, A. Laptev, O. Van Der Biest, and J. Vleugels, "Field Assisted Sintering of Electro-Conductive ZrO_2-Based Composites," *Journal of the European Ceramic Society,* **27** [2-3] 979-85 (2007).

[66]W. Chen, U. Anselmi-Tamburini, J. E. Garay, J. R. Groza, and Z. A. Munir, "Fundamental Investigations on the Spark Plasma Sintering/Synthesis Process: I. Effect of DC Pulsing on Reactivity," *Materials Science and Engineering A,* **394** [1-2] 132-38 (2005).

[67]U. Anselmi-Tamburini, J. E. Garay, and Z. A. Munir, "Fundamental Investigations on the Spark Plasma Sintering/Synthesis Process: III. Current Effect on Reactivity," *Materials Science and Engineering A,* **407** [1-2] 24-30 (2005).

[68]E. Olevsky and L. Froyen, "Constitutive Modeling of Spark-Plasma Sintering of Conductive Materials," *Scripta Materialia,* **55** [12] 1175-78 (2006).

[69]H. Muta, K. Kurosaki, M. Uno, and S. Yamanaka, "Thermal and Mechanical Properties of Uranium Nitride Prepared by SPS Technique," *Journal of Materials Science,* **43** [19] 6429-34 (2008).

[70]J. N. Dusza, G. Blugan, J. Morgiel, J. Kuebler, F. Inam, T. Peijs, M. J. Reece, and V. Puchy, "Hot Pressed and Spark Plasma Sintered Zirconia/Carbon Nanofiber Composites," *Journal of the European Ceramic Society,* **29** [15] 3177-84 (2009).

[71]R. Chaim, "Superfast Densification of Nanocrystalline Oxide Powders by Spark Plasma Sintering," *Journal of Materials Science,* **41** [23] 7862-71 (2006).

[72]Z. Guo, G. Blugan, R. Kirchner, M. Reece, T. Graule, and J. Kuebler, "Microstructure and Electrical Properties of Si_3N_4-Tin Composites Sintered by Hot Pressing and Spark Plasma Sintering," *Ceramics International,* **33** [7] 1223-29 (2007).

[73]U. Anselmi-Tamburini, S. Gennari, J. E. Garay, and Z. A. Munir, "Fundamental Investigations on the Spark Plasma Sintering/Synthesis Process: II. Modeling of

Current and Temperature Distributions," *Materials Science and Engineering A,* **394** [1-2] 139-48 (2005).

[74]U. Anselmi-Tamburini, J. E. Garay, and Z. A. Munir, "Fast Low-Temperature Consolidation of Bulk Nanometric Ceramic Materials," *Scripta Materialia,* **54** [5] 823-28 (2006).

[75]F. Inam, H. Yan, D. D. Jayaseelan, T. Peijs, and M. J. Reece, "Electrically Conductive Alumina-Carbon Nanocomposites Prepared by Spark Plasma Sintering," *Journal of the European Ceramic Society,* **In Press, Corrected Proof**.

[76]R. Orrù, R. Licheri, A. M. Locci, A. Cincotti, and G. Cao, "Consolidation/Synthesis of Materials by Electric Current Activated/Assisted Sintering," *Materials Science and Engineering R,* **63** [4-6] 127-287 (2009).

[77]Y. Kim, K. H. Lee, E. P. Kim, D. I. Cheong, and S. H. Hong, "Fabrication of High Temperature Oxides Dispersion Strengthened Tungsten Composites by Spark Plasma Sintering Process," *International Journal of Refractory Metals and Hard Materials,* **27** [5] 842-46 (2009).

[78]B. Chapman, "Glow Discharge Processes: Sputtering and Plasma Etching." John Wiley & Sons: New York, 1980.

[79]T. Kondo, M. Yasuhara, T. Kuramoto, Y. Kodera, M. Ohyanagi, and Z. Munir, "Effect of Pulsed DC Current on Atomic Diffusion of Nb-C Diffusion Couple," *Journal of Materials Science,* **43** [19] 6400-5 (2008).

[80]Y. Kornyushin, "Influence of External Fields on Sintering," pp. 3-17 in Advanced Science and Technology of Sintering**.** Edited by B. D. Stojanović, V. V. Skorokhod, and M. V. Nikolić. Kluwer Academic/Plenum Publishers, New York, 1999.

[81]W. A. Johnson, "Tungsten," pp. 577-81 in ASM Handbook*,* **Vol. 2.** Edited by J. R. Davis. ASM International, Materials Park, OH, 1994.

[82]D. M. Karpinos, A. A. Kravchenko, Y. L. Pilipovskii, V. G. Tkachenko, and Y. M. Shamatov, "Hot Pressing of Tungsten and Its Pseudoalloys. Part I," *Powder Metallurgy and Metal Ceramics,* **9** [4] 287-91 (1970).

[83]D. M. Karpinos, A. A. Kravchenko, Y. L. Pilipovskii, V. G. Tkachenko, and Y. M. Shamatov, "Hot Pressing of Tungsten and Its Pseudoalloys. Part II," *Powder Metallurgy and Metal Ceramics,* **10** [5] 367-72 (1971).

[84]R. M. German and Z. A. Munir, "Enhanced Low-Temperature Sintering of Tungsten," *Metallurgical Transactions A,* **7** [12] 1873-77 (1976).

[85]P. C. Bettler and F. M. Charbonnier, "Activation Energy for the Surface Migration of Tungsten in the Presence of a High-Electric Field," *Physical Review,* **119** [1] 85-93 (1960).

[86]J. P. Barbour, F. M. Charbonnier, W. W. Dolan, W. P. Dyke, E. E. Martin, and J. K. Trolan, "Determination of the Surface Tension and Surface Migration Constants for Tungsten," *Physical Review,* **117** [6] 1452-59 (1960).

[87]J. C. Peacock and A. D. Wilson, "Electrotransport of Tungsten and Life of a Filament," *Journal of Applied Physics,* **39** [13] 6037-41 (1968).

[88]K. G. Kreider and G. Bruggeman, "Grain Boundary Diffusion in Tungsten," *Transactions of the Metallurgical Society of AIME,* **239** [8] 1222-26 (1967).

[89]R. L. Andelin, J. D. Knight, and D. Kahn, "Diffusion of Tungsten and Rhenium Tracers in Tungsten," *Transactions of the Metallurgical Society of AIME,* **233** 19-24 (1965).

[90]R. E. Pawel and T. S. Lundy, "Tracer Diffusion in Tungsten," *Acta Metallurgica,* **17** [8] 979-88 (1969).

[91]W. V. Green, "Short-Time Creep-Rupture Behavior of Tungsten at 2250º to 2800º C," *Transactions of the American Institute of Mining and Metallurgical Engineers,* **215** [6] 1057-60 (1959).

[92]G. W. King and H. G. Sell, "Effect of Thoria on Elevated-Temperature Tensile Properties of Recrystallized High-Purity Tungsten," *Transactions of the Metallurgical Society of AIME,* **233** [6] 1104-13 (1965).

[93]S. L. Robinson and O. D. Sherby, "Mechanical Behavior of Polycrystalline Tungsten at Elevated Temperature," *Acta Metallurgica,* **17** [2] 109-25 (1969).

[94]W. D. Schubert, "Kinetics of the Hydrogen Reduction of Tungsten Oxides," *International Journal of Refractory Metals and Hard Materials,* **9** [4] 178-91 (1990).

[95]N. C. Kothari, "Sintering Kinetics in Tungsten Powder," *Journal of the Less Common Metals,* **5** [2] 140-50 (1963).

[96]G. Ehrlich and F. G. Hudda, "Atomic View of Surface Self-Diffusion: Tungsten on Tungsten," *The Journal of Chemical Physics,* **44** [3] 1039-49 (1966).

[97]F. P. Bowden and K. E. Singer, "Surface Self-Diffusion of Tungsten," *Nature,* **222** [5197] 977-79 (1969).

[98]G. King, "The Stress-Dependence of High Temperature Creep of Tungsten and a Tungsten-2 Wt Pct ThO_2 Alloy," *Metallurgical and Materials Transactions B,* **3** [4] 941-45 (1972).

[99]T. Vasilos and J. T. Smith, "Diffusion Mechanism for Tungsten Sintering Kinetics," *Journal of Applied Physics,* **35** [1] 215-17 (1964).

[100]V. I. Konstantinov, "The High-Temperature Sintering of Tungsten," *Powder Metallurgy and Metal Ceramics,* **4** [10] 805-12 (1965).

[101]N. C. Kothari, "Grain Growth During Sintering of Tungsten," *Journal of Applied Physics,* **38** [5] 2395-96 (1967).

[102]L. C. Chen, "Dilatometric Analysis of Sintering of Tungsten and Tungsten with Ceria and Hafnia Dispersions," *International Journal of Refractory Metals and Hard Materials,* **12** [1] 41-51 (1994).

[103]R. M. German and E. Olevsky, "Mapping the Compaction and Sintering Response of Tungsten-Based Materials into the Nanoscale Size Range," *International Journal of Refractory Metals and Hard Materials,* **23** [4-6] 294-300 (2005).

[104]V. D. Barth and H. O. McIntire, "Tungsten Powder Metallurgy," National Aeronautics and Space Administration report NASA SP-5035 (1965).

[105]J. W. Pugh and L. H. Amra, "On the Vacuum Sintering of Tungsten Ingots," *Journal of The Electrochemical Society,* **107** [12] 990-93 (1960).

[106]H. W. Hayden and J. H. Brophy, "Low-Temperature Sintering of Pure Tungsten and Tungsten-Iridium," *Journal of the Less Common Metals,* **6** [3] 214-18 (1964).

[107]D. M. Karpinos, A. A. Kravchenko, Y. L. Pilipovskii, V. G. Tkachenko, and Y. M. Shamatov, "Reaction of Tungsten with Die Material in Hot Pressing," *Powder Metallurgy and Metal Ceramics,* **9** [10] 831-34 (1970).

[108]D. J. Jones, "Practical Aspects of Sintering Tungsten and Molybdenum," *Journal of the Less Common Metals,* **2** [2-4] 76-85 (1960).

[109]R. M. German, J. Ma, X. Wang, and E. Olevsky, "Processing Model for Tungsten Powders and Extension to Nanoscale Size Range," *Powder Metallurgy,* **49** [1] 19-27 (2006).

[110]B. McWilliams, A. Zavaliangos, K. C. Cho, and R. J. Dowding, "The Modeling of Electric-Current-Assisted Sintering to Produce Bulk Nanocrystalline Tungsten," *Journal of the Minerals, Metals and Materials Society,* **58** [4] 67-71 (2006).

[111]Z. J. Zhou, Y. Ma, J. Du, and J. Linke, "Fabrication and Characterization of Ultra-Fine Grained Tungsten by Resistance Sintering Under Ultra-High Pressure," *Materials Science and Engineering A,* **505** [1-2] 131-35 (2009).

[112]Chino Corporation, "IR-AH Series Hand-Held Type Digital Radiation Thermometer," Tokyo (2003).

[113]ASTM Standard B311, 1993 (2002), "Test Method for Density Determination for Powder Metallurgy (P/M) Materials Containing Less Than Two Percent Porosity," ASTM International, West Conshohocken, PA (2002).

[114]ASTM Standard B962, 2008, "Standard Test Methods for Density of Compacted or Sintered Powder Metallurgy (PM) Products Using Archimedes' Principle," ASTM International, West Conshohocken, PA (2008).

[115]G. Van Der Voort, "Metallography: Principles and Practice." ASM International: Materials Park, OH, 1999.

[116]Wolfram Research, Inc., "Mathematica," Version 7.0, Champaign, IL (2008).

[117]ASTM Standard E384, 2009, "Standard Test Method for Microindentation Hardness of Materials," ASTM International, West Conshohocken, PA (2009).

[118]M. Fatima Vaz and M. A. Fortes, "Grain Size Distribution: The Lognormal and the Gamma Distribution Functions," *Scripta Metallurgica,* **22** [1] 35-40 (1988).

[119]X. H. Zhou and S. Gao, "Confidence Intervals for the Log-Normal Mean," *Statistics in Medicine,* **16** [7] 783-90 (1997).

[120]R. G. Sheppard, D. M. Mathes, and D. J. Bray, "Properties and Characteristics of Graphite: For Industrial Use," Poco Graphite, Inc., Decatur, TX (2001).

[121]G. W. Burns, M. G. Kaeser, G. F. Strouse, M. C. Croarkin, and W. F. Guthrie, "Temperature Electromotive Force Reference Functions and Tables for the Letter-Designated Thermocouple Types Based on the ITS-90." National Institute of Standards and Technology Monograph 175, 1993.

[122]W. Navidi, "Statistics for Engineers and Scientists," 3rd Edition. McGraw-Hill Science/Engineering/Math, 2003.

[123]P. Angerer, E. Neubauer, L. G. Yu, and K. A. Khor, "Texture and Structure Evolution of Tantalum Powder Samples During Spark-Plasma-Sintering (SPS) and Conventional Hot-Pressing," *International Journal of Refractory Metals and Hard Materials,* **25** [4] 280-85 (2007).

[124]R. E. Reed-Hill and R. Abbaschian, "Physical Metallurgy Principles," 3rd edition. PWS Publishing Company: Boston, 1994.

[125]B. B. Straumal, W. Gust, V. G. Sursaeva, V. N. Semenov, and L. S. Shvindlerman, "Normal and Abnormal Grain Growth in Tungsten Polycrystals," pp. 533-36. Edited by P. Lejcek and V. Paidar. (1999).

[126]T. K. Gupta, "Possible Correlation between Density and Grain Size During Sintering," *Journal of the American Ceramic Society,* **55** [5] 276-77 (1972).

[127]G. E. Dieter, "Mechanical Metallurgy." McGraw-Hill, Inc: Boston, 1986.

[128]W. D. Kingery, "Note on Thermal Expansion and Microstresses in Two-Phase Compositions," *Journal of the American Ceramic Society,* **40** [10] 351-52 (1957).

[129]Z. H. Jin and Y. W. Mai, "Effects of Damage on Thermal-Shock Strength Behavior of Ceramics," *Journal of the American Ceramic Society,* **78** [7] 1873-81 (1995).

[130]T. Sata and M. Yoshimura, "Some Material Properties of Cerium Sesquioxide," *Journal of the Ceramic Society of Japan,* **76** [872] 116-22 (1968).

[131]R. L. Coble and W. D. Kingery, "Effect of Porosity on Thermal Stress Fracture," *Journal of the American Ceramic Society,* **38** [1] 33-37 (1955).

[132]M. Yoshimura, "X-Ray Characterization and Thermal Properties of $3R_2O_3$:$2WO_3$ Compounds (R = La, Ce, Pr, and Nd)," *Journal of the American Ceramic Society,* **60** [1-2] 77-78 (1977).

[133]Y. Zhou, "The Influence of Redox Reaction of the Sintering of Cerium Oxide," *Journal of Materials Synthesis and Processing,* **6** [6] 411-14 (1998).

[134]M. W. Chase, C. A. Davies, J. R. Downey, D. J. Frurip, R. A. McDonald, and A. N. Syverud, "JANAF Thermochemical Tables, Third Edition," *Journal of Physical and Chemical Reference Data,* **14** [Supplement 1] (1985).

[135]H. Su and D. L. Johnson, "Master Sintering Curve: A Practical Approach to Sintering," *Journal of the American Ceramic Society,* **79** [12] 3211-17 (1996).

[136]K. An and D. L. Johnson, "The Pressure-Assisted Master Sintering Surface," *Journal of Materials Science,* **37** [21] 4555-59 (2002).

[137]K. Rozenburg, I. E. Reimanis, H. J. Kleebe, and R. L. Cook, "Sintering Kinetics of a $MgAl_2O_4$ Spinel Doped with LiF," *Journal of the American Ceramic Society,* **91** [2] 444-50 (2008).

[138]M. M. R. Boutz, A. J. A. Winnubst, and A. J. Burggraaf, "Yttria-Ceria Stabilized Tetragonal Zirconia Polycrystals: Sintering, Grain Growth and Grain Boundary Segregation," *Journal of the European Ceramic Society,* **13** [2] 89-102 (1994).

[139]R. E. Mistler, "Comments on the Paper 'Grain Growth During Sintering of Tungsten'," *Journal of Applied Physics,* **39** [10] 4875 (1968).

APPENDIX

Results For SPS and HP Tungsten and Tungsten-Ceria Samples

Table A.1. Fractional densities, grain sizes, and hardnesses of tungsten, W-1CeO_2, W-10CeO_2, and W-20CeO_2 spark plasma sintered with a 40 ºC/min heating rate and soaked at maximum temperature for 2 min.

Composition	Applied pressure (MPa)	Adjusted temperature (ºC)	Fractional density	95% C.I. for mean grain size (μm)	Hardness range (Hv)
Pure W	42	1313±8	0.801±0.011	2.04-2.14	228-288
		1413±8	0.817±0.008	3.24-3.44	206-294
		1513±16	0.850±0.013	3.96-4.27	247-306
		1713±18	0.894±0.015	5.62-6.17	260-316
	64	1314±8	0.835±0.009	2.51-2.64	-
		1414±8	0.868±0.011	4.06-4.28	222-261
		1513±16	0.884±0.014	4.51-4.78	233-264
		1613±17	0.892±0.012	5.41-5.88	261-306
		1710±18	0.906±0.012	5.34-5.91	284-299
W-1CeO_2	42	1313±8	0.867±0.010	1.96-2.04	214-230
		1412±8	0.863±0.012	2.18-2.28	220-246
		1513±16	0.876±0.012	2.61-2.72	216-237
		1612±17	0.889±0.011	3.48-3.70	237-281
		1713±18	0.897±0.020	4.19-4.51	248-274
	64	1313±8	0.865±0.009	1.32-1.37	249-285
		1413±8	0.890±0.009	2.55-2.70	257-292
		1509±16	0.890±0.010	2.80-2.98	304-338
		1612±17	0.891±0.010	3.56-3.85	294-346
		1710±18	0.901±0.012	4.01-4.37	302-332
W-10CeO_2	42	1315±8	0.915±0.017	0.40-0.42	471-516
		1412±8	0.932±0.015	1.75-1.83	465-486
		1512±16	0.937±0.018	2.82-2.99	426-460
		1609±17	0.938±0.021	5.43-5.93	341-388
		1712±18	0.946±0.014	5.99-6.48	355-389
	64	1314±8	0.931±0.016	0.41-0.44	456-566
		1411±8	0.938±0.018	3.33-3.55	394-432
		1512±16	0.942±0.015	3.45-3.74	385-429
		1608±17	0.947±0.015	5.15-5.55	356-389
		1712±18	0.985±0.200	6.75-7.36	231-315
W-20CeO_2	42	1310±8	0.927±0.015	-	699-765
		1412±8	0.928±0.015	1.78-1.87	436-475
		1511±16	0.931±0.018	2.56-2.72	453-486
		1610±17	0.945±0.020	3.76-4.12	460-542
		1710±18	0.982±0.035	6.37-6.94	378-419
	64	1310±8	0.927±0.010	-	696-761
		1410±8	0.931±0.012	2.78-2.94	359-437
		1512±16	0.942±0.025	3.46-3.67	415-469
		1610±17	0.952±0.020	3.67-3.99	392-444
		1709±18	0.958±0.019	4.33-4.68	367-418

Table A.2. Fractional densities, average grain sizes, and hardnesses of pure tungsten spark plasma sintered with a 100 ºC/min heating rate and 64 MPa applied pressure.

Adjusted temperature (ºC)	Soak time (min)	Fractional density	95% C.I. for mean grain size (μm)	Hardness range (Hv)
825±5	2	0.477±0.003	-	-
919±6	2	0.519±0.002	-	-
923±6	5	0.549±0.002	-	-
911±6	8	0.566±0.002	-	44-46
909±6	14	0.572±0.002	-	50-57
908±6	20	0.585±0.002	-	75-87
907±6	26	0.598±0.002	-	52-69
1018±6	2	0.610±0.002	0.28-0.30	84-96
1119±7	2	0.703±0.003	0.31-0.31	147-191
1226±7	2	0.789±0.003	0.43-0.46	149-303
1214±7	5	0.803±0.003	0.49-0.52	212-272
1211±7	8	0.817±0.003	0.58-0.61	231-312
1209±7	14	0.826±0.003	0.60-0.64	213-320
1209±7	20	0.834±0.003	0.62-0.65	228-301
1209±7	26	0.853±0.003	0.66-0.70	288-363
1330±8	2	0.839±0.003	0.85-0.87	233-334
1423±8	2	0.843±0.003	1.41-1.45	200-239
1518±16	2	0.892±0.004	2.44-2.55	254-281
1515±16	5	0.894±0.003	3.20-3.40	228-338
1513±16	8	0.897±0.003	3.62-3.89	267-297
1511±16	14	0.899±0.004	3.73-4.02	264-322
1510±16	20	0.901±0.003	4.14-4.50	307-325
1510±16	26	0.902±0.004	4.43-4.82	297-326
1617±17	2	0.932±0.004	2.88-3.25	272-301
1723±18	2	0.939±0.003	3.19-3.38	278-329
1822±19	2	0.957±0.004	3.67-3.99	327-377
1813±19	5	0.966±0.004	5.83-6.46	335-359
1813±19	8	0.968±0.004	5.87-6.51	350-376
1812±19	14	0.973±0.004	7.71-8.82	316-349
1812±19	20	0.975±0.004	9.89-11.65	299-352
1811±19	26	0.977±0.004	12.94-15.79	332-374

Table A.3. Fractional densities and hardnesses of W-10CeO_2 spark plasma sintered with a 100 ºC/min heating rate and 64 MPa applied pressure.

Adjusted temperature (ºC)	Soak time (min)	Fractional density	Hardness range (Hv)
825±5	2	0.505±0.002	-
824±5	2	0.505±0.002	-
919±6	2	0.529±0.002	37-47
919±6	2	0.530±0.002	39-50
911±6	5	0.531±0.002	44-54
909±6	8	0.536±0.002	47-60
907±6	14	0.541±0.002	43-53
907±6	20	0.559±0.002	54-67
1019±6	2	0.619±0.002	96-111
1123±7	2	0.717±0.002	347-480
1218±7	2	0.780±0.003	319-369
1218±7	2	0.743±0.003	239-297
1213±7	5	0.793±0.003	368-460
1211±7	8	0.818±0.003	418-482
1209±7	14	0.856±0.003	356-526
1209±7	14	0.844±0.003	381-496
1209±7	20	0.793±0.003	417-496
1322±8	2	0.904±0.003	416-566
1321±8	2	0.903±0.003	456-513
1417±8	2	0.908±0.003	335-492
1518±16	2	0.933±0.003	312-364
1515±16	5	0.916±0.003	381-426
1514±16	5	0.939±0.003	401-423
1512±16	8	0.920±0.003	400-431
1511±16	14	0.918±0.003	370-416
1510±16	20	0.965±0.004	311-408
1619±17	2	0.959±0.004	260-356
1619±17	2	0.950±0.004	291-289

Table A.4. Area fractions of tungsten and ceria in W-10CeO_2, W-15CeO_2, and W-20CeO_2 spark plasma sintered with 42 MPa applied pressure and soaked at maximum temperature for 2 min.

Composition	Adjusted Temperature (ºC)	Area Fraction Tungsten	Area Fraction Ceria	Area Fraction Error
W-10CeO_2	1315±8	0.771	0.224	0.01
	1412±8	0.789	0.209	0.01
	1512±16	0.784	0.207	0.01
	1609±17	0.781	0.219	0.02
	1712±18	0.819	0.175	0.02
W-15CeO_2	1313±8	0.725	0.271	0.02
	1414±8	0.720	0.278	0.01
	1514±16	0.697	0.301	0.02
	1610±17	0.723	0.267	0.01
	1713±18	0.752	0.236	0.01
W-20CeO_2	1412±8	0.530	0.468	0.01
	1511±16	0.548	0.450	0.01
	1610±17	0.580	0.417	0.01
	1710±18	0.694	0.302	0.02

Table A.5. Fractional densities and grain sizes for pure tungsten and W-4CeO_2 hot pressed for 30 min at maximum temperature.

Composition	Temperature (ºC)	Fractional Density	95% C.I. of mean grain size (μm)
Pure W	1300±20	-	2.92-3.14
	1400±20	0.776±0.020	3.88-4.23
	1500±20	0.832±0.010	5.03-5.58
	1600±20	0.852±0.011	6.96-8.05
W-4CeO_2	1300±20	0.848±0.004	3.88-4.29
	1400±20	0.850±0.004	5.57-6.39
	1500±20	0.853±0.003	5.83-6.64
	1600±20	0.855±0.006	12.50-17.36